นาโนคอมพอสิตของพอลิเมอร์และเบนโทไนต์และแอลดีเอชที่มีสมบัติแม่เหล็กสำหรับการขจัดสารหนู
จากสารละลายน้ำ

นายสุนทร สุวอเขียว

วิทยานิพนธ์นี้เป็นส่วนหนึ่งของการศึกษาตามหลักสูตรปริญญาวิทยาศาสตรดุษฎีบัณฑิต
สาขาวิชาเคมี ภาควิชาเคมี
คณะวิทยาศาสตร์ จุฬาลงกรณ์มหาวิทยาลัย
ปีการศึกษา 2558

POLYMER-BENTONITE NANOCOMPOSITES AND MAGNETIC LDH FOR REMOVAL OF ARSENIC FROM AQUEOUS SOLUTION

Mr. Soontorn Suvokhiaw

A Dissertation Submitted in Partial Fulfillment of the Requirements
for the Degree of Doctor of Philosophy Program in Chemistry
Department of Chemistry
Faculty of Science
Chulalongkorn University
Academic Year 2015

Thesis Title	POLYMER-BENTONITE NANOCOMPOSITES AND MAGNETIC LDH FOR REMOVAL OF ARSENIC FROM AQUEOUS SOLUTION
By	Mr. Soontorn Suvokhiaw
Field of Study	Chemistry
Thesis Advisor	Nipaka Sukpirom, Ph.D.

Accepted by the Faculty of Science, Chulalongkorn University in Partial Fulfillment of the Requirements for the Doctoral Degree

.....Dean of the Faculty of Science
(Associate Professor Polkit Sangvanich, Ph.D.)

THESIS COMMITTEE

.....Chairman
(Associate Professor Vudhichai Parasuk, Ph.D.)

.....Thesis Advisor
(Nipaka Sukpirom, Ph.D.)

.....Examiner
(Assistant Professor Apichat Imyim, Ph.D.)

.....Examiner
(Numpon Insin, Ph.D.)

.....External Examiner
(Assistant Professor Anawat Pinisakul, Ph.D.)

สุนทร สุวอเขียว : นาโนคอมพอสิตของพอลิเมอร์และเบนโทไนต์และแอลดีเอชที่มีสมบัติแม่เหล็กสำหรับการขจัดสารหนูจากสารละลายน้ำ (POLYMER-BENTONITE NANOCOMPOSITES AND MAGNETIC LDH FOR REMOVAL OF ARSENIC FROM AQUEOUS SOLUTION) อ.ที่ปรึกษาวิทยานิพนธ์หลัก: อ. ดร.นิปกา สุขภิรมย์, 148 หน้า.

งานวิจัยนี้มุ่งเน้นสังเคราะห์คอมพอสิตของเคลย์ทั้งสองชนิด (cationic และ anionic clays) โดยการเพิ่มหมู่ฟังก์ชันเพื่อให้เหมาะแก่การเป็นตัวดูดซับอาร์เซเนตที่ดี

งานวิจัยนี้ได้สังเคราะห์นาโนคอมพอสิตชนิด pAPTMA/bentonite และ pAETMA/bentonite ด้วยวิธี solution intercalation และ *in-situ* intercalative polymerization จากการพิสูจน์เอกลักษณ์ทำให้ทราบว่าเกิดการแทรกตัวของพอลิเมอร์เข้าไปอยู่ข้างในชั้นของเบนโทไนต์กลายเป็นนาโนคอมพอสิต นอกจากนี้ยังพบว่านาโนคอมพอสิตที่ได้จากวิธี solution intercalation มีค่าการดูดซับอาร์เซเนตที่สูงกว่า โดยค่าการดูดซับสูงสุดที่ได้คือ 47.7 mg/g polymer (pAPTMA/bentonite) และ 46.2 mg/g polymer (pAETMA/bentonite) การศึกษาจลนศาสตร์การดูดซับบ่งชี้ว่าการดูดซับเกิดจาก chemisorption และไอโซเทอมของการดูดซับของ pAPTMA/bentonite และ pAETMA/bentonite สอดคล้องกับแบบจำลองการดูดซับของฟรุนดลิช ซึ่งอธิบายพฤติกรรมการดูดซับอาร์เซเนตบนพื้นผิวแบบเฮเทอโรจีเนียสของนาโนคอมพอสิต

งานวิจัยนี้ยังได้สังเคราะห์คอมพอสิตของแม่เหล็กและเลเยอร์ดับเบิลไฮดรอกไซด์โดยการตกตะกอนเลเยอร์ดับเบิลไฮดรอกไซด์ (LDH) ในสารละลายที่มีอนุภาค Fe_3O_4 อยู่ จากการพิสูจน์เอกลักษณ์ พบว่าคอมพอสิตที่สังเคราะห์ได้ประกอบด้วยอนุภาค Fe_3O_4 ที่ถูกห่อหุ้มด้วย LDH และพบว่ามีค่าการดูดซับอาร์เซนิกเท่ากับ 188 mg/g ที่ pH 3 จากการศึกษาไอโซเทอมของการดูดซับและจลนศาสตร์การดูดซับ พบว่าการดูดซับเป็นแบบชั้นเดียวและมีกลไกการดูดซับสองขั้นตอนซึ่งเกี่ยวข้องกับการคืนสภาพของ LDH ตามด้วยการแลกเปลี่ยนแอนไอออน

ภาควิชา เคมี ลายมือชื่อนิสิต .....

สาขาวิชา เคมี ลายมือชื่อ อ.ที่ปรึกษาหลัก .....

ปีการศึกษา 2558

5472900423 : MAJOR CHEMISTRY
KEYWORDS: POLYMER/CLAY NANOCOMPOSITE / BENTONITE / LAYERED DOUBLE HYDROXIDE / MAGNETIC COMPOSITE / ARSENIC ADSORPTION

SOONTORN SUVOKHIAW: POLYMER-BENTONITE NANOCOMPOSITES AND MAGNETIC LDH FOR REMOVAL OF ARSENIC FROM AQUEOUS SOLUTION. ADVISOR: NIPAKA SUKPIROM, Ph.D., 148 pp.

This work aimed to incorporate the designed functional parts into both cationic and anionic clays so that they became efficient in arsenate adsorption.

Both pAPTMA/bentonite and pAETMA/bentonite nanocomposites were synthesized via solution intercalation and *in-situ* intercalative polymerization method. The characterization revealed that both polymers intercalated in between the interlayers of bentonite. Comparing between two methods, the composites prepared via solution intercalation method provided higher As(V) adsorption amount. The maximum As(V) adsorption amounts were 47.7 mg/g polymer (for pAPTMA/bentonite) and 46.2 mg/g polymer (pAETMA/bentonite). The adsorption kinetics indicated the chemisorption process. The adsorption isotherm is fitted to the Freundlich model for both pAPTMA/bentonite and pAETMA/bentonite nanocomposites describing the adsorption behavior of As(V) onto the heterogeneous surface of nanocomposites.

The magnetic layered double hydroxide composite was synthesized by coprecipitation of layered double hydroxide (LDH) precursors in the presence of Fe_3O_4 particles. The characterization revealed that the composite was comprised of Fe_3O_4 particles covered by a LDH. The As(V) adsorption capacity (188 mg/g) was achieved at pH 3. The kinetics studies and adsorption isotherms suggested a two-stepped adsorption mechanism of the monolayer adsorption inside the interlayers of LDH. The adsorption mechanism involved the reconstruction process of LDH phase and the ion-exchange between the interlayers of reconstructed LDH.

Department:	Chemistry	Student's Signature	.....
Field of Study:	Chemistry	Advisor's Signature	.....
Academic Year:	2015		

ACKNOWLEDGEMENTS

The author deeply appreciates his family for their love, support and encouragement during the period of his study.

The author wishes to express greatest gratitude to his advisor, Dr Nipaka Sukpirom, for her valuable advice, kind assistance, and encouragement throughout the course of this research. Gratefully thanks to Assistant Professor Dr. Apichat Imyim, for his good advice, kind assistance, the support on equipment. In addition, the author would like to thank to Associate Professor Dr. Vudhichai Parasuk, Assistant Professor Dr. Apichat Imyim, Assistant Professor Anawat Pinisakul, and Dr. Numpon Insin for serving as chairman and examiner of his thesis committee, respectively, for their valuable suggestions and comments.

The author would like to thank Physical Chemistry Laboratory Department of Chemistry, Faculty of Science, Chulalongkorn University for the support on the TGA equipment, Materials chemistry and Catalysis Research Unit (MATCAT), and Environmental Analysis Research Unit (EARU) for provision of experimental facilities. Appreciation is extended to Department of Chemistry, Faculty of Science, Chulalongkorn University. Acknowledgement is also extended to the 90th Anniversary of Chulalongkorn University Fund and the Ratchadapisek Sompoch Endowment Fund (2015), Chulalongkorn University (CU-58-014-FW) for granting financial support to fulfill this study as well as the Development and Promotion of Science and Technology (DPST).

This thesis cannot be completed without generous help of the staff members of Materials chemistry and Catalysis Research Unit (MATCAT) and Environmental Analysis Research Unit (EARU). Special thank is forwarded to his best friends for their love, assistance and encouragement. Without them the author would have been able to achieve this goal.

CONTENTS

Page

THAI ABSTRACT iv

ENGLISH ABSTRACT v

ACKNOWLEDGEMENTS vi

CONTENTS vii

LIST OF FIGURES xiv

LIST OF TABLES xxii

LIST OF ABBREVIATIONS xxiii

CHAPTER 1 INTRODUCTION 1

1.1 Fundamental of arsenic 1

1.2 Composite 2

1.3 Clay minerals 4

1.4 Polymer/clay nanocomposites 5

1.4.1 The advantage of polymey/clay nanocomposites over individual parts 6

1.4.2 Polymer/clay nanocomposites as adsorbent for contaminants removals 7

1.4.3 Polymer/clay nanocomposites with polycations 8

1.4.4 Cationic polymer for anion contaminants removal 9

1.4.4.1 Poly(3-acrylamidopropyl)trimethylammonium chloride (pAPTMA-Cl) 9

1.4.4.2 Poly[2-(acryloyloxy)ethyl]trimethylammonium chloride (pAETMA-Cl) 10

1.5 Magnetic layered double hydroxides composites 11

1.5.1 Layered double hydroxides 11

Page

1.5.2 Magnetite (Fe_3O_4) 11
1.5.3 Composite of magnetite and LDHs 12
1.6 The objectives of this study 13
CHAPTER 2 THEORY 14
2.1 Clay and clay minerals 14
2.1.1 Conventional phyllosilicates 15
2.1.1.1 The 1:1 phyllosilicates (T-O) 17
2.1.1.2 The 2:1 phyllosilicates (T-O-T) 17
2.1.1.2.1 The 2:1 phyllosilicates with no interlayer 17
2.1.1.2.2 The 2:1 phyllosilicates with cation interlayer 18
2.1.1.2.3 The 2:1 phyllosilicates with octahedral sheet interlayer 19
2.1.2 Anionic clay 20
2.1.2.1 Structure of LDHs 21
2.1.2.2 Natural occurrence LDHs 22
2.1.2.3 Synthetic LDHs 23
2.1.2.4 Synthesis method of LDHs [42, 43, 97] 23
2.1.2.4.1 Coprecipitation 23
2.1.2.4.2 The urea method 24
2.1.2.4.3 Ion exchange method 24
2.1.2.4.4 Reconstruction 25
2.2 Composites 25
2.3 Polymer/clay composites 26

Page

2.3.1 Conventional composite or microcomposite [27, 29, 101] 26
2.3.2 Intercalated nanocomposite [27, 29, 34, 38, 99-101] 26
2.3.3 Exfoliated nanocomposite [27, 29, 34, 38, 99-101] 27
2.4 Preparation of polymer/clay composites 27
2.4.1 In situ template polymerization [27, 29, 34] 27
2.4.2 Solution intercalation [27, 29, 34, 38] 28
2.4.3 In situ intercalative polymerization [27, 29, 34, 38] 28
2.4.4 Melt intercalation [27, 29, 34, 38] 29
2.5 X-Ray Diffraction (XRD) 29
Bragg's law 30
2.6 N_2 adsorption-desorption isotherm 31
BET surface area 33
2.7 Adsorption kinetics 34
2.7.1 Pseudo first-order model [110-112] 34
2.7.2 Pseudo second-order model [113] 34
2.8 Adsorption isotherm 35
2.8.1 Langmuir isotherm [114-117] 35
2.8.2 Frudlich isotherm [114-119] 37
CHAPTER 3 EXPERIMENTAL 38
3.1 Chemicals 38
3.2 Preparation of Na-bentonite 38
3.3 Synthesis of polymer/bentonite nanocomposites via solution intercalation method 39

Page

3.3.1 Preparation of preformed polymer solution 39
3.3.2 Preparation of polymer-bentonite nanocomposites 40
3.4 Synthesis of polymer/bentonite nanocomposites via *in situ* intercalative polymerization method 40
3.5 Synthesis of magnetic/LDH composite via coprecipitation method 41
3.5.1 Preparation of Fe_3O_4 41
3.5.2 Preparation of the LDH 41
3.5.3 Preparation of the Mg-Fe-Zr LDH/Fe_3O_4 composite (m-LDH) 42
3.6 Characterization 42
3.7 Arsenate adsorptions studies of polymer/bentonite nanocomposites 43
3.7.1 Effect of sorbent dosage 43
3.7.2 Effect of contact time 43
3.7.3 Effect of pH of solution on As(V) adsorption 44
3.7.4 Effect of initial As(V) concentration 44
3.7.5 Effect of interference anions 44
3.8 Arsenate adsorption studies of magnetic LDH composites 44
3.8.1 Effect of contact time 45
3.8.2 Effect of pH of solution on As(V) adsorption 45
3.8.3 Effect of initial As(V) concentration 45
CHAPTER 4 RESULTS AND DISCUSSION 46
4.1 Synthesis of polymer/bentonite nanocomposites via solution intercalation method 46
4.1.1 Poly(3-acrylamidopropyl)trimethylammonium chloride) 46
4.1.1.1 Effect of monomer concentration 46

Page

4.1.1.2 Effect of cross-linker concentration 54
4.1.1.3 Effect of Initiator concentration 56
4.1.1.4 Effect of Na-bentonite concentration 58
4.1.2 Poly([2-(acryloyloxy)ethyl]trimethylammonium chloride) 62
4.1.2.1 Effect of monomer concentration 62
4.1.2.2 Effect of cross-linker concentration 66
4.1.2.3 Effect of Initiator concentration 68
4.1.2.4 Effect of Na-bentonite concentration 70
4.2 Synthesis of polymer/bentonite nanocomposites via *in-situ* intercalative polymerization method 73
4.2.1 Poly(3-acrylamidopropyl)trimethylammonium chloride) 74
4.2.1.1 Effect of cross-linker concentration 74
4.2.1.2 Effect of Initiator concentration 79
4.2.1.3 Effect of Na-bentonite concentration 81
4.2.2 Poly([2-(acryloyloxy)ethyl]trimethylammonium chloride) 84
4.2.2.1 Effect of cross-linker concentration 84
4.2.2.2 Effect of Initiator concentration 88
4.2.2.3 Effect of Na-bentonite concentration 90
4.3 Comparison of the As(V) adsorption performance for the composite from different polymers and synthesis routes 92
4.4 Optimization of As(V) adsorption parameters of polymer/bentonite nanocomposites 94
4.4.1 Effect of an adsorbent dose 94
4.4.2 Effect of contact time 95

Page

4.4.3 Effect of initial pH of arsenate solution 100

4.4.4 Effect of initial concentration of arsenate 101

4.4.5 Effect of interference anions 105

4.6 Arsenic removals from real wastewater using polymer/bentonite nanocomposites 106

4.7 Synthesis and characterization of magnetic layered double hydroxide composite via coprecipitation method 107

4.7.1 Synthesis of Fe_3O_4 107

4.7.2 Synthesis of $[Mg_{0.66}Fe_{0.33-x}Zr_x(OH)_2](CO_3)\delta$ (x = 0 – 0.33) 108

4.7.3 Synthesis of Fe_3O_4/Mg-Fe-Zr LDH composite 111

4.8 Optimization of As(V) adsorption parameters of magnetic/LDH composite 116

4.8.1 Effect of initial pH of arsenate solution 118

4.8.2 Effect of contact time 120

4.8.3 Effect of Initial concentration of arsenate 123

4.9 As removals from real wastewater using magnetic/LDH composite 125

CHAPTER 5 CONCLUSION 126

5.1 Synthesis of polymer/bentonite nanocomposites via solution intercalation method 126

5.1.1 Poly(3-acrylamidopropyl)trimethylammonium chloride) 126

5.1.2 Poly([2-(acryloyloxy)ethyl]trimethylammonium chloride) 126

5.2 Synthesis of polymer/bentonite nanocomposites via *in-situ* intercalative polymerization method 127

5.2.1 Poly(3-acrylamidopropyl)trimethylammonium chloride) 127

5.2.2 Poly([2-(acryloyloxy)ethyl]trimethylammonium chloride) 128

Page

5.3 Comparison of the As(V) adsorption performance for the composite from different polymers and synthesis routes 128

5.4 Synthesis of magnetic layered double hydroxide composite 129

5.5 The As(V) adsorption of Fe_3O_4/Mg-Fe-Zr LDH composite 129

5.6 Suggestions 130

REFERENCES 131

VITA 148

LIST OF FIGURES

Figure 1.1 The *Eh–pH* diagram for arsenic at 25 °C and 101.3 kPa [4]..... 2

Figure 1.2 The number of published papers during 2005-2015 in ISI web of knowledge by using “nanocomposite” as a key word of topic search. (Accessed June 11, 2016)..... 4

Figure 2.1 Schematic of (a) a tetrahedron unit and (b) a tetrahedral sheet. (Adapted from ref. [87])..... 15

Figure 2.2 Schematic of (a) an octahedron unit and (b) an octahedral sheet. (Adapted from ref. [87])..... 16

Figure 2.3 Schematic of (a) a trioctahedral sheet and (b) a dioctahedral sheet. (Adapted from ref. [86])..... 16

Figure 2.4 The clay mineral structure of 1:1 and 2:1 layer types. (adapted from Brigatti et al . [85])..... 17

Figure 2.5 Flow chart demonstrates the formation of clay minerals [88]..... 19

Figure 2.6 The structure of brucite [$Mg(OH)_2$]. Dark balls are hydroxide anions and white balls are magnesium ions. [90]..... 20

Figure 2.7 Schematic of LDH structure [91]..... 21

Figure 2.8 Schematic of various polymer/clay structural configurations. (adapted from ref. [34])..... 27

Figure 2.9 Schematic of the preparation of polymer/clay via solution intercalation method. (Adapted from ref. [29])..... 28

Figure 2.10 Schematic of the synthesis of Nylon-6/clay nanocomposite. (Adapted from ref. [29])..... 29

Figure 2.11 Schematic of the constructive interference of reflected waves (reflected waves in phase, i.e., maxima are superimposed)..... 30

Figure 2.12 Schematic of the destructive interference of reflected waves (in the two reflected waves, maximum and minimum of the respective wave amplitude are superimposed). 31

Figure 2.13 Diagrammatic representation of isotherm classification [107]. 33

Figure 4.1 FTIR spectra of (a) Na-bentonite, (b) 15M1C0.5A30B and (c) pAPTMA-Cl. ... 48

Figure 4.2 XRD patterns of pAPTMACl/bentonite composites of (a) 7.5M1C0.5A30B, (b) 10M1C0.5A30B, (c) 12.5M1C0.5A30B, (d) 15M1C0.5A30B, (e) 17.5M1C0.5A30B, (f) 20M1C0.5A30B, (g) 22.5M1C0.5A30B, and (h) Na-bentonite 49

Figure 4.3 The d_{001} spacings and polymer amounts with varied monomer concentrations 49

Figure 4.4 The TGA graphs of Na-bentonite (- - -), pAPTMA-Cl (—), and pAPTMACl/bentonite composites before (– · · –) and after (– – –) As(V) adsorption. . 52

Figure 4.5 The polymer amount of pAPTMACl/bentonite composites before and after As(V) adsorption and their difference (Polymer lost). 53

Figure 4.6 The d_{001} spacings and As(V) adsorption amounts with varied monomer concentrations 54

Figure 4.7 XRD patterns of pAPTMACl/bentonite composites of (a) 15M0C0.5A30B, (b) 15M1C0.5A30B, (c) 15M2C0.5A30B, (d) 15M3C0.5A30B, (e) 15M4C0.5A30B, (f) 15M5C0.5A30B, and (g) Na-bentonite 55

Figure 4.8 The As(V) adsorption and d_{001} of pAPTMA/bentonite composites at various MBA concentrations 56

Figure 4.9 XRD patterns of pAPTMA/bentonite composites of (a) 15M1C0.5A30B, (b) 15M1C1A30B, (c) 15M1C2A30B, (d) 15M1C3A30B, (e) 15M1C4A30B, (f) 15M1C5A30B, and (g) Na-bentonite 57

Figure 4.10 The As(V) adsorption amount and d_{001} of pAPTMACl/bentonite composites at various APS concentrations. 58

Figure 4.11 XRD patterns of pAPTMACl/bentonite composites of (a) 15M1C2A5B, (b) 15M1C2A10B, (c) 15M1C2A20B, (d) 15M1C2A30B, (e) 15M1C2A40B, (f) 15M1C2A50B, (g) 15M1C2A60B, (h) 15M1C2A70B, and (i) Na-bentonite..... 59

Figure 4.12 The As(V) adsorption and d_{001} of pAPTMA/bentonite composites at various Na-bentonite concentrations. (15 %w/v APTMA-Cl, 1 %mole MBA, 2 %mole APS)..... 60

Figure 4.13 The d_{001} and polymer amounts of pAPTMA/bentonite composites at various Na-bentonite concentrations. (15 %w/v APTMA-Cl, 1 %mole MBA, 2 %mole APS)..... 61

Figure 4.14 FTIR spectra of (a) Na-bentonite, (b) 7.5M1C0.5A30B and (c) pAETMA-Cl..... 62

Figure 4.15 XRD patterns of pAETMACl/bentonite composites of (a) 7.5M1C0.5A30B, (b) 10M1C0.5A30B, (c) 12.5M1C0.5A30B, (d) 15M1C0.5A30B, and (e) Na-bentonite..... 64

Figure 4.16 The TGA graphs of Na-bentonite (- - -), pAETMA-Cl (—), and pAETMACl/bentonite composites (– · · –)..... 65

Figure 4.17 The As(V) adsorption and polymer amounts of pAETMA/bentonite composites with various monomer concentrations..... 66

Figure 4.18 XRD patterns of pAETMA/bentonite composites of (a) 10M0C0.5A30B, (b) 10M1C0.5A30B, (c) 10M2C0.5A30B, (d) 10M3C0.5A30B, and (e) Na-bentonite..... 67

Figure 4.19 the As(V) adsorption of pAETMA/bentonite composites at various MBA concentrations..... 68

Figure 4.20 XRD patterns of pAETMA/bentonite composites of (a) 10M1C0.5A30B, (b) 10M1C1A30B, (c) 10M1C2A30B, (d) 10M1C3A30B, (e) 10M1C4A30B, (f) 10M1C5A30B, and (g) Na-bentonite..... 69

Figure 4.21 The As(V) adsorption of pAETMA/bentonite composites at various APS concentrations..... 69

Figure 4.22 XRD patterns of pAETMA/bentonite composites of (a) 10M1C0.5A5B, (b) 10M1C0.5A10B, (c) 10M1C0.5A20B, (d) 10M1C0.5A30B, (e) 10M1C0.5A40B, (f) 10M1C0.5A50B, (g) 10M1C0.5A60B, (h) 10M1C0.5A70B, and (i) Na-bentonite. 71

Figure 4.23 Polymer amount and d_{001} of pAETMA/bentonite composites at various Na-bentonite concentrations. 71

Figure 4. 24 The As(V) adsorption amount and d_{001} of pAETMA/bentonite composites at various Na-bentonite concentrations. (10 %w/v AETMA-Cl, 1 %mole MBA, 0.5 %mole APS) 73

Figure 4.25 FTIR spectra of (a) Na-bentonite, (b) 1C0.5A10B and (c) pAPTMA-Cl. 74

Figure 4.26 XRD patterns of pAPTMA/bentonite composites of (a) 0C0.5A10B, (b) 1C0.5A10B, (c) 3C0.5A10B, (d) 5C0.5A10B and (e) Na-bentonite. 76

Figure 4.27 The d_{001} spacings of composites with varied MBA cross-linker concentrations 77

Figure 4.28 The TGA graphs of Na-bentonite (- - -), pAPTMA-Cl (—), and pAPTMACl/bentonite composites (– – –). 78

Figure 4.29 The d_{001} spacings and As(V) adsorption amounts with varied MBA concentrations 79

Figure 4.30 XRD patterns of pAPTMA/bentonite composites of (a) 3C0.25A10B, (b) 3C1A10B, (c) 3C3A10B, (d) 3C5A10B and (e) Na-bentonite. 80

Figure 4.31 The As(V) adsorption amount of pAPTMA/bentonite composites at various APS concentrations. 81

Figure 4.32 XRD patterns of pAPTMA/bentonite composites of (a) Na-bentonite (b) 1C0.5A76B, (c) 1C0.5A67B, (d) 1C0.5A57B, (e) 1C0.5A47B, (f) 1C0.5A36B, (g) 1C0.5A25B, (h) 11C0.5A22B, (i) 1C0.5A19B, (j) 1C0.5A16B, (k) 1C0.5A13B, (l) 1C0.5A10B, (m) 1C0.5A7B and (n) 1C0.5A4B. 82

Figure 4.33 The As(V) adsorption amount and d001 of pAPTMACl/bentonite composites at various Na-bentonite concentration. 83

Figure 4.34 FTIR spectra of (a) Na-bentonite, (b) 3C0.5A7.5B and (c) pAETMA-Cl. 84

Figure 4.35 XRD patterns of pAETMA/bentonite composites of (a) 0C0.5A7.5B, (b) 1C0.5A7.5B, (c) 3C0.5A7.5B, (d) 5C0.5A7.5B and (e) Na-bentonite. 86

Figure 4.36 The TGA graphs of Na-bentonite (- - -), pAETMA-Cl (—), and pAETMA/bentonite composites (– – –). 87

Figure 4.37 The d_{001} spacings and As(V) adsorption amounts with varied MBA concentrations 88

Figure 4.38 XRD patterns of pAETMACl/bentonite composites of (a) 3C0.5A7.5B, (b) 3C1A7.5B, (c) 3C3A7.5B, (d) 3C5A7.5B and (e) Na-bentonite 89

Figure 4.39 The As(V) adsorption amount of pAETMA/bentonite composites at various APS concentrations. 90

Figure 4.40 XRD patterns of pAPTMA/bentonite composites of (a) Na-bentonite (b) 1C0.5A22.5B, (c) 1C0.5A20B, (d) 1C0.5A17.5B, (e) 1C0.5A15B, (f) 1C0.5A12.5B, (g) 1C0.5A10B, (h) 11C0.5A7.5B and (i) 1C0.5A5B. 91

Figure 4.41 The As(V) adsorption amount and d_{001} of pAETMA/bentonite composites at various Na-bentonite concentrations. 92

Figure 4.42 The As(V) removals from aqueous solution at various dosages using 15M1C2A30B (APSI) and 10M1C0.5A40B (AESI) nanocomposite. (C_0 = 50 mg/L, the contact time = 24 hour) 94

Figure 4.43 The effect of contact time on As(V) adsorption onto 15M1C2A30B composite(APSI) and 10M1C0.5A40B composite(AESI). 96

Figure 4.44 Schematic of the sorption mechanism step i, showing the transportation of the solute from bulk solution to the film surrounding the adsorbent. 96

Figure 4.45 Schematic of the sorption mechanism step ii, showing the transportation of the solute from the film to the adsorbent surface. 97

Figure 4.46 Schematic of the proposed sorption mechanism step iii, showing the As(V) adsorption onto the nanocomposites. 97

Figure 4.47 Linear plots of (a) pseudo-first-order kinetic model and (b) pseudo-second-order kinetic model of 15M1C2A30B nanocomposite (APSI). 98

Figure 4.48 Linear plots of (a) pseudo-first-order kinetic model and (b) pseudo-second-order kinetic model of 10M1C0.5A40B nanocomposite (AESI). 99

Figure 4.49 The adsorption of As(V) on nanocomposites in various pH. (C_0 = 50 mg/L, the contact time = 6 h) 101

Figure 4.50 Schematic of the As(V) adsorption by APSI at pH =11. 101

Figure 4.51 As(V) adsorption isotherm of APSI and AESI nanocomposites. (pH 9, the contact time = 6 hour) 103

Figure 4.52 Langmuir isotherm plot (a) and Freundlich isotherm plot (b) of APSI nanocomposite. 103

Figure 4.53 Langmuir isotherm plot (a) and Freundlich isotherm plot (b) of AESI nanocomposite. 104

Figure 4.54 Schematic of the pAPTMA-Cl and pAETMA-Cl Structures. 104

Figure 4.55 The As(V) adsorption on 15M1C2A30B composite (APSI) with difference competing anions. (C_0 = 50 mg/L, the contact time = 24 hour) 105

Figure 4.56 The As(V) adsorption on 10M1C0.5A40B composite (AESI) with difference competing anions. Dash line is the As(V) adsorption amount with no competing anion. (C_0 = 50 mg/L, the contact time = 24 hour) 106

Figure 4.57 Arsenic removal from wastewater samples (a) TK80 and (b) TK81 using polymer/bentonite nanocomposites. 107

Figure 4.58 XRD patterns of (a) Fe_3O_4 and (b) cal-Fe_3O_4 108

Figure 4.59 XRD patterns of $[Mg_{0.66}Fe_{0.33-x}Zr_x(OH)_2](CO_3)_\delta$ (x = 0 – 0.33) 109

Figure 4.60 XRD patterns at various region of $[Mg_{0.66}Fe_{0.33-x}Zr_x(OH)_2](CO_3)_\delta$ (x = 0 – 0.33) 109

Figure 4.61 The unit cell parameters of $[Mg_{0.66}Fe_{0.33-x}Zr_x(OH)_2](CO_3)\delta$ (x = 0 – 0.33). 110

Figure 4.62 The As(V) adsorption amounts of $[Mg_{0.66}Fe_{0.33-x}Zr_x(OH)_2](CO_3)\delta$ (x = 0 – 0.33). (C_0 = 150 ppm, pH = 6, shaking time = 18 h at 30 rpm) 110

Figure 4.63 XRD patterns of (a) Fe_3O_4, (b) calcined Fe_3O_4, (c) LDH, (d) as-synthesized m-LDH composite, (e) c-LDH and (f) cm-LDH. 112

Figure 4.64 TEM images of m-LDH (a) with scale bar of 0.5 μm and (b) the enlarge of the square box in (a). 112

Figure 4.65 TEM images of cm-LDH: (a) with scale bar of 0.5 μm and (b) the enlarge of the square area in (a). 113

Figure 4.66 SEM-EDX of cm-LDH showing (a) particles, and the distributions of (b) Zr atoms, (c) Mg atoms and (d) Fe atoms. 113

Figure 4.67 Magnetization hysteresis curves of (a) Fe_3O_4 and (b) cm-LDH. 114

Figure 4.68 Nitrogen adsorption/desorption isotherms of (a) Fe_3O_4, (b) calcined Fe_3O_4, (c) Mg-Fe-Zr LDH, (d) calcined Mg-Fe-Zr LDH (c-LDH), (e) as-synthesized m-LDH composite, and (f) cm-LDH. 115

Figure 4.69 Demonstration of the magnetic separation of cm-LDH in aqueous As(V) solution (a) without and (b) with an external magnetic field 118

Figure 4.70 The pH buffer capacities of cm-LDH and the adsorption of As(V) on cm-LDH in various pH solutions. (C_0 = 200 mg/L, the contact time = 3 days) 119

Figure 4.71 The adsorption of As(V) onto cm-LDH as a function of (pH_{eq} – pH_{int}). (C_0 = 200 mg/L, contact time = 3 days) 119

Figure 4.72 The effect of contact time on As(V) adsorption onto cm-LDH, (a) up to 8 h and (b) up to 120 h. 121

Figure 4.73 Linear plots of pseudo-first-order kinetic model of cm-LDH composite, (a) up to 8 h and (b) up to 120 h. 121

Figure 4.74 Linear plots of pseudo-second-order kinetic model of cm-LDH composite, (a) up to 8 h and (b) up to 120 h. 121

Figure 4.75 XRD patterns of the (a) as-synthesized m-LDH composite, (b) cm-LDH and (c) cm-LDH after As(V) adsorption 122

Figure 4.76 Schematic mechanism of As(V) adsorption by cm-LDH 122

Figure 4.77 As(V) adsorption isotherm of cm-LDH. 123

Figure 4.78 Langmuir isotherm plot of cm-LDH. 124

Figure 4.79 Freundlich isotherm plot of cm-LDH. 124

Figure 4.80 As removal from wastewater samples TK80 (a) and TK81 (b) from the oil company in Thailand. 125

LIST OF TABLES

Table 2.1 Distinction between clay and clay mineral [85] 14

Table 2.2 The possible polytypes for all stacking sequences [89] 22

Table 2.3 The IUPAC classification of pores [104-106]. 33

Table 4.1 FTIR spectral assignment of Na-bentonite, 15M1C0.5A30B and pAPTMA-Cl 47

Table 4.2 Literature reviews on temperature degradation assignments of bentonite, polymers and organic/clay. 51

Table 4.3 FTIR spectral assignments of Na-bentonite, 7.5M1C0.5A30B and pAETMA-Cl 63

Table 4.4 FTIR spectral assignments of Na-bentonite, 1C0.5A10B and pAPTMA-Cl 75

Table 4.5 FTIR spectral assignments of Na-bentonite, 3C0.5A7.5B and pAETMA-Cl 85

Table 4.6 Polymer/bentonite composites with the best performances from each methods. 93

Table 4.7 Adsorption kinetic parameters of As(V) adsorption onto 15M1C2A30B nanocomposites 99

Table 4.8 Isotherm parameters of As(V) adsorption onto the 15M1C2A30B nanocomposite(APSI) and 10M1C0.5A40B(AESI) 104

Table 4.9 The saturated magnetization of various magnetic composites 114

Table 4.10 Surface area and As(V) adsorption amounts of the LDH, Fe_3O_4 and composites 117

Table 4.11 Adsorption kinetic parameters of As(V) adsorption onto the cm-LDH composite 122

Table 4.12 Isotherm parameters of As(V) adsorption onto the cm-LDH composite 124

LIST OF ABBREVIATIONS

APTMA-Cl	(3-acrylamidopropyl)trimethylammonium chloride
AETMA-Cl	[2-(acryloyloxy)ethyl]trimethylammonium chloride
pAPTMA-Cl	Poly(3-acrylamidopropyl)trimethylammonium chloride
pAETMA-Cl	Poly[2-(acryloyloxy)ethyl]trimethylammonium chloride
CEC	Cation-exchanged capacity
LDHs	Layered double hydroxides
c-LDH	Calcined LDH
m-LDH	Magnetic LDH composite
cm-LDH	Calcined magnetic LDH composite
XRD	X-Ray Diffraction
VSM	Vibrating sample magnetometer
TEM	Transmission electron microscopy
SEM-EDX	Scanning electron microscopy with energy dispersive X-ray spectroscopy
TGA	Thermogravimetric analysis or thermal gravimetric analysis
FTIR	Fourier transform infrared spectroscopy
ICP-OES	Inductively coupled plasma optical emission spectrometry
BET	Brunauer-Emmett-Teller
Q_e	The adsorption capacity at equilibrium (mg/g)
Q_t	The adsorption capacity at time *t* (mg/g)
Q_m	The maximum adsorption capacity (mg/g)
C_{eq}	The equilibrium concentration (mg/L)
C_0	the initial concentration (mg/L)
C_t	the concentration at time *t* (mg/L)
K_L	The Langmuir adsorption constant
R_L	The separation factor or equilibrium parameter
K_F	The Freundlich constant
TEMED	*N,N,N′,N′*-tetramethylethylenediamine

MBA *N,N'*-methylenebisacrylamide

APS Ammonium persulfate

APSI The pAPTMA/bentonite nanocomposite prepared via solution intercalation method

AESI The pAETMA/bentonite nanocomposite prepared via solution intercalation method

CHAPTER 1
INTRODUCTION

1.1 Fundamental of arsenic

Arsenic is the 33th element in periodic table and resides in group 15 with the oxidation states of -3, 0, +3 and +5 [1, 2]. It can be found in various species such as H_3AsO_3, H_3AsO_4, $H_2AsO_4^-$, $HAsO_4^{2-}$, AsO_4^{3-} [2], and exists in more than 245 minerals [3]. Arsenic is a highly toxic element. According to the World Health Organization (WHO), the guideline for arsenic concentration in drinking water should lower than 10 ug/L. Unfortunately, the two main inorganic arsenic species, arsenite As(III) and arsenate As(V), are commonly found in water supplies [2]. The species of inorganic arsenic are controlled by pH in solution as shown in Figure 1.1. The sources of arsenic can be divided to two groups, natural sources and human activities. The former sources normally exist in earth crusts, soil, sediments, water, air and living organisms before man activities. The later sources release arsenic three times of the natural sources as the components in insecticides, herbicides, desiccants and wood preservatives [3]. Long-term up take of arsenic can cause human carcinogen (including cancer for skin, lungs, urinary bladder, liver, kidney), pigment change, skin thickening (hyperkeratosis), neurological disorders, muscular weakness, loss of appetite, and nausea [1, 2].

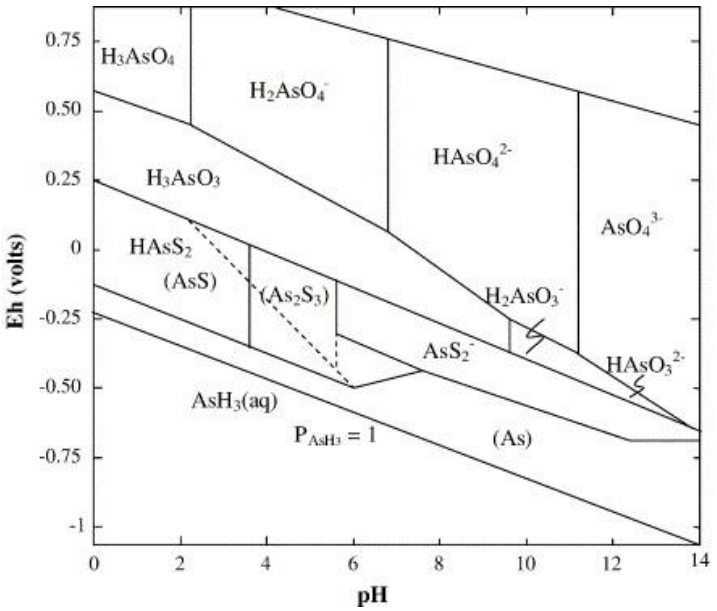

Figure 1.1 The *Eh–pH* diagram for arsenic at 25 °C and 101.3 kPa [4].

Many techniques have been used for the removal of arsenic from water such as chemical precipitation, reverse osmosis, electrodialysis, electrolysis, agulation and flocculation, adsorption, ion exchange, and membrane filtration [1, 5-15]. The most popular method is adsorption because of its simplicity, ease of preparation, low cost, high efficiency, and reusability. Many research studies proposed the use of various materials for arsenic adsorption, such as agriculture products, metal oxides, activated alumina, activated carbon, layered double hydroxides, polymer composites, and novel hybrid materials [16-26].

1.2 Composite

Composites are materials containing more than one component and forming a solid multiphase. Composite materials are aimed to combine the desired properties of each individual components [27]. Similarly, nanocomposites are the solid multiphase materials that at least one dimension of building blocks of one phase is in the scale of nanometer (<100 nm) [27-32]. The interfacial interaction between each component therefore is dramatically increased, resulting to the improve in mechanical, electrical, thermal, optical, electrochemical, and catalytic properties [32]. Nanocomposites have been widely studied during last decades, as

observed from the increasing numbers of publications (Figure 1.2). Nanocomposites can be grouped based on their matrix materials; ceramic-matrix nanocomposites, metal-matrix nanocomposites, and polymer-matrix nanocomposites [32]. Their applications are widely investigated and commercially applied in many fields, for example, construction, pharmacy, energy storage, and environment. The polymer-matrix nanocomposites have received more attention due to the advantage properties of polymer counterparts, especially polymer hydrogel, such as swellability in water, hydrophilicity, biocompatibility and lack of toxicity. Polymer hydrogels have gain interest in wastewater treatment due to their high adsorption capacities, especially regeneration abilities and reuse for continuous processes. However, pure polymer hydrogels often have some limitations such as low mechanical stability and gel strength [33]. Thus it is important to incorporate dispersed phase (or filler) with polymer to form polymer-matrix nanocomposites. A wide range of fillers are used such as TiO_2, carbon nanotubes, layered silicate and layered double hydroxides [32]. Amongst them, those based on clay and layered silicates have been more widely investigated. This should be due to that the starting clay materials are naturally available and easily regenerated. Moreover their intercalation chemistry has been studied for a long time [33, 34].

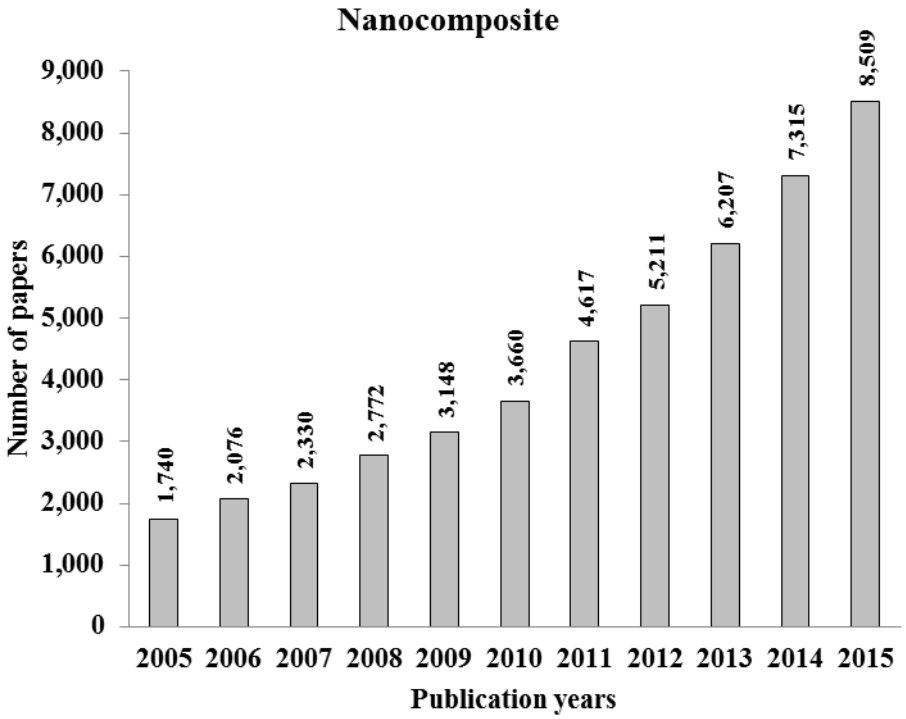

Figure 1.2 The number of published papers during 2005-2015 in ISI web of knowledge by using "nanocomposite" as a key word of topic search. (Accessed June 11, 2016)

1.3 Clay minerals

Clay minerals have a potential for use as adsorbents since they can be easily obtained and regenerated. Moreover they are low cost, highly abundant, highly sorptive and ion-exchangeable [33] which make them suitable as adsorbents.

Clay materials are naturally occurrence aluminosilicates with the average size of 2 μm and frequently used as inorganic filler in polymer nanocomposites because of its economic cost and biocompatibility. They possess high surface area and structural strength that are suitable as adsorbents for the removal of toxic contaminants. Bentonite is a type of clay that contains montmorillonite as a major component [35, 36]. Montmorillonite is a member of a smectite 2:1 phyllosilicate group of clays. Many applications and new materials are developed based on these smectite clays: montmorillonite, hectorite and saponite [33]. Montmorillonite contains negative-charged layers with cations between layers. Each layer is comprised of one alumina octahedral sheet sandwiched in between two silica

tetrahedral sheets [33, 37]. The negative charge of each layer is a result of the partially substitution of Al^{3+} by Mg^{2+}or Fe^{2+} [38, 39]. Therefore, the structure requires cations, such as Ca^{2+}, Na^{+} etc. to balance the negative charges. Moreover, it is well known that montmorillonite exhibits good swelling property because of their weak electrostatic force and van de Waals force which held each layer together [38, 40]. As a result, montmorillonite has an interesting property of cation exchange between its layered structures. From the literature, the cation-exchanged capacity (CEC) of montmorillonite is reported between 0.80-1.50 meq/g [41]. Using bentonite as adsorbents for removal of toxic cations through ion-exchange has been widely studied. However, bentonite itself cannot adsorb toxic anions such as chromate, arsenite and arsenate anions. Therefore, the surface modification of bentonite is required.

Another type of clay minerals is layered double hydroxides (LDHs). LDHs have become the prime candidates for arsenic removal with arsenic adsorption capacities in the range of 5-615 mg/g, due to their hydrophilic nature and cationic layered structures [42]. LDHs are known as synthetic clays or anionic-clay with many similarities to natural clays, including the layered structure, wide chemical compositions, variable charge density, ion exchange capabilities, high surface area, structural stability, reactive in interlayer space, swelling in water, and rheological and colloidal properties [42-45]. On the contrary to clays, LDH layers consist of positive charges with anions between the interlayer regions [46]. Therefore, the adsorption of arsenic from wastewater can occur on the external surfaces of these materials through physisorption and between the interlayer regions through ion exchange.

1.4 Polymer/clay nanocomposites

Polymers were applied in various fields because of their good unique properties compared with other materials such as light weight, ductility, ease of preparing and handling [27]. Some polymers can separate to be ionic polymer in aqueous solution, for example, poly(3-acrylamidopropyl)trimethylammonium chloride, poly[2-(acryloyloxy)ethyl]trimethylammonium chloride, and chitosan [47-

49]. Therefore, those ionic polymers can adsorb toxic anions from aqueous solution such as As(III), As(V), Cr(VI), PO_4^{3-}, Hg(II) [49-52].

1.4.1 The advantage of polymey/clay nanocomposites over individual parts

The clay-polymer nanocomposites (CPNs) were considered as the candidate adsorbent materials because of their simple production, excellent performance, and low cost. Several studies on nanocomposites reveal the advantages of polymer/clay nanocomposites over neat clay and polymer individuals as adsorbents for water treatment.

The adsorption capacities of polymer/clay nanocomposites exhibited higher adsorption capacity and longer life cycle [15, 53, 54]. Kaşg**Ö**z et al. [53] reported that the AAm-AMPS/clay nanocomposites containing 10% wt of clay showed higher degree of swelling and higher heavy metal ions (Cu^{2+}, Cd^{2+}, and Pb^{2+}) adsorption capacities than each component alone. A similar result was reported by Kaplan and Kasgoz [54] that nanocomposite containing 3% wt montmorillonite exhibited 9.0% higher adsorption capacity of brilliant cresyl blue (BCB) than the copolymer alone.

Several reports showing that the polymer/clay nanocomposite used faster treatment time than both polymer and clay did. Unuabonah and Taubert [15] reported that clay-polymer nanocomposites showed faster treatment time than both polymer and clay did. Kaplan and Kasgoz [54] synthesized the nanocomposite containing acrylamide, itaconic acid, polyethyleneglycol (400) diacrylate, and montmorillonite by *in situ* polymerization technique. They found that nanocomposite containing 3% wt montmorillonite exhibited slightly faster treatment time for the adsorption of 30 min.

Furthermore, the polymer/clay nanocomposite exhibited superior properties over polymer alone and clay alone. Urbano and Rivas [55] synthesized two polymer/montmorillonite nanocomposites. They found that both nanocomposites, poly(sodium 4-styrene sulfonate) and poly(2-acrylamide glycolic acid) containing 2.5% wt montmorillonite exhibited better deformation resistance, stability for

different stress frequencies, diminished compliance and elastic recovery compared with polymer alone. Güçlü et al. [56] prepared the nanocomposite of Starch-graft-acrylic acid/montmorillonite and used it as Cu^{2+} and Pb^{2+} adsorbents. Although the adsorption of their nanocomposite and polymer hydrogel alone did not show a significant difference in adsorption capacities, but including montmorillonite into polymer hydrogel could dramatically increase mechanical properties as a shear moduli increased. As a result, nanocomposites could be regenerated while polymer hydrogel could not. Irani et al. [57] synthesized the composite of polyethylene, acrylic acid and modified montmorillonite via emulsion polymerization procedure. They found that the nanocomposite containing 3% wt modified montmorillonite showed better swelling rate than bulk polymer. Starodoubtsev et al. [58] synthesized the composite of poly(acrylamide) and bentonite by *in situ* polymerization method. They found that the composite did not coagulate with cationic surfactant like pure bentonite did. Moreover, polymer/clay nanocomposites were easier to separate from solution than neat clay [15]. KaşgÖz et al. [53] exhibited that nanocomposites of the acrylamide (AAm)- 2-acrylamido2-methylpropane sulfonic acid (AMPS) sodium salt and clay were successful prepared by *in situ* copolymerization, and the nanocomposite containing 10% wt of clay showed better swelling capacity.

1.4.2 Polymer/clay nanocomposites as adsorbent for contaminants removals

The polymer/clay nanocomposites can remove various types of contaminants depending on their polymer counterparts, for example, microorganism, inorganic and organic macropollutants, and heavy metal ions [15, 53, 56, 59-61].

Some of polymer/clay nanocomposites were aimed as heavy metal ions adsorbents. For example, the nanocomposite of acrylamide (AAm)- 2-acrylamido2-methylpropane sulfonic acid (AMPS) sodium salt and clay was used to remove Cu (II), Cd (II), and Pb (II) from aqueous solution [53]. Güçlü et al. [56] prepared the nanocomposite of Starch-graft-acrylic acid/montmorillonite and used it as Cu^{2+} and Pb^{2+} adsorbents. Futalan et al. [62] prepared chitosan immobilized on bentonite by

solution intercalation and used it as heavy metal adsorbent, and claimed this composite is a candidate inexpensive large-scale barrier filters for the treatment of heavy metals contaminations in wastewater or groundwater plumes. Bulet et al. [63] synthesized the cheap and highly selective poly(acrylic acid)/bentonite nanocomposite for the removal of heavy metal ions through *in situ* polymerization method. The nanocomposite shows good ability to adsorb Pb(II), Ni(II), Cd(II), and Cu(II). Mansri et al. [64] synthesized the composite of poly(4-vinylpyridine) and bentonite via solution intercalation. They found that the composite exhibited good efficiency in removing Cr(VI) from aqueous solution at low pH. Natkaǹski et al. [65] synthesized the nanocomposites of montmorillonite with poly(sodiumacrylate), polyacrylamide and their copolymers via *in situ* polymerization procedure. They reported that at polymer-to-clay mass ratio of 1:1, all nanocomposites were intercalated products. The highest adsorption of Fe(III) ions was belong to the nanocomposite containing poly(sodiumacrylate) because of the presence of carboxyl groups and high swelling capacity.

The studies on the removal of organic pollutants were done using several of polymer/clay nanocomposites such as the removals of atrazine by poly (4-vinylpyridine-co-styrene)-montmorillonite [59], of cationic dyes by humic acid-immobilized amine modified polyacrylamide/bentonite composite (HA-Am-PAA-B) [60], of trinitrophenol and trichlorophenol by PVPcoS - and PDADMAC–MMT [61].

According to previous research studies; many research studies deal with the nanocomposites contain uncharged and negative charged polymer, thus most focused on the removals of cation contaminants. The nanocomposites contain positively charge polymer were rarely reported.

1.4.3 Polymer/clay nanocomposites with polycations

There are a few reports on the nanocomposites containing polycations and cationic molecules. For example, the nanocomposite of montmorillonite and polydiallyl dimethylammonium chloride (PDADMAC) was successful synthesized through solution intercalation method by Ganigar et al. [61]. Lvov et al. [66]

successful prepared the nanocomposite of montmorillonite and linear polycation poly(ethylenimine) (PEI) or poly(dimethyldiallylammonium chloride) (PDDA) via layer-by-layer method. Li et al. [67] modified the surface of zeolite and kaolinite with cationic surfactant, hexadecyltrimethylammonium. As a result, negative charges on the surface of zeolite and kaolinite were modified to positive charges of cationic surfactants. Consequently, the ability to adsorb arsenate anions compared to very low abilities of the unmodified materials was tremendously improved. Li et al. [68] also synthesized the composite of polyepicholorohydrin-dimethylamine (EPIDMA) and bentonite via solution intercalation technique and used it as the reactive yellow K-4G (RY K-4G) and the disperse yellow brown S-2RFL (DYB S-2RFL) dye adsorbents.

1.4.4 Cationic polymer for anion contaminants removal

Interesting polycations that showed high anion adsorption capacities are review below.

1.4.4.1 Poly(3-acrylamidopropyl)trimethylammonium chloride (pAPTMA-Cl)

Barakat and Sahiner [49] synthesized poly(3-acrylamidopropyl) trimethylammonium chloride via radical polymerization and shaped it into cylinder with a diameter of 0.8 cm and 5 mm-long. The polymer cylinder showed high removal efficiency of As(V) of 99.7% from aqueous solution containing 50 mg/L As(V) at pH 9. Kusku et al. [51] used poly[(4-vinylbenzyl) trimethylammonium chloride] P(ClVBTA) and poly[(3-acrylamidopropyl) trimethyl ammonium chloride] P(ClAPTA) for the removal of Cr(VI) from aqueous solution. They found that the polymers exhibited greater and faster sorption rates than a commercially available ion exchange resin Amberlite IRA-400. Constantin et al. [69] modified the surface of Pullulan with poly(3-acrylamidopropyl)trimethylammonium chloride. They reported that the modified Pullulan could adsorb anionic dyes with high adsorption capacity up to 113.63 mg/g. Yatin et al. [70] synthesized poly (3-acrylamidopropyl)-trimethylammonium chloride-co-N,N-dimethylacrylamide by free radical polymerization of APTAC and DMAAm

monomers in a presence of *N,N´*-methylenebisacrylamide as a crosslinking agent. They reported that dye adsorption occurred via strong interaction of the negatively charged (– SO_3Na) groups of the dye molecules with both the uncharged (– NMe_2) of DMAAm and the positively charged (– NMe_3^+) of APTAC of crosslinked SAH chain.

According to literature reviews above, poly(3-acrylamidopropyl) trimethylammonium (pAPTMA) cation containing amide and amino groups was of interest because they provide a positive charge in aqueous solution and could attract toxic anions such as arsenate anion with a high capacities.

1.4.4.2 Poly[2-(acryloyloxy)ethyl]trimethylammonium chloride (pAETMA-Cl)

Rivas et al. [47] prepared poly[3-(methacryloylamino)propyl]trimethyl ammonium chloride, poly[2-(acryloyloxy)ethyl]trimethylammonium chloride, and poly(ar-vinylbenzyl)trimethylammonium chloride and tested the polymers for arsenate removal using liquid-phase polymer-based retention technique. They found that poly[3-(methacryloylamino)propyl]trimethylammonium chloride and poly[2-(acryloyloxy)ethyl]trimethylammonium chloride can remove arsenate up to 100% when initial concentration of arsenate in cell was as low as 5.5 mg/L.

Since MOTA and AETMA-Cl structures are quite similar with the difference of one methyl group at the double bond carbon. Morales et al.[71] synthesized the Poly([(2-methacryloyloxy)ethyl]trimethylammonium chloride) resin P(MOTA) through radical polymerization and used it as As(V) adsorbent. They showed that P(MOTA) exhibited higher As(V) adsorption capacity than Amberlite IRA-400(Cl) commercial resin. They described that the higher capacity of the P(MOTA) resin over Amberlite IRA-400(Cl) was due to the higher degree of swelling than Amberlite IRA-400(Cl) and a different structure of P(MOTA) resin over Amberlite IRA-400(Cl).

According to literature reviews above, poly[2-(acryloyloxy)ethyl]trimethyl ammonium (pAETMACl) cation which contains amide group was of interest because it provided a positive charge in aqueous solution and could attract toxic anions such as arsenate anion with a high capacities.

However, both polymers, pAPTMA-Cl and pAETMA-Cl, are water soluble. Therefore, the polycation/clay nanocomposites of pAPTMA or pAETMA with bentonite were prepared and tested the arsenic adsorption ability. Here, bentonite with the property of high surface area and stable oxide compounds would play the role of supporter and distributor of polymer components. These two nanocomposites are expected to be the adsorbents for arsenate anion from aqueous solution.

1.5 Magnetic layered double hydroxides composites

1.5.1 Layered double hydroxides

LDHs are known as synthetic clays with many similarities to natural clays, including the layered structure, ion exchange capabilities, high surface area, topotactic reactions and structural stability [42, 44, 45]. On the contrary to clays, LDH layers consist of positive charges with anions between the interlayer regions [46]. Therefore, the adsorption of arsenic from wastewater can occur on the external surfaces of these materials through physisorption and between the interlayer regions through ion exchange. The drawback to this approach is the difficulty in collecting dispersed LDH particles in aqueous solution after the removal process. Several reports have shown that Zr has a high affinity to both As(III) and As(V) [72-74]. Chitrakar et al. [75] reported that Mg-Fe-Zr LDH showed better phosphate removal than amorphous ZrO_2 and MgFe LDH. Mandel et al. [76] synthesized various types of LDHs deposited on SiO_2/Fe_3O_4 particles and reported that the deposition of Mg-Fe-Zr LDH led to the best phosphate adsorption ability. As arsenate is isoelectronic and isostructural with phosphate [77], therefore, Mg-Fe-Zr LDH could be selected as an active phase for arsenate removal in this work.

1.5.2 Magnetite (Fe_3O_4)

Liu et al. [78] demonstrated the mechanism of arsenic adsorption on magnetite nanoparticles and they reported that magnetite nanoparticles have a high

affinity to both As(III) and As(V). However, magnetite itself has a low surface area and therefore low As(V) adsorption capacity is expected [79, 80]. Song et al. [79] reported that the As(V) adsorption capacity of magnetite is 8.8 mg/g with a BET surface area of 40 m^2/g. Furthermore, Fe_3O_4 could be oxidized to α-Fe_2O_3 at high temperatures or in an oxidizing environment, resulting in the loss of magnetic response [81]. According to the literature, therefore, iron magnetite (Fe_3O_4) was chosen due to its ease of preparation, availability and environmental friendliness.

1.5.3 Composite of magnetite and LDHs

The research areas on the magnetic layered hydroxides had attracted many researchers because of their environmental friendly nature and ease of recovery. Toledo et al. [82] synthesized the magnetic hydrotalcite-iron oxide composite and used it as As(V) adsorbent. They reported that the composite exhibited both ion-exchange and magnetic properties. The maximum adsorption capacity of 24.09 mg/g was obtained at pH value of 4. Turk and Alp [19] prepared the Fe-hydrotalcite supported magnetite nanoparticle via co-precipitation method and applied it in the removal of As(III) and As(V). They reported that the obtained product consisted of magnetite, maghemite, hydrotalcite, and pyrouaurite-2H phases. This composite can remove As(III) and As(V) up to 95%. Zhang et al. [83] synthesized magnetic Fe_3O_4@C@MgAl-layered double-hydroxide by the chemical self-assembly method and used it as Cr(VI) adsorbent. The composite exhibited high Cr(VI) adsorption of 152.0 mg/g at 40°C and pH 6.0. Mandel et al. [76] synthesized various types of LDHs deposited on SiO_2/Fe_3O_4 particles and reported that the deposition of Mg-Fe-Zr LDH led to the best phosphate adsorption ability.

Although several reports revealed the synthesis of magnetic layered double hydroxides composite for the removal of contaminant; however, the removal of arsenic using the magnetic Mg-Fe-Zr layered double hydroxides had not been studied before. In this work, a Mg-Fe-Zr LDH/Fe_3O_4 composite was synthesized in an attempt to combine the magnetic properties of Fe_3O_4 and the high As(V) adsorption capacity of the LDH.

1.6 The objectives of this study

1.6.1 To synthesized the nanocomposites of polycations and bentonite.

1.6.2 To investigate the removal of arsenate from aqueous solution and real wastewater using the as-synthesized nanocomposites.

1.6.3 To synthesized the magnetic layered double hydroxide composite.

1.6.4 To investigate the removal of arsenate from aqueous solution and real wastewater using as-synthesized composites.

1.6.5 To studies the arsenate adsorption behavior of the polymer/bentonite nanocomposites and the magnetic layered double hydroxide composite.

CHAPTER 2

THEORY

2.1 Clay and clay minerals

The joint nomenclature committees (JNCs) of the Association Internationale pour l'Etude des Argiles (AIPEA) and the Clay Minerals Society (CMS) have defined *clay* as "a naturally occurring material composed primarily of fine-grained minerals, which is generally plastic at appropriate water contents and will harden with dried or fired". Clay usually contains phyllosilicates (from the Greek "phyllon": leaf, and from the Latin "silic": flint), i.e. silicate material which has a sheet-like structure, and may contain other materials that impart plasticity and harden when dried or fired. Associated phases in clay may include materials that do not impart plasticity and also organic matter [84, 85]. The term *clay mineral* have been defined as "phyllosilicate minerals and to minerals which impart plasticity to clay and which harden upon drying or firing" [84, 85]. There are many types of clays depending on their origin and main clay mineral substituents includes ball clay, bentonite, China clay, fire clay, kaolin, etc. Some clay minerals, for example, include kaolinite, montmorillonite, palygorskite, sepiolite, layered double hydroxides (LDHs), etc. Clay minerals are found to be the main constituents of clays, for example, bentonite composed of mainly montmorillonite [85]. The distinction between clay and clay mineral is demonstrated in Table 2.1.

Table 2.1 Distinction between clay and clay mineral [85]

Clay	Clay mineral
Natural	Natural and synthetic
Fine-grained (<2 μm or <4 μm)	No size criterion
Phyllosilicates as principal constituents	May in clude non-phyllosilicates
Plastic[a]	Plastic
Hardens on drying or firing	Hardens on drying or firing

[a]with some exception like flint clays

Clay minerals can be classified into two group upon their ions exchange properties, cationic clays (conventional phyllosilicates with a negative layer charge) and anionic clays (layered double hydroxides (LDHs) with a positive layer charge) [85].

2.1.1 Conventional phyllosilicates

The basic building block for pillosilicate minerals are tetrahedron consisting of a cation coordinated to four oxygen atoms (T unit) and octahedron consisting of a cation coordinated to six oxygen atoms (O unit). Each T unit is linked to other three T units by sharing three corner oxygen atoms to form an infinite two-dimentional mesh pattern along the *a, b* crystallographic directions as shown in Figure 2.1. The O units link to each other by edge sharing to form hexagonal octahedral sheet along the *a, b* crystallographic directions as shown in Figure 2.2. Common cations occupied in tetrahedron unit are Si^{4+}, Al^{3+}, and Fe^{3+} while common cations occupied in octahedron unit are Al^{3+}, Fe^{3+}, Mg^{2+}, and Fe^{2+} [86]. There are two forms of octahedral sheet, trioctahedral sheet and dioctahedral sheet, as shown in Figure 2.3. In trioctahedral sheet, cations are divalent (usually Mg^{2+} or Fe^{2+}) and the – 6 charge from the anions is balanced by three divalent cations. Therefore all cation sites are filled. In case of divalent octahedral, cations are trivalent (usually Al^{3+}) in with the – 6 charge from the anions is balanced by only two trivalent cations, hence one out of every three cation sites is vacant.

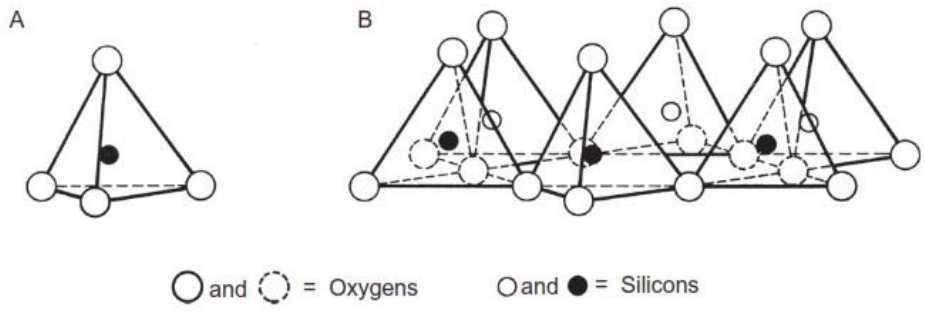

Figure 2.1 Schematic of (a) a tetrahedron unit and (b) a tetrahedral sheet. (Adapted from ref. [87])

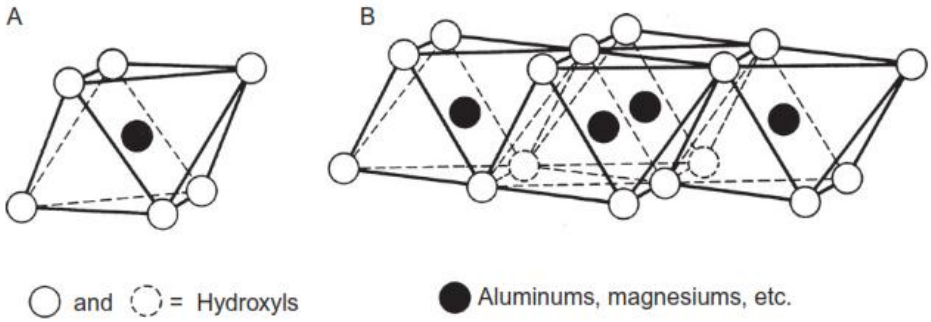

Figure 2.2 Schematic of (a) an octahedron unit and (b) an octahedral sheet. (Adapted from ref. [87])

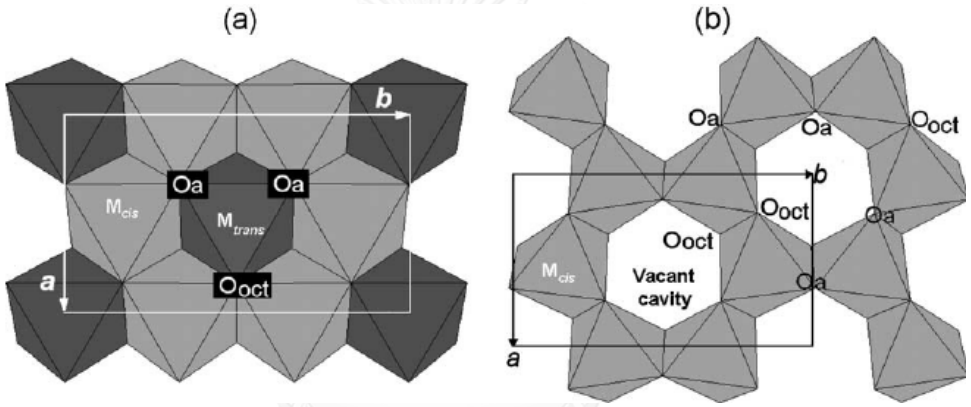

Figure 2.3 Schematic of (a) a trioctahedral sheet and (b) a dioctahedral sheet. (Adapted from ref. [86])

There are two types of layer structure formed by T sheets and O sheets: the 1:1 layer structure (by a repetition of one tetrahedral and one octahedral sheet) and the 2:1 layer structure (by a repetition of two tetrahedral enclosing one octahedral sheet) [86] as shown in Figure 2.4.

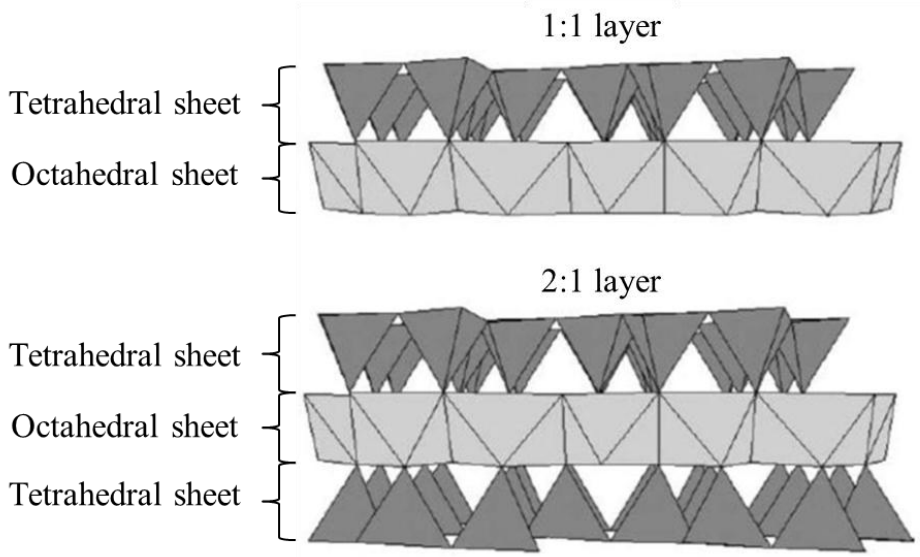

Figure 2.4 The clay mineral structure of 1:1 and 2:1 layer types. (adapted from Brigatti et al . [85])

2.1.1.1 The 1:1 phyllosilicates (T-O)

All of clay minerals of this type have no layer charge. The group of dioctahedral 1:1 minerals with the general composition of $Al_2Si_2O_5(OH)_4$ is called the kaolin group (e.g., kaolinite, dickite, nacrite, halloysite and hisingerite.) For trioctahedral 1:1 minerals, the serpentine group, the general composition is $Mg_3Si_2O_5(OH)_4$ (e.g., lizardite, antigorite, and chrysolite.)

2.1.1.2 The 2:1 phyllosilicates (T-O-T)

In this case, they can be classified into 3 groups, 2:1 phyllosilicates with no interlayer, with cation interlayer, and with octahedral sheet interlayer.

2.1.1.2.1 The 2:1 phyllosilicates with no interlayer

This group has no charge on the layers. The layers hold together by van der Waals interactions. The group consists of pyrophyllite $Al_2Si_4O_{10}(OH)_2$ (dioctahedral) and talc $(Mg,Fe)_3Si_4O_{10}(OH)_2$ (trioctahedral).

2.1.1.2.2 The 2:1 phyllosilicates with cation interlayer

Clay minerals in this type is called mica group. The layers of this type show net negative charge. The values of the negative charge per half-unit-cell are up to the amount of heterovalent substitution in the octahedral and tetrahedral sites. The members of this group are present as follow.

Muscovite: The ideal composition of Muscovite is $KAl_2(Si_3Al)O_{10}(OH)_2$.

Illite: The general composition of illite is similar to Muscovite. The difference is that, for illite, the Al^{3+} in octahedral sites are partially substituted by Mg^{2+} or Fe^{2+} and the Si^{4+} in tetrahedral sites are partially substituted by Al^{3+}. The charge of this group is between -0.6 and -0.9.

Smectites: In this case, tetravalent Si^{4+} cation in tetrahedral sites is partially substituted by trivalent cations of Al^{3+} or Fe^{3+} which results to an excess of negative charge on the tetrahedral sheet. For octahedral sites, the partially substitution of trivalent by divalent cations in dioctahedral smectite creates an excess of negative charge, whereas the partially substitution of divalent by trivalent cations in trioctahedral smectite creates an excess of positive charge on the layer. The important species of dioctahedral smectites are:

Montmorillonite $(M_y \cdot nH_2O)(Al_{2-y}Mg_y)Si_4O_{10}(OH)_2$

Beidellite $(M_x \cdot nH_2O)Al_2(Si_{4-x}Al_x)O_{10}(OH)_2$

Nontronite $(M_x \cdot nH_2O)Fe_2(Si_{4-x}Al_x)O_{10}(OH)_2$

Volkonskoite $(M_x \cdot nH_2O)Cr_2(Si_{4-x}Al_x)O_{10}(OH)_2$

The most species of trioctahedral smectite are:

Hectorite $(M_y \cdot nH_2O)(Mg_{3-y}Li_y)Si_4O_{10}(OH)_2$

Saponite $(M_x \cdot nH_2O)Mg_3(Si_{4-x}Al_x)O_{10}(OH)_2$

Sauconite $(M_x \cdot nH_2O)Zn_3(Si_{4-x}Al_x)O_{10}(OH)_2$

, where M is a monovalent cation, x is the amount of cations substituted in tetrahedral sites and y is the amount of cations substituted in octahedral sites.

Vermiculite is quite similar to trioctahedral smectite. The difference is that vermiculite has larger negative layer charge which due to more substitution of Al^{3+} for Si^{4+} in tetrahedral sites.

2.1.1.2.3 The 2:1 phyllosilicates with octahedral sheet interlayer

The clay mineral in this type is called chlorite group. The structure of this type is described as the stacking of the negatively charged 2:1 layers with the insertion of the positively charged octahedral sheet in interlayer. The octahedral sites can be occupied by Mg^{2+},Al^{3+}, Fe^{2+}, Fe^{3+}, Cr^{3+}, Mn^{3+}, Ni^{2+}, V^{3+}, Cu^{2+}, Zn^{2+}, and Li^{+} while the tetrahedral sites are occupied by Si^{4+} and Al^{3+}. However, Si^{4+} can occasionally be substituted by Fe^{3+}, Zn^{2+}, Be^{2+}, or B^{3+}. Some of trioctahedral chlorites are given below:

Clinochlore	$(Mg_5Al)(Si_3Al)O_{10}(OH)_8$
Chamosite	$(Fe_5Al)(Si_3Al)O_{10}(OH)_8$
Pennantite	$(Mn_5Al)(Si_3Al)O_{10}(OH)_8$
Nimite	$(Ni_5Al)(Si_3Al)O_{10}(OH)_8$

The flow chart describing the building block of various types of clay minerals is illustrated in Figure 2.5.

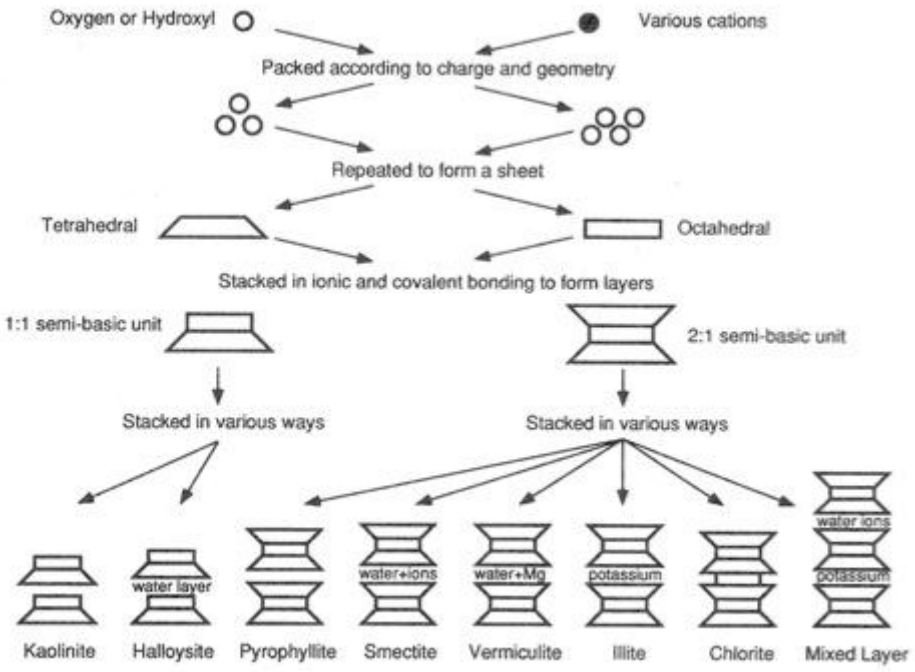

Figure 2.5 Flow chart demonstrates the formation of clay minerals [88].

2.1.2 Anionic clay

The layered double hydroxides (LDHs) were referred as anionic clays because of the similarity of the physical and chemical properties compared to clay minerals. The similar properties include the layered structure, wide chemical compositions, variable charge density, ion-exchange properties, reactivity in interlayer space, swelling in water, and rheological and colloidal properties. Unlike clay minerals, LDHs have a positively charge layers which make LDH exhibit anion-exchange properties [43].

The structure of LDHs is related to that of brucite [$Mg(OH)_2$] which is of the CdI_2 type [89]. Considering the brucite structure illustrated in Figure 2.6, each Mg^{2+} cation is surrounded by six OH^- anions to form an octahedral unit. Each octahedral unit links together by edge-sharing to form infinite layer and leaves the hydroxide anions sitting perpendicular to the plane of the layers. The three dimensional structure is created by the stacking of the layers on top of one another.

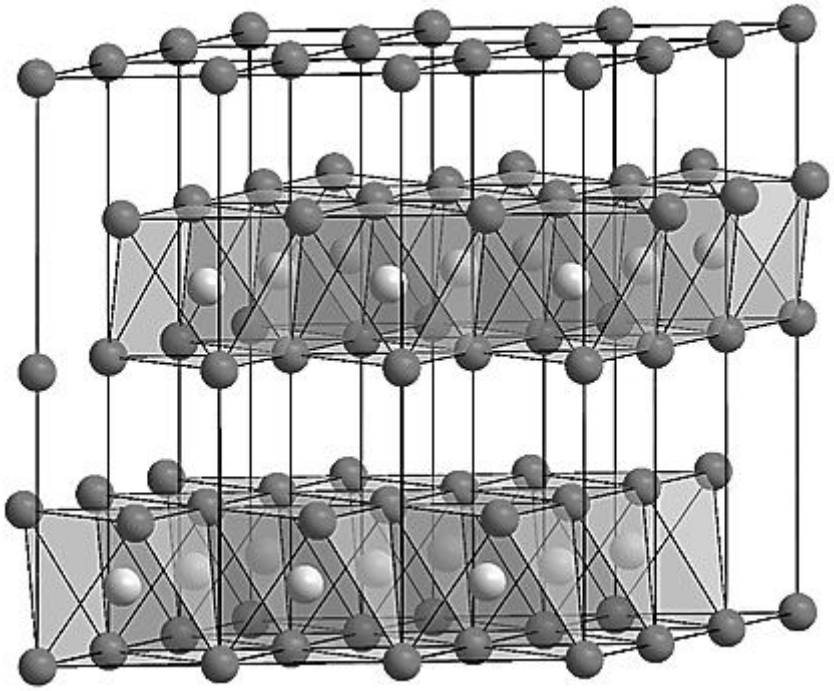

Figure 2.6 The structure of brucite [$Mg(OH)_2$]. Dark balls are hydroxide anions and white balls are magnesium ions. [90]

Unlike brucite, LDHs have a net positive charge on the layers. This charge is a result of the partial substitution of divalent Mg^{2+} cation by trivalent cations, such as Al^{3+} in case of hydrotalcite [43]. The positive charge is balanced by anions which intercalates in between the layers as shown in Figure 2.7. However not only Mg^{2+} cation that can occupied in octahedral hole, any divalent metal cations with the ionic radii lower than 0.06 nm also capable to occupy this octahedral hole [43]. Hence the general formulae of LDHs can be written as $[M^{II}_{1-x}M^{III}_{x}(OH)_2][X^{n-}_{x/n}]$ where M^{II} is the divalent metal cation, M^{III} is the trivalent metal cation, x is the amount of M^{III}, X is anion, and n is a charge of anion.

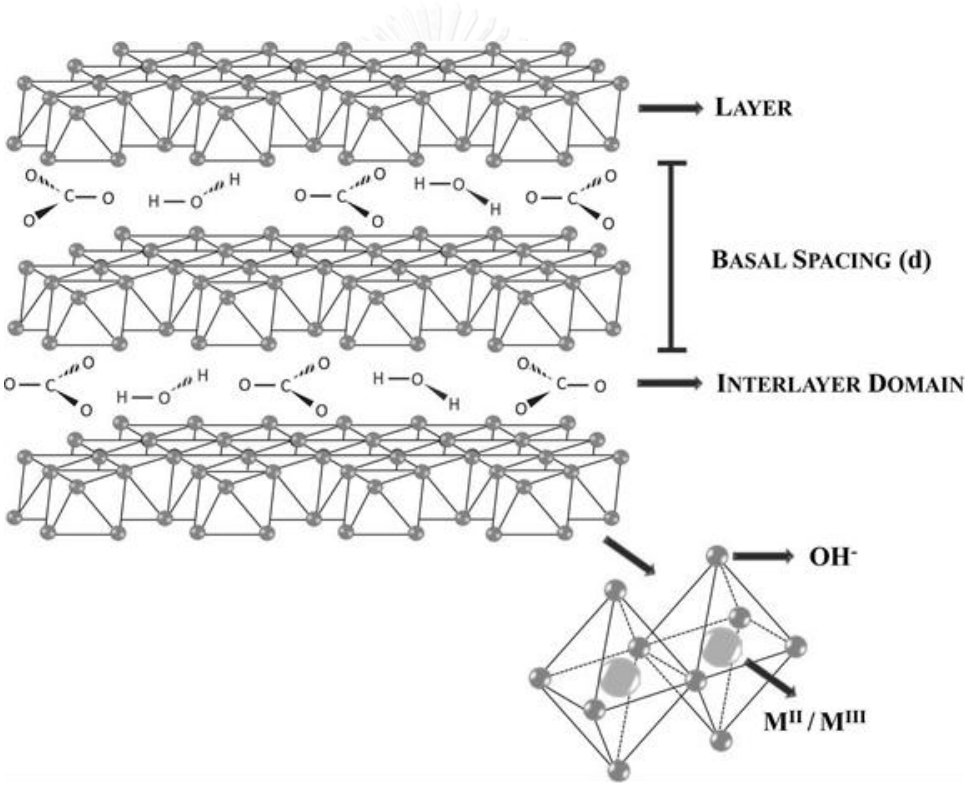

Figure 2.7 Schematic of LDH structure [91].

2.1.2.1 Structure of LDHs

There are many types of LDH structure depending on the stacking sequences of brucite-like layers. Giving that A, B and C are sites of brucite-like layers related by lattice translation, A is at (0, 0, 0), B is translated to (1/3, 2/3, 0), and C is translated to (2/3, 1/3, 0)]. And a, b, and c are the location of octahedral holes occupied by

metal cations related to A, B, and C. Thus the symbol AbC represents the brucite-like sheets at A and C sites and the cation at b sites. If the opposing OH groups of adjacent layers lie vertically above one another (say both in C sites), a trigonal prismatic arrangement is denoted by the symbol =, if the adjacent layers are different on different sites, the connection will denoted by ~. Therefore brucite can be denoted as ...AbC~AbC... H and R are denoted for a stacking sequence with hexagonal symmetry a rhombohedral symmetry, respectively. The possible polytypes of LHDs are listed in Table 2.2.

Table 2.2 The possible polytypes for all stacking sequences [89]

Stacking sequence	Symbol	Symmetry	Polytype characteristic
...AbC~AbC~AbC...	1H	Hexagonal	One-layer
...AbC=CbA=AbC...	$2H_1$	Hexagonal	Two-layer
...AbC~AcB~AbC...	$2H_2$	Hexagonal	
...AbC~BcA=AbC...	$2H_3$	Hexagonal	
...AbC~AcB~AcB~AbC...	$3H_1$	Hexagonal	Three-layer
...AbC~AcB~CaB~AbC...	$3H_2$	Hexagonal	
...AbC~AcB=BcA~AbC...	$3H_3$	Hexagonal	
...AbC~AbC=CbA=AbC...	$3H_4$	Hexagonal	
...AbC~AcB=BaC~AbC...	$3H_5$	Hexagonal	
...AbC~AcB~CbA=AbC...	$3H_6$	Hexagonal	
...AbC~AcA~BcA=AbC...	$3H_7$	Hexagonal	
...AbC=CaB=BcA=AbC...	$3R_1$	Rhombohedral	Three-layer
...AbC~BcA~CaB~AbC...	$3R_2$	Rhombohedral	

2.1.2.2 Natural occurrence LDHs

Hydrotalcite, $Mg_6Al_2(OH)_{16}[CO_3]^{\bullet}4H_2O$, is the longest-known natural occurrence mineral. It is a white hydrous mineral with a rhombohedral system [43]. Many

minerals belong to the hydrotalcite groups, for example, stichtite $Mg_6Cr_2(OH)_{16}[CO_3]\cdot 4H_2O$, pyroaurite $Mg_6Fe_2(OH)_{16}[CO_3]\cdot 4H_2O$, and zincowoodwardite $Zn_{1-x}Al_x(OH)_2[SO_4]_{x/2}\cdot nH_2O$. Variations such as the dominant divalent cations, (e.g. Mg, Ca, Mn, Fe, Ni, Cu and Zn), the dominant trivalent cations, (e.g. Al, Mn, Fe, Co and Ni), the M^{2+}/M^{3+} ratios, and the intercalated anions (e.g.CO_3^{2-}, SO_4^{2-}, Cl^-, OH^-, S^{2-} and $[Sb(OH)_6]^-$) [43, 92] are also found naturally.

2.1.2.3 Synthetic LDHs

A wide range of M^{2+}/M^{3+} LDHs was synthesized on both fixed and varied ratio. There is only one LDH produced from a monovalent cation are found, i.e., $LiAl_2(OH)_6X\cdot nH_2O$. Several reports reveal that tetravalent metal cations can be incorporated to LDHs [93-96]. Not only LDHs with binary component are synthesized, but LHDs with multicomponent can also be prepared.

The general formula of M^{2+}/M^{3+} LDHs is given as $[M^{II}_{1-x}M^{III}_x(OH)_2][X^{q-}_{x/2}\cdot nH_2O]$. The molar fraction, x, of M^{III} can be determines by $x = \sum(M^{III})/\sum_i(M_i)$.

2.1.2.4 Synthesis method of LDHs [42, 43, 97]

2.1.2.4.1 Coprecipitation

This is the simplest and most commonly used method. There are generally two types of coprecipitation conditions.

First condition is coprecipitation at low supersaturation. In this condition, three solutions are prepared; an aqueous solution of the desired interlayer anion, a mixed solution of divalent and trivalent metal salts at the selected ratio, and a solution of an alkali. A mixed salt solution and an alkali solution are simultaneously slowly added into a reactor containing an aqueous solution of the desired interlayer anion. An alkali solution is added at such a rate as to maintain the desired pH for coprecipitation of the two metallic salts. For the coprecipitation at high supersaturation, only two solutions are required; a mixed salt solution and an alkali solution.

Coprecipitation at high supersaturation generally gives rise to less crystalline materials compared to those with low supersaturation, due to the formation of a large number of crystallization nuclei. In order to increase the yields and crystallinity of the materials, a thermal treatment process is required after precipitation and then followed by an aging process conducted for a period ranging from a few hours to several days.

2.1.2.4.2 The urea method

In standard coprecipitation method, OH^- is act as a precipitating agent. In this method, a very weak Brønsted base is used instead. Urea is a highly soluble in water and its hydrolysis rate can be easily controlled by temperature, making it suitable to prepare a monodisperse particle.

2.1.2.4.3 Ion exchange method

If the coprecipitation method is inapplicable, the ion exchange method will be applied. For example, in the case that the divalent or trivalent metal cations or the anions involved are unstable in the alkaline solution, or when the direct reaction between the metal ions and the guest anions is more favorable. However, the LDHs with low affinity anions in the interlayer should be prepared before ion exchange process. The affinity of anions toward LDHs is concluded as the followings.

The order of affinity of LDH for monovalent anions:

$OH^- > F^- > Cl^- > Br^- > NO_3^- > I^-$

The order of affinity of LDH for divalent anions:

$CO_3^{2-} > C_{10}H_4N_2O_8S^{2-} > SO_4^{2-}$

In this method, the desired anions are exchanged with the low-affinity anions present in the interlayer spaces of the LDHs to produce specific anion-pillared LDHs. One should keep in mind that the guest anions should have higher affinity to LDHs than that in the interlayer spaces of the LDHs.

2.1.2.4.4 Reconstruction

This method involves calcination of LDHs containing a volatile anion in order to remove the interlayer water, interlayer volatile anions, and the hydroxyl groups. The result product is mixed metal oxides which can be regenerated to the layered structure when they are exposed to water and the desired inorganic or organic anions. To obtain a structure recovery property, it is important to control the temperature, rate, and duration for the calcination of LDHs.

2.2 Composites

A composite is a solid multiphase material made of more than one component. Composite materials can be considered as the mixing of two phases, a matrix and a dispersed phase or filler. A matrix is continuous and surrounds a dispersed phase [27, 98]. The properties of composite materials depend on the properties of each constituent phase, their relative amounts, and also particle size, particle distribution, and the orientation of a dispersed phase.

A nanocomposite is a solid multiphase material which at least one dimension of at least one component is in range 1 to 100 nm [27, 28, 32]. Their properties depend on the properties of each component, compositions, micro-structures, and interfacial interactions. Additionally, the properties are strongly influenced by the dimension and microstructure of dispersed phase [27]. When the particle size is less than a particular level, called 'the critical size', the changes in particle properties can be observed [32]. Moreover, if the dimension of particle reaches the nanometer scale, the interaction at an interface becomes largely improved, and greatly enhances the properties of materials. In polymer nanocomposites, the filler or dispersed phase has at least one dimension in the nanometer level. Its nanoscale dispersion within the polymer matrix leads to the largely interfacial contacts between the polymer and inorganic filler, resulting to the superior strength as compared with the bulk polymer.

There are three types of nanocomposite materials based on their matrix materials, ceramic nanocomposites, metal nanocomposites and polymer nanocomposites [32].

2.3 Polymer/clay composites

The polymer/clay composite is made with the combination of a polymer and clay. Because clay has the network-layer sheets in the nanometer scale, the structural strength of the composite is expected. The structure of polymer/clay composites can be divided into three types based on the degree of dispersion of polymer and clay [27, 29, 38, 99-101].

2.3.1 Conventional composite or microcomposite [27, 29, 101]

Microcomposites are the composites that the polymer does not reside into the interlayer of clay. The clay particles are dispersed in the polymer matrix as aggregates or particles. In this type, the d-spacing or d_{001} of the clay is the same [101]. The properties of these composites are the combination of each component without interfacial interactions [34]. The simplified structure of microcomposites is depicted in Figure 2.8 (a).

2.3.2 Intercalated nanocomposite [27, 29, 34, 38, 99-101]

Intercalated nanocomposites are obtained when polymer chains insert (intercalate) into the gallery of the clay, resulting in the increasing of d-spacing of the clay. The large amount of polymer may lead to very large expansion of clay gallery; however, the clay layers must remain stacked. The properties of the intercalated nanocomposites usually resemble those of ceramic materials [38, 99] with the special property of intercalated polymer. The structure of intercalated nanocomposites is depicted in Figure 2.8 (b).

2.3.3 Exfoliated nanocomposite [27, 29, 34, 38, 99-101]

When the polymer chains insert in between interlayer of the clay and separate clay into individual layer, the exfoliated or delaminated structure is obtained. In this structure, the stacking of clay layers is totally lost due to the layers is far apart from each other. Therefore the d_{001} cannot be determined by a conventional XRD. Normally, the exfoliated structure is obtained when the polymer causes the expansion more than 8-10 nm [27, 101]. The structure of exfoliated nanocomposites is depicted in Figure 2.8 (c).

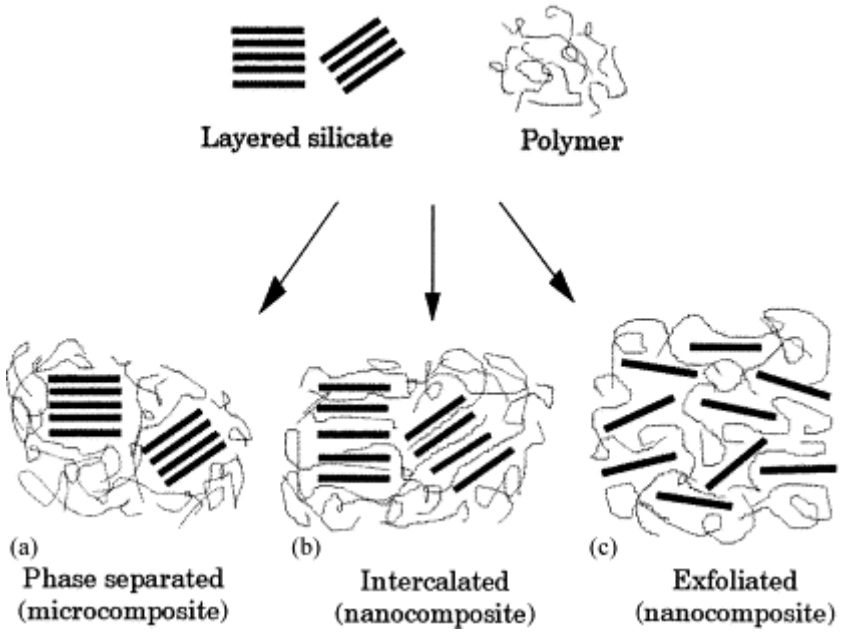

Figure 2.8 Schematic of various polymer/clay structural configurations. (adapted from ref. [34])

2.4 Preparation of polymer/clay composites

2.4.1 In situ template polymerization [27, 29, 34]

In this method, the inorganic host crystals are prepared in the solution containing polymer. The nucleation and growth of in organic host crystals are aided by the polymer and then the polymer is trapped inside the hosts as they grow. The advantage of this method is the well dispersion of the layered silicate in the polymer

matrix at nanometer scale. The drawback occurs when the high temperature of inorganic synthesis is required, resulting to the degradation of polymer.

2.4.2 Solution intercalation [27, 29, 34, 38]

For this technique, it is important to dissolve the polymer in a suitable solvent. Moreover, this solvent should be hydrophilic enough to disperse the clay layers to nearly single layer. When the polymer solution is mixed to the dispersed layered silicates, the polymer intercalates and displaces the solvent molecules or interlayer cations in the gallery of silicate. Upon the evaporation of solvent, the layers reassembly and sandwich the polymer to form an ordered multilayer structure, resulting to nanocomposite with intercalated structure as shown in Figure 2.9.

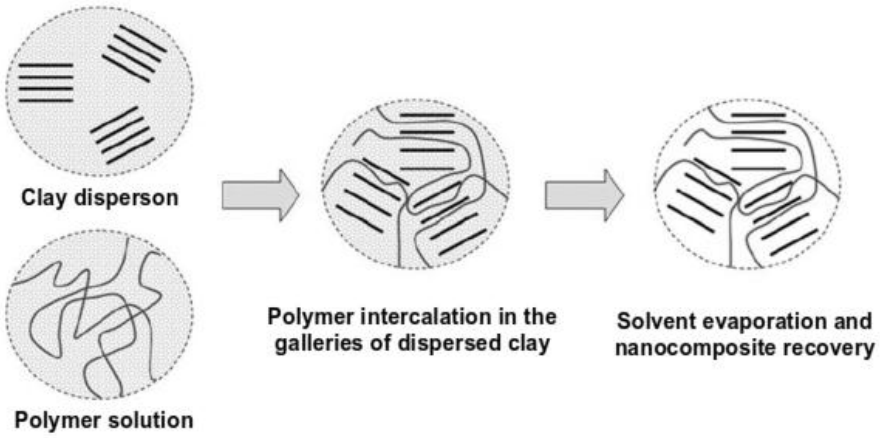

Figure 2.9 Schematic of the preparation of polymer/clay via solution intercalation method. (Adapted from ref. [29])

2.4.3 In situ intercalative polymerization [27, 29, 34, 38]

In this method, the polymer is synthesized in the solution containing the dispersed clay as shown in Figure 2.10. Firstly, clay is dispersed in the solution contain monomers. The monomer molecules intercalate into the interlayer of clay and then polymerized by the initiation of either heat or radiation, by the diffusion or

cationic exchange of a suitable initiator or catalyst into the interlayer before the swelling step by the monomer.

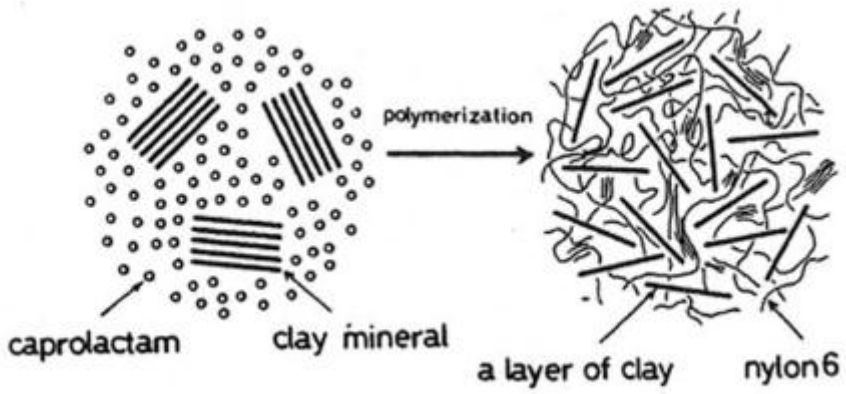

Figure 2.10 Schematic of the synthesis of Nylon-6/clay nanocomposite. (Adapted from ref. [29])

2.4.4 Melt intercalation [27, 29, 34, 38]

In this technique, the polymer is melted at high temperature (above the softening point of the polymer) and blended with clay under shear. Under these conditions and if the layer surfaces are sufficiently compatible with the chosen polymer, the polymer can crawl into the interlayer space and form either an intercalated or an exfoliated nanocomposite. The advantage of this technique is that the solvent is not required. However, the use of high temperature to produce a homogenous mixed product can lead to the degradation of polymer.

2.5 X-Ray Diffraction (XRD)

X-rays are electromagnetic radiation with the wavelength in the range of 0.01 to 10 nm. The working range for XRD is 0.05 – 0.25 nm, which is about the same degree of lattice d-spacing [102]. X-ray diffraction is the important characterization tools used in solid state chemistry and materials science. It has been used for two main approaches. The first approach is the fingerprint characterization. Because the characteristic X-ray powder pattern of each crystalline solid is unique; therefore, a

fingerprint for the identification of each crystalline solid is very effective. Another approach is to determine a crystalline structure, i.e., how the atoms pack together in the crystalline state and what the atomic distances and angles are, etc. The size and shape of the unit cell of the material also can be determined.

Bragg's law

Bragg diffraction was first proposed by William Lawrence Bragg and his father William Henry Bragg in 1913 [103]. They found that the crystals, at certain specific wavelengths and incident angles, produced intense peaks of reflected radiation. They explained this result by modeling the crystal as a set of discrete parallel planes separated by a constant parameter d. Bragg diffraction occurs when X-ray radiation, with a wavelength comparable to atomic spacings, is incident upon a crystalline sample, scattered by the atoms in the system, and undergo constructive interference in accordance to Bragg's law. The constructive interference (Figure 2.11) occurs when the difference between the path lengths of the two waves is equal to an integer multiple of the wavelength. If the difference between the path lengths of the two waves is not equal to an integer multiple of the wavelength, then the destructive interference occurs as shown in Figure 2.12.

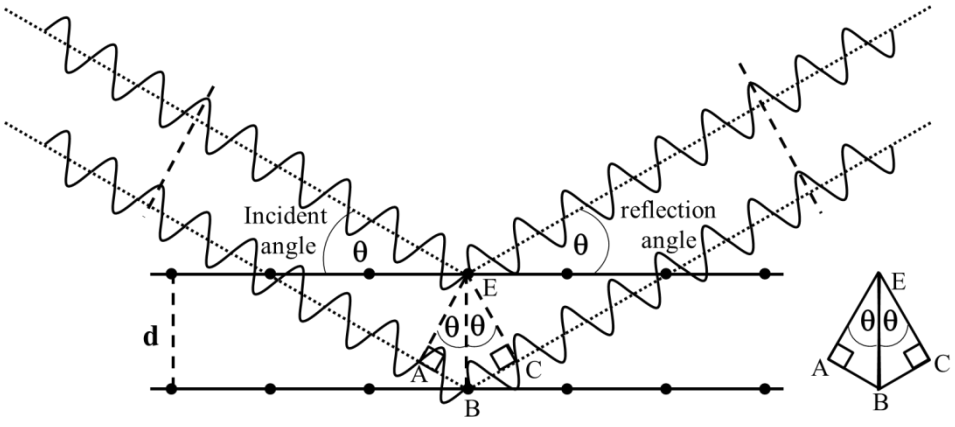

Figure 2.11 Schematic of the constructive interference of reflected waves (reflected waves in phase, i.e., maxima are superimposed).

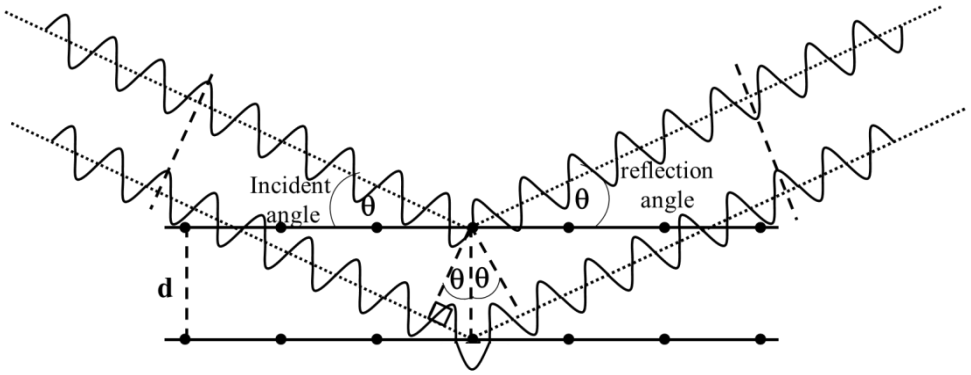

Figure 2.12 Schematic of the destructive interference of reflected waves (in the two reflected waves, maximum and minimum of the respective wave amplitude are superimposed).

2.6 N_2 adsorption-desorption isotherm

The surface of any material is the separating plane between a solid and its surroundings, liquid, gas or another solid. The surface area is an important factor in the behavior of a solid which affects, for example, dissolution rates of pharmaceuticals, the activity of an industrial catalyst, how fast cement hydrates, and adsorption capacity of air and water purifiers. There are six types of physical adsorption isotherms classified by the IUPAC [104-106] as shown in Figure 2.13.

Type I isotherm

The materials which give this type of isotherm are identified as microporous materials. The interaction between sample surface and adsorbate is relatively strong. Pores are typically microporous (pore diameters of less than 2 nm) with the exposed surface residing almost exclusively inside the microspores, which once filled with adsorbate, leave little or no external surface for further adsorption.

Type II isotherm

Most frequently, the nonporous powders or powders with macropores give this type of isotherm. Brunauer, Emmett, and Teller described this type as the

multilayer adsorption. Point B in Figure 2.13 is the inflection point which occurs near the completion of the first adsorbed monolayer. The interaction between sample surface and adsorbate is relatively strong.

Type III isotherm

This isotherm is indicative suggesting the presence of nonporous or macroporous surfaces which interact very weakly with adsorbate molecule.

Type IV isotherm

The materials which give this type of isotherm are classified as mesoporous materials which interact relatively strong with adsorbate molecule. The hysteresis loop is observed for this type. Similar to type II isotherm, the inflection point (at point B) typically occurs near completion of the first monolayer.

Type V isotherm

The type V isotherm is closed to the type IV isotherm. The difference is that, for the type V isotherm, the interaction between adsorbent-adsorbate is very weak. The materials giving this type of isotherm are purposed as mesoporous and microporous materials.

Type VI isotherm

This isotherm is the stepped adsorption isotherm. It comes from phase transition of the adsorbed molecular layer or adsorption on the different faces of crystalline solids. This type was attributed to nonporous surfaces.

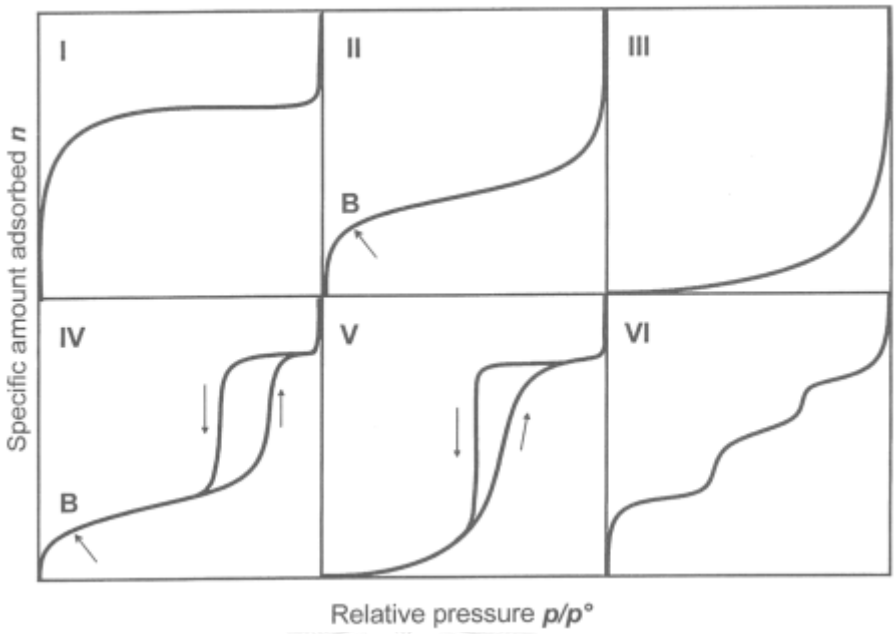

Figure 2.13 Diagrammatic representation of isotherm classification [107].

Pores of any materials were simply classified in term of pore widths (Table 2.3) as micropores (less than 2 nm), mesopores (2 and 50 nm), and macropores (larger than 50 nm).

Table 2.3 The IUPAC classification of pores [104-106].

Types of pores	Pores width (w)
Macropores	w > 50 nm
Mesopores	2 nm > w > 50 nm
Micropores	w < 2 nm

BET surface area

In 1938, Brunauer, Emmett and Teller developed the Brunauer-Emmett-Teller (BET) theory which was an extension of the Langmuir theory [108]. It is the most common method for determining the surface area of powders and porous materials. IUPAC was also recommended the Brunauer-Emmett-Teller (BET) method to derive

the surface area from physisorption isotherm data [109]. The BET equation is expressed by:

$$P/[n(P_0-P)] = 1/(n_mC) + [(C-1)/(n_mC)][P/P_0] \quad (2.\ 1)$$

where n is the amount adsorbed at the relative pressure P/P_0, n_m is the monolayer capacity and C is a constant, which is dependent on the isotherm shape.

If the $P/[n(P_0-P)]$ is plotted against P/P_0, a linear relation is obtained and the value of n_m can be calculated. The surface area, A(BET) is calculated from equation below.

$$A(BET) = n_m \times L \times a_m \quad (2.\ 2)$$

where L is the Avogadro constant and a_m is a molecular cross-section area.

2.7 Adsorption kinetics

2.7.1 Pseudo first-order model [110-112]

In 1898, Lagergren suggested a pseudo-first-order rate equation to describe the kinetics of liquid-solid phase adsorption which can be written as (based on the adsorption capacity):

$$dQ_t/dt = k_1(Q_e-Q_t) \quad (2.\ 3)$$

where Q_e and Q_t (mg/g) are the adsorption capacities at equilibrium and at time t, respectively, and k_1 is the pseudo first-order kinetic rate constant. Integrating the equation with applying initial conditions (t = 0 to t = t and Q_t = 0 to Q_t = Q_t), the equation above becomes

$$\log (Q_e - Q_t) = \log (Q_e) - k_1 \times t/2.303 \quad (2.\ 4)$$

This equation can be rewritten as nonlinear form of

$$Q_t = Q_t[1-\exp(-k_1t)] \quad (2.\ 5)$$

The values of Q_e and k_1 can be determined from slope and intercept, respectively, of the plot of $\log(Q_e- Q_t)$ versus t.

2.7.2 Pseudo second-order model [113]

In 1999, Ho and McKay [113] suggested a pseudo-second-order rate equation in which base on the assumption that the rate-limiting step may be chemisorption

involving valency forces through sharing or exchange of electrons between sorbent and sorbate. It can be expressed as:

$$dQ_t/dt = k_2(Q_e-Q_t)^2 \quad (2.\ 6)$$

where Q_e and Q_t (mg/g) are the adsorption capacities at equilibrium and at time t, respectively, and k_2 is the pseudo second-order kinetic rate constant. Integrating the equation with applying initial conditions (t = 0 to t = t and Q_t = 0 to Q_t = Q_t), the equation above becomes

$$1/(Q_e-Q_t) = t/Q_e + k_2t \quad (2.\ 7)$$

This equation can be rewritten as:

$$t/Q_t = t/Q_e + 1/(k_2Q_e^2) \quad (2.\ 8)$$

The values of Q_e and k_2 can be determined from slope and intercept, respectively, of the plot of t/Q_t versus t.

2.8 Adsorption isotherm

2.8.1 Langmuir isotherm [114-117]

The Langmuir isotherm is based on the following assumptions:

a. All surface sites have the same adsorption energy for the adsorbate. The surface site is defined as the area on the sample where one molecule can adsorb onto.

b. Adsorption of solvent at one site occurs independently of adsorption at neighboring sites.

c. Activity of adsorbate is directly proportional to its concentration.

d. Adsorbates form a monolayer.

e. Each active site can be occupied only by one particle.

The Langmuir isotherm models describe a monolayer adsorption of sorbate onto the sorbent surface with homogeneous nature [114, 117]. The chemical reaction for monolayer adsorption can be written as:

$$A + S \rightleftharpoons AS \quad (2.\ 9)$$

where AS is a solute molecule bound to a surface site on S. The equilibrium constant (K_{ads}) for this reaction is represented as:

K_{ads} = [AS]/[A][S] (2. 10)

where [A] (mol/L) is the concentration of A, [AS] and [S] are two-dimentional analogs of concentration (mol/cm^2). If the fraction of the adsorption sites is represented as the surface coverage (θ), then term [AS]/[S] can be rewritten as:

[AS]/[S] = θ/(1-θ) (2. 11)

If [A] is expressed as C, the equilibrium constant can be rewritten as:

K_{ads} = θ/[C(1-θ)] (2. 12)

Rearranging the above equation, the Langmuir adsorption isotherm is obtained as:

θ = $K_{ads}C/(1+K_{ads}C)$ (2. 13)

The surface coverage (θ) can be expressed as Q_e/Q_m, then the linear form of Langmuir equation can be written as:

$C_{eq}/Q_e = C_{eq}/Q_m + 1/(K_L \times Q_m)$ (2. 14)

where C_{eq} (mg/L) is the equilibrium concentration, Q_e and Q_m (mg/g) are the equilibrium and maximum adsorption capacities, respectively, K_L is the Langmuir adsorption constant. Q_m and K_L values are calculated from the slope and intercept of the plot where C_{eq}/Q_e *versus* C_{eq} using equation 2.17.

The essential characteristics of Langmuir isotherm called separation factor or equilibrium parameter (R_L) can be expressed in terms of dimensionless constant which defined by [114, 115],

$R_L = 1/(1 + K_L C_0)$ (2. 15)

were K_L is the Langmuir adsorption constant and C_0 is the highest initial As(V) concentration (mg/L).

The R_L value indicates the shape and feasibility of the isotherm. R_L = 0 represents the irreversible adsorption process, 0 < R_L < 1 represents the favorable adsorption process, and R_L > 1 represents the unfavorable adsorption process [114-116].

2.8.2 Frudlich isotherm [114-119]

The assumption of Freundlich isotherm model is based on the sorbates adsorbed onto the heterogeneous surface of a sorbent [114, 115, 117]. It can be used for non-ideal sorption and is expressed by the following equation:

$$Q_e = K_F C_{eq}^{1/n} \quad (2.16)$$

where Q_e is the equilibrium adsorption capacity, C_{eq} is the equilibrium concentration, K_F is the Freundlich constant indicated the adsorption capacity, and n is the indicator showing the favorability of adsorption. The linear form of Freundlich equation is:

$$\log (Q_e) = \log (K_F) + (1/n) \log (C_{eq}) \quad (2.17)$$

The values of K_F and n values are calculated from the intercept and slope of the plot where log (Q_e) *versus* log (C_{eq}) using equation 2.20. The value of n larger than 1 indicates the favorable adsorption condition [115, 116, 119].

CHAPTER 3

EXPERIMENTAL

3.1 Chemicals

All chemicals listed below were used as-receive.

3.1.1 3-acrylamidopropyl)trimethylammonium chloride (75%wt in water, Aldrich Chemical Company, Inc. Milwaukee, WI)

3.1.2 [2-(acryloyloxy)ethyl]trimethylammonium chloride (80 %wt in water, Aldrich Chemical Company, Inc. Milwaukee, WI)

3.1.3 *N,N'*-methylenebisacrylamide (99.5%, Aldrich Chemical Company, Inc. (Milwaukee, WI)

3.1.4 Ammonium persulfate (Univar reagent grade, Ajax Finechem Pty. Ltd.)

3.1.5 *N,N,N',N'*-tetramethylethylenediamine (Purity 99%, Sigma-Aldrich, Inc.)

3.1.6 $Na_2HAsO_4 \cdot 7H_2O$ (Purity ≥98.0%, Sigma)

3.1.7 $Mg(NO_3)_2 \cdot 6H_2O$ (AR/ACS, 99.0-102.0%, Loba Chemie Pvt. Ltd.)

3.1.8 $Fe(NO_3)_3 \cdot 9H_2O$ (Univar reagent grade, 98.0-101.0% , Ajax Finechem Pty. Ltd.)

3.1.9 $FeSO_4 \cdot 7H_2O$ (AR, 99.0-104.5%, Loba Chemie Pvt. Ltd.)

3.1.10 $ZrOCl_2 \cdot 8H_2O$ (RPE for analysis reagent grade, Carlo Erba reagent Ltd.)

3.1.11 NaOH (Emsure ISO reagent grade, Merck KGaA)

3.1.12 Na_2CO_3 (Baker analyzed reagent grade, J. T. Baker)

3.1.13 NaCl (RPE for analysis reagent grade, Carlo Erba reagent Ltd.)

3.1.14 Na_2SO_4 (AR, Fisher Scientific)

3.1.15 NaH_2PO_4 (ACS, 99.0-102,0%, Merck KGaA)

3.1.16 $NaNO_3$ (Purity >99.0%, Fluka Chemical Corp.)

3.1.17 Bentonite (Cernic International Co. Ltd.)

3.2 Preparation of Na-bentonite

The raw bentonite was purified by dispersing 30 g bentonite in 1000 mL DI water. The suspension was stirred for 3 h and then centrifuged at 4000 rpm for 10

min. The supernatant was dried at 100°C in order to obtain the sediments as purified bentonite. The 20 g of purified bentonite powder was dispersed in 1000 mL of 5 M NaOH or NaCl. The suspension was stirred for 24 h and then centrifuged at 4000 rpm for 5 min. This ion-exchange process using NaOH or NaCl was repeated 3 times to ensure the Na-ion exchange. Hydroxides/chlorides and excess Na^+ ions were removed using dialysis membrane (Seamless Cellulose Tubing, small size 30, Wako Chemicals USA). The final product was dried at 100°C. The cation-exchanged capacity (CEC) was determined by the adsorption of a copper ethylenediamine complex [120]. The CEC of Na-bentonite in this work was 1.15 meq/g. The reported CEC of montmorillonite is between 0.80-1.50 meq/g [121].

3.3 Synthesis of polymer/bentonite nanocomposites via solution intercalation method

3.3.1 Preparation of preformed polymer solution

Poly(3-acrylamidopropyl)trimethylammonium chloride (pAPTMA-Cl) was synthesized via a free radical polymerization [49]. The starting materials of polymer, including a monomer APTMA-Cl (7.5-22.5 %w/v), a cross-linker MBA (0-5% by mole of APTMA-Cl monomer) and a co-initiator TEMED (1 % by mole of APTMA-Cl monomer) and DI water, were stirred in aqueous solution for 5 min. The solution was added to cylinder tube and bubbled with nitrogen gas for 5 min before adding an initiator APS (0-5 % by mole of APTMA-Cl monomer). After adding APS, the polymerization was aged for 1 h prior to the next step.

Poly([2-(acryloyloxy)ethyl]trimethylammonium chloride) (pAETMA-Cl) was also prepared in the similar fashion with poly(3-acrylamidopropyl)trimethylammonium chloride.

In order to compare the properties of nanocomposites and the bulk polymers, the bulk pAPTMA-Cl and pAETMA-Cl were synthesized via the same method with 30 %w/v of APTMA-Cl or AETMA-Cl monomer, MBA concentration of 1% by mole of APTMA-Cl monomer and TEMED concentration of 1 % by mole of APTMA-Cl monomer.

3.3.2 Preparation of polymer-bentonite nanocomposites

The pAPTMA/bentonite nanocomposites and pAETMA/bentonite nanocomposites were synthesized via a solution intercalation method. Firstly, Na-bentonite was dispersed into DI water and then stirred overnight before used. The Na-bentonite suspension and the as-prepared polymer solution were added to a conical tube and then stirred for 5 h. The precipitates were collected by centrifugation at 3000 rpm for 5 min and dried at 60°C.

The nanocomposites were denoted as *v*M*x*C*y*A*z*B, when *v* is the monomer concentration (7.5-22.5 %w/v), *x* is the percentage of MBA cross-linker (0-5 %mole), *y* is the percentage of APS initiator (0-5%mole), and *z* is the percentage of bentonite (5-70 %wt). For example, 15M1C2A30B is the pAPTMA/bentonite nanocomposite or pAETMA/bentonite nanocomposite, prepared from the monomer concentration of 15 %w/v, MBA cross-linker of 1 %mole, APS initiator of 2 %mole, and bentonite of 30 %wt.

3.4 Synthesis of polymer/bentonite nanocomposites via *in situ* intercalative polymerization method

In the synthesis of the polymer/bentonite composites via *in-situ* intercalative polymerization method, all precursors (APTMA-Cl monomer or AETMA-Cl, MBA cross-linker, TEMED and Na-bentonite) were mixed together and stirred overnight before adding APS initiator.

In order to study the effect of MBA cross-linker concentration, the concentration of MBA cross-linker was varied from 0 % to 5 % mole, while the weight ratio of Na-bentonite and monomer was fixed at 10:90 and 7.25:92.5 for APTMA-Cl and AETMA-Cl, respectively, the molar ratio of TEMED and APS over the APTMA-Cl monomer or AETMA-Cl were fixed at 1:100 and 0.5:100, respectively.

The effect of APS initiator concentration was studied by varying the molar ratio of APS initiator concentration over APTMA-Cl or AETMA-Cl monomer (0.5-5 %mole), while the weight ratio of Na-bentonite and monomer was fixed at 10:90 and 7.25:92.5 for APTMA-Cl and AETMA-Cl, respectively, the molar ratio of TEMED and

MBA over the APTMA-Cl or AETMA-Cl monomer was fixed at 1:100 and 3:100, respectively.

In order to study the effect of weight ratio of polymer and Na-bentonite, the concentration of Na-bentonite was varied from 5 % to 70 % wt while the molar ratio of MBA, TEMED and APS over the APTMA-Cl monomer or AETMA-Cl was fixed at 1:100, 1:100 and 0.5:100, respectively.

The nanocomposites were denoted as *x*C*y*A*z*B, when *x* is the percentage of MBA cross-linker, *y* is the percentage of APS initiator, and *z* is the weight ratio of bentonite and polymer. For example, 15M1C30B is the pAPTMA/bentonite nanocomposite or pAETMA/bentonite nanocomposite, prepared from the monomer concentration of 15 %w/v, MBA cross-linker of 1 %mole and bentonite of 30 %wt.

3.5 Synthesis of magnetic/LDH composite via coprecipitation method

3.5.1 Preparation of Fe_3O_4

The synthesis of Fe_3O_4 was modified from the method described in the literature [122]. A mixed-metal solution was prepared by dissolving 7.6340 g of $Fe(NO_3)_3 \cdot 9H_2O$ and 3.0020 g of $FeSO_4 \cdot 7H_2O$ in 100 mL deionized water. Concentrated ammonia (50 mL) was added to the mixed solution under continuous stirring. The pH of the solution was adjusted to 9 by adding concentrated ammonia. The solution was stirred for another 30 min. The black solid was separated using a magnet and washed three times with deionized water and twice with ethanol. Finally, the black solid was dried under vacuum at 60 $^{\circ}$C for 24 h. The product was ground and sieved through a 75 μm aperture before use.

3.5.2 Preparation of the LDH

The LDH was prepared via a coprecipitation method, modified from that described in the literature [123]. Mg-Fe-Zr LDH ($Mg_{0.66}Fe_{0.08}Zr_{0.25}(OH)_2(CO_3)_{0.28} \cdot nH_2O$) was prepared by mixing the metal precursors in a stoichiometric ratio. $Mg(NO_3)_2 \cdot 6H_2O$ (3.2051 g), $Fe(NO_3)_3 \cdot 9H_2O$ (0.6121 g) and $ZrOCl_2 \cdot 8H_2O$ (1.5259 g) were dissolved in 25 mL of deionized water. The solution was then added to the base solution containing

NaOH (1.65 g) and Na_2CO_3 (1.3249 g) in 25 mL of deionized water, which led to the formation of white precipitates. The precipitates were separated using centrifugation and washed several times with deionized water until the supernatant reached pH 7. Finally, the LDH precipitates were dried at 60 °C for two days. The calcined LDH was obtained from calcination at 450 °C for 5 h. The calcination product was named c-LDH.

3.5.3 Preparation of the Mg-Fe-Zr LDH/Fe_3O_4 composite (m-LDH)

The Mg-Fe-Zr LDH/Fe_3O_4 composite was synthesized by the precipitation of the LDH in the presence of the preformed Fe_3O_4 particles. At first, the Fe_3O_4 suspension was prepared by sonicating the mixture containing Fe_3O_4 (0.1625 g) in 12.5 mL of deionized water for 5 min. The following steps proceeded as mentioned above for the preparation of the LDH, except that the mixed-metal and base solutions were simultaneously added to the suspension of Fe_3O_4 with continuous stirring. As before, the precipitates were separated using centrifugation and washed several times with deionized water until the supernatant reached pH 7. Finally, the magnetic-LDH (m-LDH) precipitates were dried at 60 °C for two days. The calcination product of m-LDH (cm-LDH) was obtained by calcination at 450 °C for 5 h.

3.6 Characterization

Materials structures were characterized by XRD using a Rigaku, Dmax-2200 Ultima$^+$ diffractometer equipped with a monochromator and a Cu Kα radiation source generated at 40 kV and 30 mA. The scattering, divergent and receiving slits were set at 1°, 1° and 0.3 mm, respectively. The surface area of each sample was measured by N_2 adsorption-desorption using a BEL Japan BELSORP-mini 28SP instrument. The morphology and spreading of the metals in the composite particles were monitored by SEM-EDX using a JSM-5800 LV scanning electron microscopy (Oxford Instrument Link ISIS series 300). The magnetic hysteresis loops were recorded using a vibrating sample magnetometer (VSM, LakeShore 7404). Transmission electron microscopy (TEM) images were carried out using a Philips TECNAI 20 electron

microscope. The organic contents of nanocomposites were determined by thermogravimetric analysis under nitrogen atmosphere using Perkin-Elmer Pyris 1 TGA with a heating rate of 10°C/min. The FTIR spectra were recorded as KBr pellets with a Thermo Scientific Nicolet 6700 FTIR spectrophotometer.

3.7 Arsenate adsorptions studies of polymer/bentonite nanocomposites

The 50 mg/L stock solution of As(V) was prepared by dissolving 0.1041 g of $Na_2HAsO_4{\cdot}7H_2O$ (Purity ≥98.0%, Sigma) in 500 mL of MilliQ water. The pH of As(V) solutions was adjusted by 0.01 M, 0.1 M, and 1.0 M HNO_3 and NaOH.

The As(V) adsorption experiments were conducted in batch processes at room temperature. The sample (15 mg) was weighed into 50 mL polypropylene bottle with a screw-top cover. The As(V) solution (10 mL) was then added. The bottle was shaken using an overhead shaker with a shaking rate of 30 rpm. The suspension was centrifuged and filtered through a 0.45 μm syringe filter. The As(V) concentration was determined by ICP-OES model iCAP 6500 series (Thermo Fisher scientific). The As(V) adsorption amount was calculated by :

$$Q_t = [V(C_0 - C_t)]/m \qquad (3.\ 1)$$

where Q_t (mg/g) is the As(V) adsorption capacity, C_0 and C_t (mg/L) are the initial As(V) concentration and the As(V) concentration at time t, respectively. V (L) is the volume of the As(V) solution and m (g) is the mass of the sorbent.

3.7.1 Effect of sorbent dosage

Various amounts of a sorbent (15, 30, 45 and 60 mg) were suspended separately in 10 mL of 50 mg/L As(V) stock solution. The mixtures were shaken at 30 rpm for 6 h.

3.7.2 Effect of contact time

The sorbents (30 mg) were suspended in 10 mL of 50 mg/L As(V) stock solution. The mixtures were shaken at different time intervals (5, 10, 15, 20, 25 and 30 min.) at 30 rpm.

3.7.3 Effect of pH of solution on As(V) adsorption

The 50 mg/L As(V) stock solutions with different pH (2, 3, 5, 7, 9 and 11) were prepared and adjusted using 0.01, 0.1 and 1.0 M HNO_3 or NaOH. The samples (30 mg) were suspended in 10 mL of each solution and the mixtures were shaken at 30 rpm for 6 h.

3.7.4 Effect of initial As(V) concentration

Different As(V) concentrations (10, 20, 30, 40, 50, 60 and 70 mg/L) were prepared and the pH was adjusted to 9 using 0.01, 0.1 and 1.0 M HNO_3 or NaOH. The samples (30 mg) were suspended in 10 mL of each solution and then shaken at 30 rpm for 6 h.

3.7.5 Effect of interference anions

Various types of sodium salts (NaCl, $NaNO_3$, Na_2SO_4, NaH_2PO_4 and Na_2CO_3) were dissolved separately in 50 mL of 50 mg/L As(V) stock solution to obtain the competing anion/As(V) molar ratio of 0.2, 1, 5, 10 and 50. The pH of each solution was adjusted to 9 using 0.01, 0.1 and 1.0 M HNO_3 or NaOH. The samples (30 mg) were suspended in 10 mL of each solution and the mixtures were shaken at 30 rpm for 24 h.

3.8 Arsenate adsorption studies of magnetic LDH composites

A 200 mg/L stock solution of As(V) was prepared by dissolving 0.4165 g of $Na_2HAsO_4{\cdot}7H_2O$ (purity ≥98.0%, Sigma) in 500 mL of Milli-Q water. The pH of the As(V) solution was adjusted by 0.01, 0.1 and 1.0 M HNO_3 and NaOH.

The As(V) adsorption was measured using batch experiments. The sorbent samples of 10 g were weighed into 50 mL polypropylene bottles with screw-top covers. As(V) solutions of 10 mL were then added. The suspensions were shaken using an overhead shaker with a shaking rate of 30 rpm. After the adsorption process, the supernatant was separated from the adsorbent using an external magnetic field. The supernatant was then filtered through a 0.45 μm syringe filter. The As(V)

concentration was determined by ICP-OES, model iCAP6500 series (Thermo Fisher scientific).

The As(V) adsorption capacity was calculated by:

$$Q_t = [V(C_0 - C_t)]/m \quad (3.\ 2)$$

where Q_t (mg/g) is the As(V) adsorption capacity, C_0 and C_t (mg/L) are the initial As(V) concentration and the As(V) concentration at time t, respectively. V (L) is the volume of the As(V) solution and m (g) is the mass of the sorbent.

3.8.1 Effect of contact time

The samples (10 mg) were suspended in 10 mL of 200 mg/L As(V) stock solution at pH 3. The mixtures were shaken at different time intervals (15, 30, 45, 60, 120, 180, 240, 300, 375, 480, 600, 720, 900, 1080, 1260, 1440, 2400, 2880, 3600, 4590, 5130, 5730, 6675 and 7200 min.) at the speed of 30 rpm.

3.8.2 Effect of pH of solution on As(V) adsorption

The effect of the initial pH on As(V) adsorption was examined by varying the pH of the 200 mg/L As(V) solution from 2 to 11 using 0.01, 0.1 and 1.0 M HNO_3 or NaOH. The samples (10 mg) were suspended in 10 mL of each solution and then the mixtures were shaken at 30 rpm for three days.

3.8.3 Effect of initial As(V) concentration

An experiment for adsorption isotherm was carried out by adding 10 mL of various As(V) concentrations (40, 120, 160, 200, 240, 280, 320 and 360 mg/L), at pH 3, into polypropylene bottles containing 10 mg of sorbents. The suspensions were shaken at 30 rpm for three days.

CHAPTER 4
RESULTS AND DISCUSSION

4.1 Synthesis of polymer/bentonite nanocomposites via solution intercalation method

The polymer/bentonite composites were prepared via the solution intercalation method, characterized by FTIR, XRD, and TGA and tested for their As(V) adsorption abilities. Two types of polymers, poly(3-acrylamidopropyl) trimethylammonium chloride) and poly([2-(acryloyloxy)ethyl]trimethylammonium chloride), were used in the synthesis. The concentration of monomer, MBA cross-linker, APS initiator, and Na-bentonite were varied in order to achieve the nanocomposites with the best adsorption performance.

4.1.1 Poly(3-acrylamidopropyl)trimethylammonium chloride)

4.1.1.1 Effect of monomer concentration

The concentration of APTMA-Cl monomer was varied from 7.5 %w/v to 22.5 %w/v while the molar ratio of MBA, TEMED and APS over the APTMA-Cl monomer was fixed at 1:100, 1:100 and 0.5:100, respectively. The as-synthesized polymer was then mixed with Na-bentonite by fixed the weight ratio of 70:30.

The FTIR spectra of Na-bentonite, the pAPTMA/bentonite composite (15M1C0.5A30B) and pAPTMA-Cl are shown in Figure 4.1. The characteristic peaks of Na-bentonite appear at 3627 cm^{-1} (X – OH, X = Al, Mg), 3441 cm^{-1}, 1644 cm^{-1} (H – O – H) and 1034 cm^{-1} ($Si(Al)O_4$) [36, 124, 125]. The FTIR spectrum of pAPTMA-Cl in Figure 4.1 (c) show the characteristic peaks at 3449 cm^{-1} (H – O – H), 2944 cm^{-1} (C_{sp3} – H), 1649 cm^{-1} (C = O amide) and 1480 cm^{-1} (C – N amide) [126]. It can be seen that the FTIR spectrum of composite (15M1C0.5A30B) contains both the characteristic peaks of Na-bentonite and pAPTMA-Cl. The results suggested that the composite was composed of both bentonite and pAPTMA-Cl. The FTIR spectra of the other composites show the same result with 15M1C0.5A30B. The characteristic absorption bands were summarized in Table 4.1.

Table 4.1 FTIR spectral assignment of Na-bentonite, 15M1C0.5A30B and pAPTMA-Cl

Band assignment	Na-bentonite (cm^{-1})	15M1C0.5A30B (cm^{-1})	pAPTMA-Cl (cm^{-1})
υ(X – O – H), X = Al, Mg[a]	3627	3618	-
υ(H – O – H)[a]	3441	3433	
δ(H – O – H)[a]	1644	1661	
υ(Si – O)[a]	1034	1037	-
δ(Al – Al – OH)[a]	914	913	-
δ(Al – Mg– OH)[a]	835	838	-
δ(Al – O – Si)[a]	521	517	-
δ(Si – O – Si)[a]	466	460	
υ(N – H) or υ(O – H)[b]		3433	3449
		3077	3077
υ(C – H)[b]	-	2959	2944
υ(C = O)[b]		1661	1649
δ(N – H)[b]	-	1552	1551
δ(N – H) of $RN^{+}(CH_3)_3$[b]	-	1491	1480
		1449	1443
υ(C – N)[b]		1247	1268

υ = stretching, δ = bending, [a]data from [36, 124, 125], [b]data from [70, 126, 127]

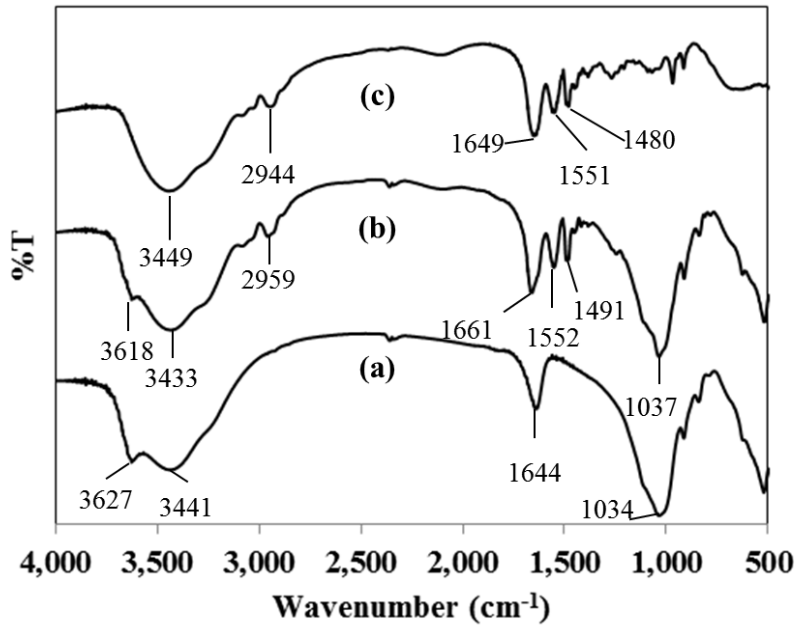

Figure 4.1 FTIR spectra of (a) Na-bentonite, (b) 15M1C0.5A30B and (c) pAPTMA-Cl.

All XRD patterns of the nanocomposites (Figure 4.2) shows the shift of (001) peaks of bentonite to larger d-spacings (2.13 $\pm$ 0.04 nm) as compared to the d-spacing of Na-bentonite (1.46 nm) while the d-spacing of (020) peak do not change. It can be explained that Na^+ ions were exchanged by the bigger cations, pAPTMA, resulting to the expansion of interlayer along (00*l*) direction. The result suggested that pAPTMA found by FTIR could indeed intercalate into the layers of bentonite and expanded the d-spacing of bentonite. The (001) d-spacings of all samples were summarized in Figure 4.3. The d-spacing become constant when the monomer concentration reached 7.5 %w/v.

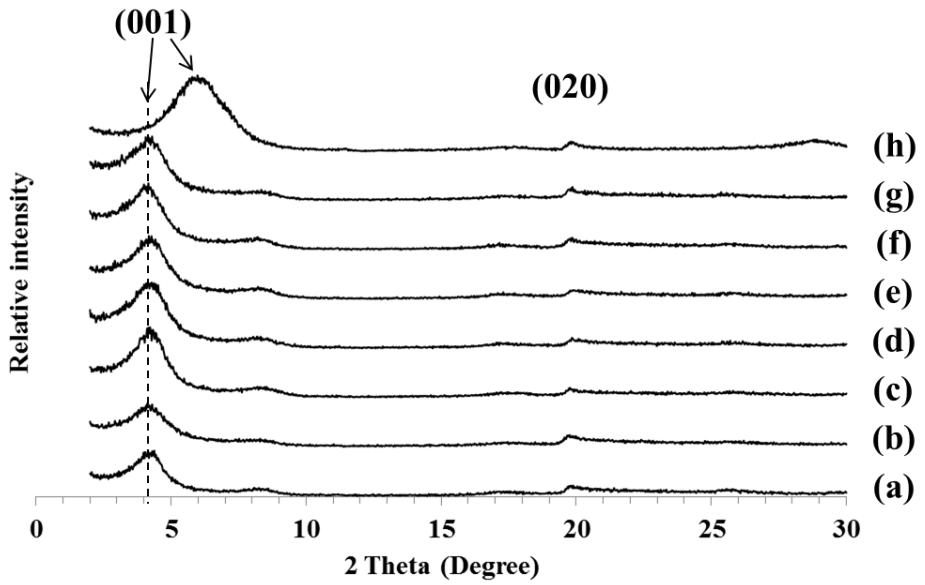

Figure 4.2 XRD patterns of pAPTMACl/bentonite composites of (a) 7.5M1C0.5A30B, (b) 10M1C0.5A30B, (c) 12.5M1C0.5A30B, (d) 15M1C0.5A30B, (e) 17.5M1C0.5A30B, (f) 20M1C0.5A30B, (g) 22.5M1C0.5A30B, and (h) Na-bentonite

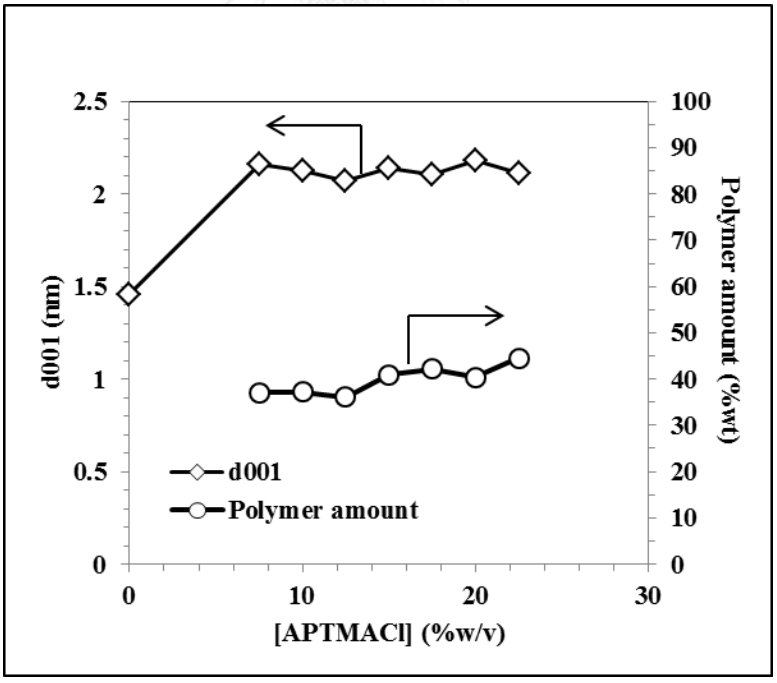

Figure 4.3 The d_{001} spacings and polymer amounts with varied monomer concentrations.

The amount of polymer in nanocomposites was estimated using TGA. As shown in Figure 4.4, Na-bentonite possesses the two-stepped [124, 128, 129] weight loss upon increasing temperature, (i) the loss of adsorbed and intercalated water between 50 – 180 °C (9.9%) and (ii) the degradation of clay layered structure starting from 500 °C (5.3%). For the bulk pAPTMA-Cl, the weight loss went through 3 steps [126], (i) the loss of the occluded water up to 100 °C (6.2%), (ii) the degradation of polymer involving the CO_2 and NH_3 evolution up to 300 °C (13.1%), and (iii) the decomposition of both main and side chains between 300-500 °C (76.4%). The characteristic weight loss of the nanocomposites of both materials could be predicted as the combination of the individual components. At the temperature up to 100 °C, the amount of water in the nanocomposites was significantly lower than its individual components. This could be explained that the pAPTMA polycation was trapped inside bentonite galleries instead of Na^+ ions, resulting to less amount of intercalated water [130]. The weight loss of water would count from the adsorbed water on the outer surface of the nanocomposite and the remaining intercalated water which could be evaporated at the temperature up to 100 °C and 180 °C, respectively. The characteristic loss of intercalated pAPTMA appeared as that of the bulk pAPTMA-Cl, except that the decomposition temperature would not be the sharp cut due to the confined space between bentonite layers trapping the decomposition products. Table 4.2 reviews the assignments of the weight loss in each temperature range. The calculation of polymer amount in the composites was based on that the weight loss in each temperature range is the combination of the weight loss due to water, polymer and bentonite. Therefore weight loss of composites was divided into three steps. The temperature range from 50 °C to 200 °C was assigned as the degradation of water. Between 200 °C to 500 °C was the degradation of polymer. The range of 500 °C - 850 °C belonged to the degradation of bentonite. However, the degradation of polymer in the composites was not completed at 500 °C. Hence, the amounts of polymer and bentonite in composites were calculated in the same way as described in literature [76] as described below.

$$Ax + B(1 - x) = C \quad (4.\ 1)$$

where A = the weight loss of pure pAPTMA-Cl, B = the weight loss of pure Na-bentonite, C = the weight loss of a composite, and x = fraction of pAPTMA-Cl

The amounts of polymer in the composites were included in Figure 4.5. It can be seen that the amounts of polymer in the composites were not significantly different (39.8 $\pm$ 3.1 %wt). This result supports the XRD result that the increase of monomer concentration from 7.5 %w/v to 22.5 %w/v has no effect on the increase of d-spacing.

Table 4.2 Literature reviews on temperature degradation assignments of bentonite, polymers and organic/clay.

Materials	A (°C)	B (°C)	C (°C)
Bentonite [124]	RT-200		400-800
Organic cations modified montmorillonite [128]	RT-150	200-550	550-700
Organosilane modified montmorillonite [131]	RT-160	500-550	
Organic cations modified montmorillonite [129]	87.9-135.5		556-636.6
Poly (3-acrylamidopropyl)trimethylammonium chloride-co-*N,N*-dimethylacrylamide [70]	RT-100	210-310	
Poly[3-(methacryloylamino)propyl] trimethylammonium chloride [126]	RT-100	100-500	

A = the loss of dehydration of adsorbed and interlayer water molecules

B = the loss of organic molecule

C = the loss of dehydroxylation of the structural OH units of the montmorillonite

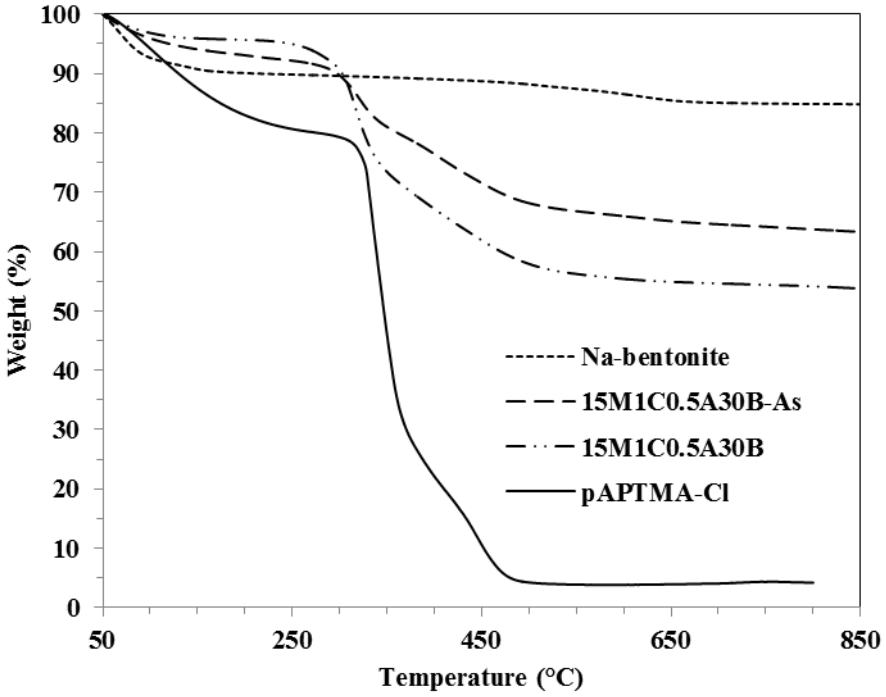

Figure 4.4 The TGA graphs of Na-bentonite (- - -), pAPTMA-Cl (—), and pAPTMACl/bentonite composites before (– · · –) and after (– – –) As(V) adsorption.

The As(V) adsorption of the composites was shown in Figure 4.6. The As(V) adsorption increased with increasing the monomer concentration.

According to the equation derived by Odian [132] the average number of monomer molecules (M_n) consumed (polymerized) per each radical is proportional to monomer concentration and inversely proportional to initiator concentration. In this section, the initiator concentration was fixed at 0.5% by mol. Therefore, the average number of monomer molecules consumed is dependent on the monomer concentration. Consequently, the polymer that prepared using the monomer concentration of 7.5 %w/v should provide lower the average number of monomer molecules in one chain than that prepared by using higher monomer concentrations.

The amounts of polymer before and after As(V) adsorption were calculated from TGA results and shown in Figure 4.5. The difference of the amount of polymer before and after As(V) adsorption might due to the dissolution of polymer from the

composites. The highest amount of polymer loss was obtained at the lowest monomer concentration. According to the previous description, the lowest monomer concentration gives the lowest the average number of monomer molecules in one chain; therefore, the water-soluble low M_n chain would be the easiest to leave the gallery of bentonite. In another word, the polymer prepared using higher monomer concentration contained the larger average number of monomer molecules in one chain that could have stronger interaction with the clay layers. Therefore, the composite prepared by using monomer concentration of 15 %w/v was selected for further study because it showed the lowest polymer loss after As(V) adsorption and is the lowest concentration that reach to constant the As(V) adsorption amount.

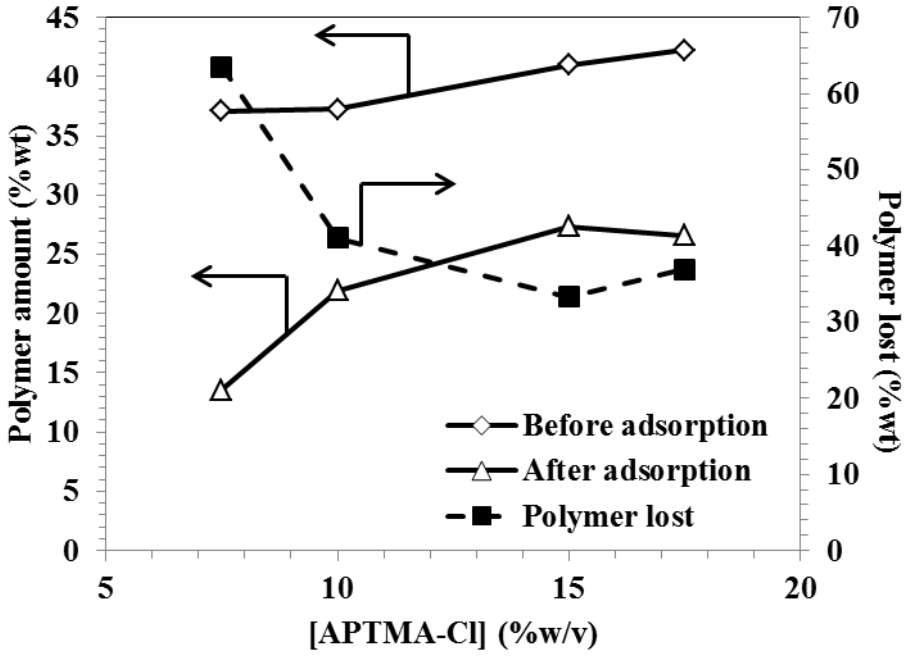

Figure 4.5 The polymer amount of pAPTMACl/bentonite composites before and after As(V) adsorption and their difference (Polymer lost).

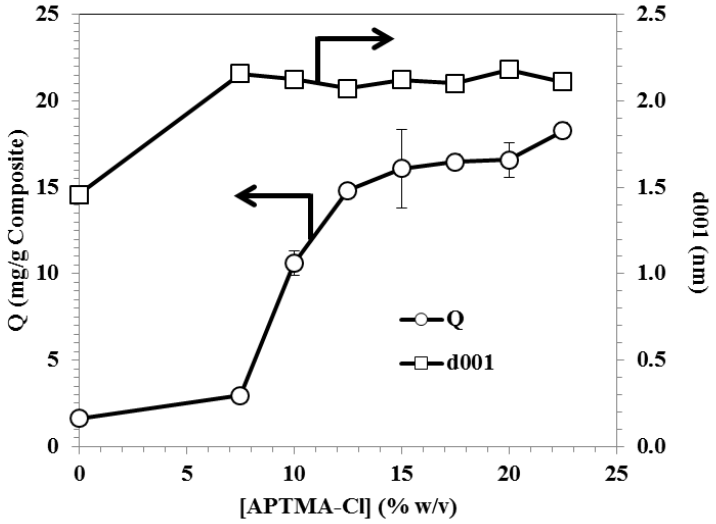

Figure 4.6 The d_{001} spacings and As(V) adsorption amounts with varied monomer concentrations.

4.1.1.2 Effect of cross-linker concentration

The effect of MBA cross-linker concentration was studied by synthesizing the polymer with various molar ratio of MBA cross-linker over APTMA-Cl monomers (0-5 %mol) and combining it with Na-bentonite the with fixed weight ratio of 70:30. The APTMA-Cl monomer concentration was fixed at 15 %w/v. The molar ratio of TEMED and APS over the APTMA-Cl monomer was fixed at 1:100 and 0.5:100, respectively.

All XRD patterns of the nanocomposites (Figure 4.7) show the shift of (001) peaks of bentonite to larger d-spacings (2.11 $\pm$ 0.04 nm) as compared to the d-spacing of Na-bentonite (1.46 nm). Similar to the previous section (4.1.1.1), the expansion of d-spacing was due to the intercalation of polymer cations into the layers of bentonite. However, as the molar ratio of MBA cross-linker to APTMA-Cl monomer varied from 1 to 4, the (001) d-spacing of bentonite did not shift, but the relative intensity decreased with increasing MBA cross-linker. According to the Debye-Scherrer equation, the peak width is inversely proportional to crystallinity, therefore, it suggest that increasing the MBA cross-linker amount decreased the crystallite size of the nanocomposite. The large amount of cross-linkers could lead to

uncontrollable size and shape of polymer that prevent the stacking of bentonite layers.

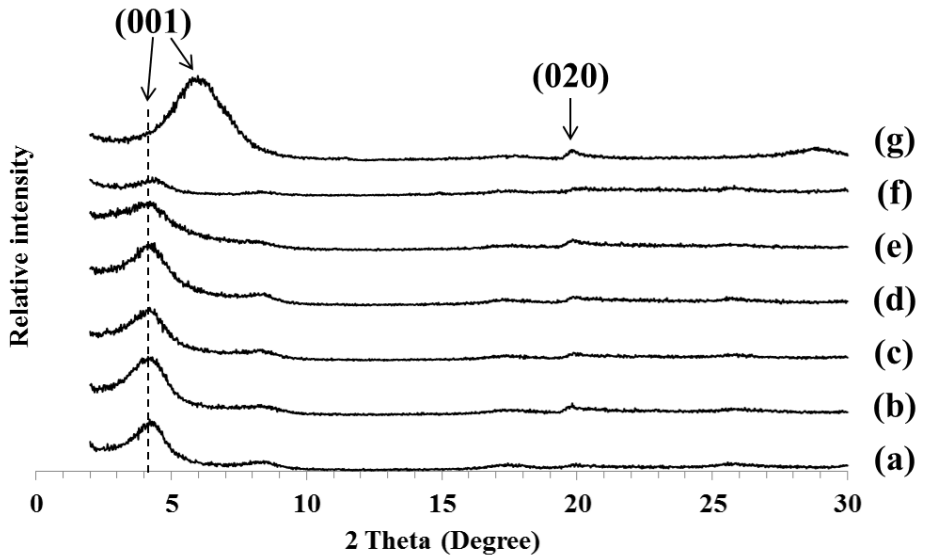

Figure 4.7 XRD patterns of pAPTMACl/bentonite composites of (a) 15M0C0.5A30B, (b) 15M1C0.5A30B, (c) 15M2C0.5A30B, (d) 15M3C0.5A30B, (e) 15M4C0.5A30B, (f) 15M5C0.5A30B, and (g) Na-bentonite

The As(V) adsorption of the composites (Figure 4.8) shows the slightly increase of the adsorption as the amount of cross-linker increased. However, the large error bar at high ration of cross-linker indicates the irreproducible results because of the uncontrollable synthesis.

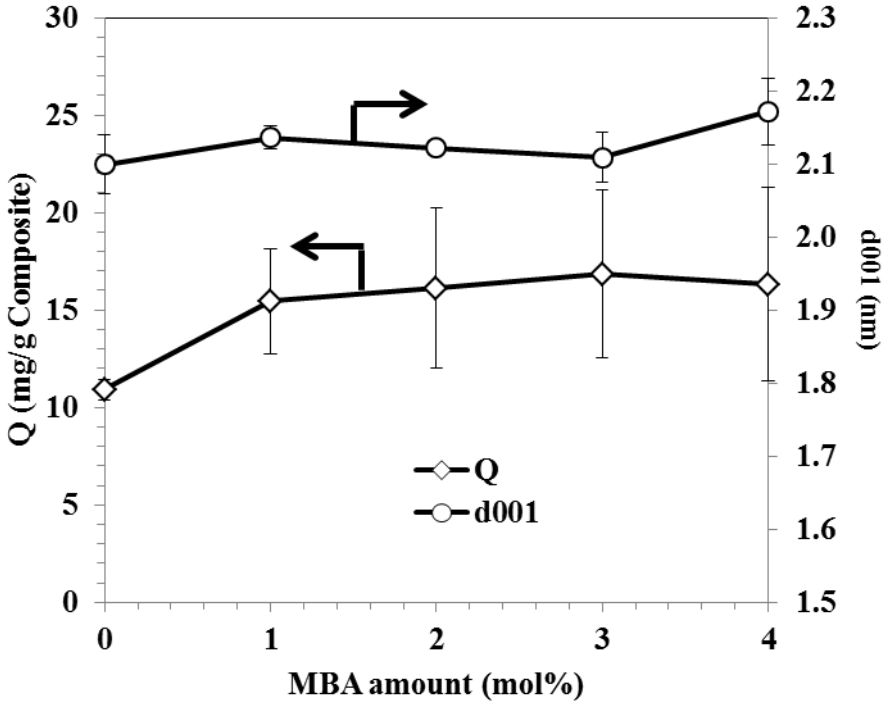

Figure 4.8 The As(V) adsorption and d_{001} of pAPTMA/bentonite composites at various MBA concentrations

4.1.1.3 Effect of Initiator concentration

The effect of APS initiator concentration was studied by synthesizing the polymer with various molar ratio of APS initiator concentration over APTMA-Cl monomer (0.5-5 %mole) and combining it with Na-bentonite with the fixed weight ratio of 70:30. The APTMA-Cl monomer concentration was fixed at 15 %w/v. The molar ratio of TEMED and MBA cross-linker over the APTMA-Cl monomer were fixed at 1:100.

All XRD patterns of the nanocomposites (Figure 4.9) shows the shift of (001) peaks of bentonite to larger d-spacings as compared to the d-spacing of Na-bentonite. The trend of d_{001} shown in Figure 4.10 became slightly smaller as the APS initiator concentration got higher. According to the equation derived by Odian [132] that the average number of monomer molecules consumed (polymerized) per each radical is proportional to monomer concentration and inversely proportional to

initiator concentration. In this section, the monomer concentration was fixed at 15% by w/v, therefore, the average number of monomer molecules consumed was dependent on the APS initiator concentration. Consequently, the polymer prepared from higher APS initiator concentration should yield the lower average number of monomer molecules in one chain than that prepared using lower APS initiator concentrations. The exception was given for the APS initiator concentration of 0.5 % by mole. It could be explained that too low concentration of APS initiator would retard the propagation step of polymer synthesis.

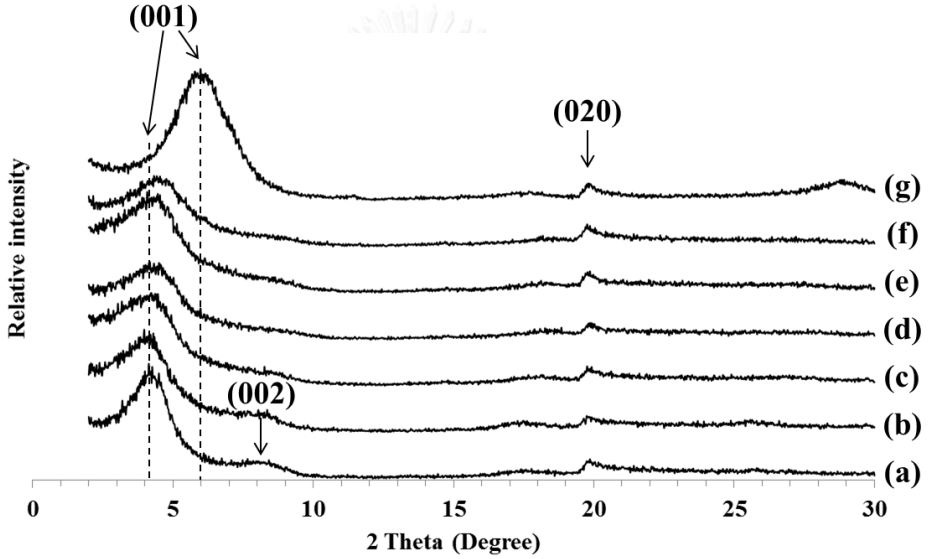

Figure 4.9 XRD patterns of pAPTMA/bentonite composites of (a) 15M1C0.5A30B, (b) 15M1C1A30B, (c) 15M1C2A30B, (d) 15M1C3A30B, (e) 15M1C4A30B, (f) 15M1C5A30B, and (g) Na-bentonite

The As(V) adsoption amount increased with increasing the APS initiator concentration up to 2 % mole. After that it slightly decreased upon the increasing of the initiator concentration as shown in Figure 4.10. The trend is similar to the trend of d-spacing in Figure 4.10. Since using 2 %mole of APS initiator gave the highest As(V) adsorption amount, the condition was selected for further studies.

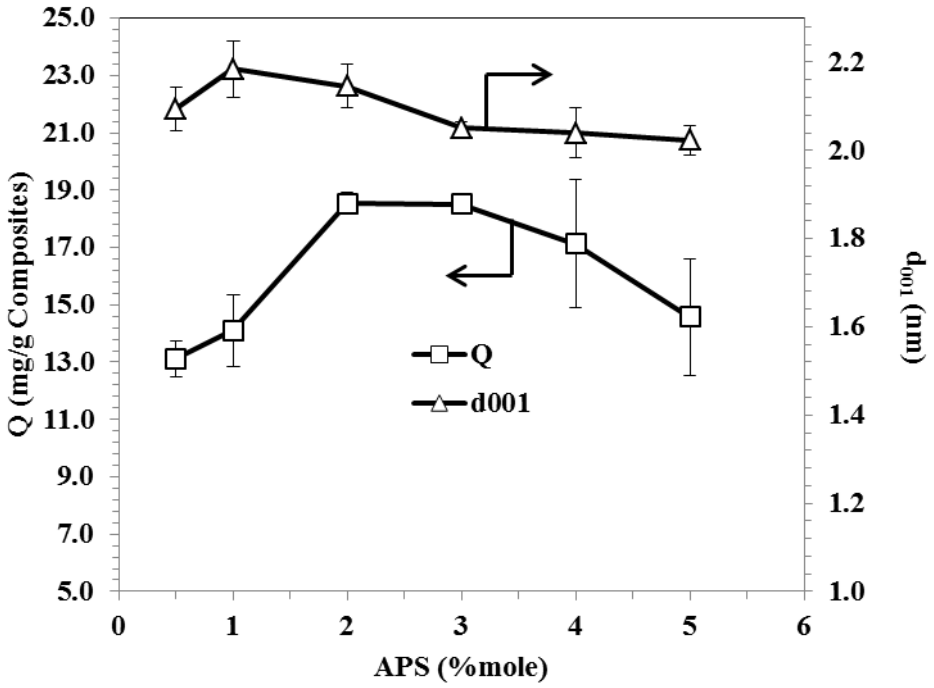

Figure 4.10 The As(V) adsorption amount and d_{001} of pAPTMACl/bentonite composites at various APS concentrations.

4.1.1.4 Effect of Na-bentonite concentration

All XRD patterns of the nanocomposites (Figure 4.11) shows the shift of (001) peaks of bentonite to larger d-spacings as compared to the d-spacing of Na-bentonite. The d-spacing of nanocomposites are summarized in Figure 4.12. For the composites with Na-bentonite concentration of 5 %wt, 10 %wt and 20 %wt, the d_{001} peak (2 theta around 4-6 degree) was hardly observed, suggested that these composites were exfoliated nanocomposites. For the composite with 30 %wt and 40 %wt Na-bentonite, the d_{001} peak shifted to lower 2 theta values, suggested that the composites were intercalated nanocomposites. For the composites with 50-70 %wt Na-bentonite, two d_{001} peaks of bentonite were observed. The first peak at around 6 degree belonged to d_{001} peak of Na-bentonite. The second peak at around 4.2 degree could be referred to d_{001} peak of intercalated bentonite. In conclusion, the amount of bentonite should not be higher than 40 %wt in order to obtain the pure phase of nanocomposites.

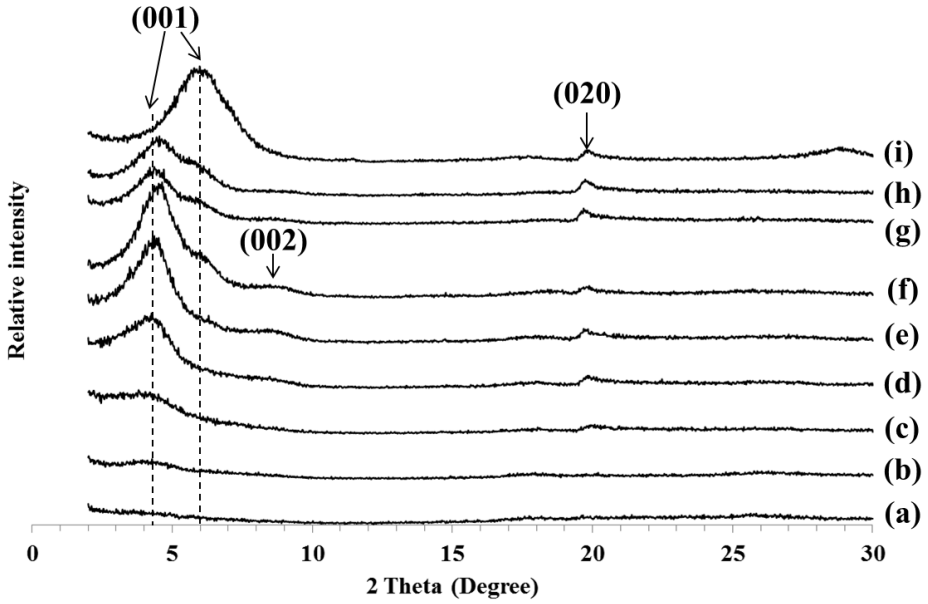

Figure 4.11 XRD patterns of pAPTMACl/bentonite composites of (a) 15M1C2A5B, (b) 15M1C2A10B, (c) 15M1C2A20B, (d) 15M1C2A30B, (e) 15M1C2A40B, (f) 15M1C2A50B, (g) 15M1C2A60B, (h) 15M1C2A70B, and (i) Na-bentonite

The As(V) adsorption amount of the composites decreased with increasing Na-bentonite concentration (Figure 4.12). Apparently it was due to the low adsorption capacity of bentonite. According to the basis that the bentonite acted as the supporter for the dispersion of pAPTMA polycation and held the composites into a solid phase, therefore, the decreasing of adsorption amount upon the increasing of the Na-bentonite concentration resulted from the decreasing of the pAPTMA polycation amount.

In order to compare the effect of Na-bentonite amount, the adsorption amounts per weight of polymer were calculated and shown in Figure 4.12**.** The As(V) adsorption amount per weight of polymer reached the maximum value of 47.7 mg/g polymer with the Na-bentonite amount of 30 %wt. Comparing with 15M1C2A30B, 15M1C2A40B and 15M1C2A50B showed lower As(V) adsorption amounts per weight of polymer. This might be due to their smaller d-spacing leading to harder access of arsenate anions into the confine spaces of bentonite to bind with polymercation. For 15M1C2A10B and 15M1C2A20B, although their polymer amount were higher than

that of 15M1C2A30B, their As(V) adsorption amounts per weight of polymer were lower as shown in Figure 4.13. This might be due to that the polymers leave the exfoliated nanocomposites easier than the intercalated nanocomposites resulted in decrease arsenate adsorption sites.

However, the calculated As(V) adsorption amounts per weight of polymer for the composites with Na-bentonite of 10-50 %wt (31.8-47.7 mg/g polymer) were higher than that of as-synthesized polymer (24.4 mg/g polymer).

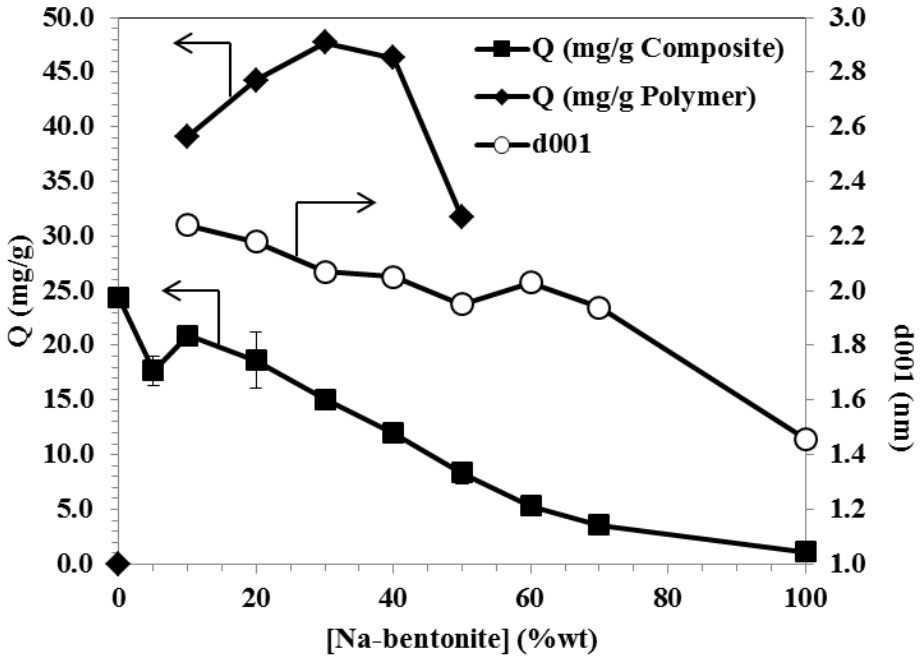

Figure 4.12 The As(V) adsorption and d_{001} of pAPTMA/bentonite composites at various Na-bentonite concentrations. (15 %w/v APTMA-Cl, 1 %mole MBA, 2 %mole APS)

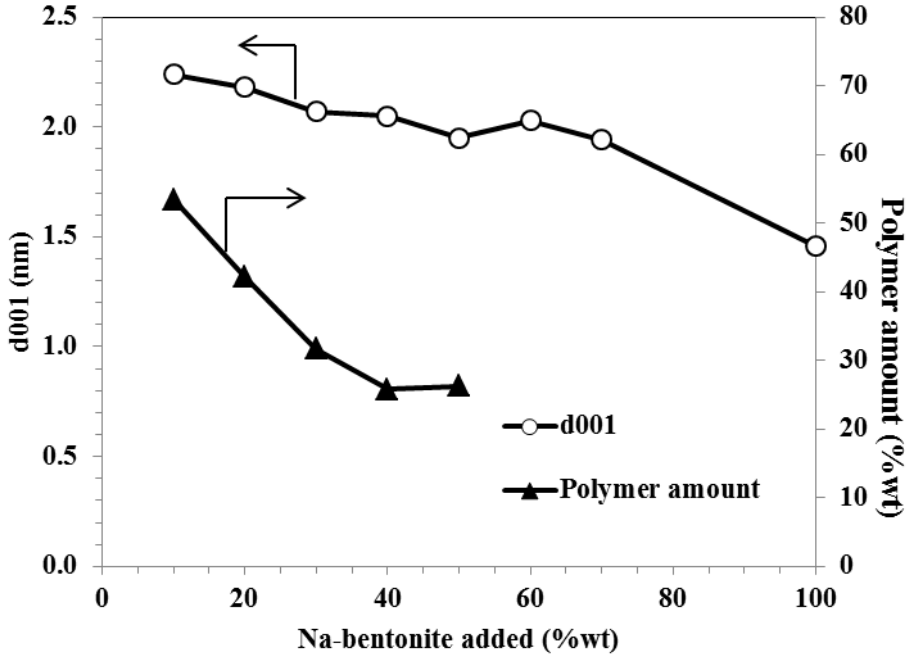

Figure 4.13 The d_{001} and polymer amounts of pAPTMA/bentonite composites at various Na-bentonite concentrations. (15 %w/v APTMA-Cl, 1 %mole MBA, 2 %mole APS)

According to all studied parameters, the optimum condition for the pAPTMA/bentonite nanocomposite prepared via solution intercalation method is that:

APTMA-Cl monomer concentration = 15 % w/v,

MBA cross-linker concentration = 1 % mole (base on APTMA-Cl monomer),

APS initiator concentration = 2 % mole (base on APTMA-Cl monomer),

and Na-bentonite concentration = 30 % wt (base on APTMA-Cl monomer).

4.1.2 Poly([2-(acryloyloxy)ethyl]trimethylammonium chloride)

4.1.2.1 Effect of monomer concentration

This section used [2-(acryloyloxy)ethyl]trimethylammonium chloride (AETMA-Cl) as monomer. The concentration of AETMA-Cl monomer was varied from 7.5 %w/v to 15 %w/v while the molar ratio of MBA, TEMED and APS over the APTMA-Cl monomer was fixed at 1:100, 1:100 and 0.5:100, respectively. The as-synthesized polymer was then mixed with Na-bentonite by fixed the weight ratio of 70:30.

The FTIR spectra of Na-bentonite, the pAETMA/bentonite composite (7.5M1C0.5A30B) and pAETMA-Cl are shown in Figure 4.14. The characteristic peaks of Na-bentonite appear at 3627 cm^{-1} (X – OH, X = Al, Mg), 3441 cm^{-1}, 1644 cm^{-1} (H – O – H) and 1034 cm^{-1} ($Si(Al)O_4$) [36, 124, 125]. The FTIR spectrum of pAETMA-Cl in Figure 4.14 (c) shows the characteristic peaks at 3429 cm^{-1} (– N – R_3), 1735 cm^{-1} (C = O) and 1168 cm^{-1} (R – O – R) [71]. It can be seen that the FTIR spectrum of composite (7.5M1C0.5A30B) contains both the characteristic peaks of Na-bentonite and pAETMA-Cl. The results suggested that the composite was composed of both bentonite and pAETMA-Cl. The FTIR spectra of the other composites show the same result with 7.5M1C0.5A30B. The characteristic absorption bands for all peaks were summarized in Table 4.3.

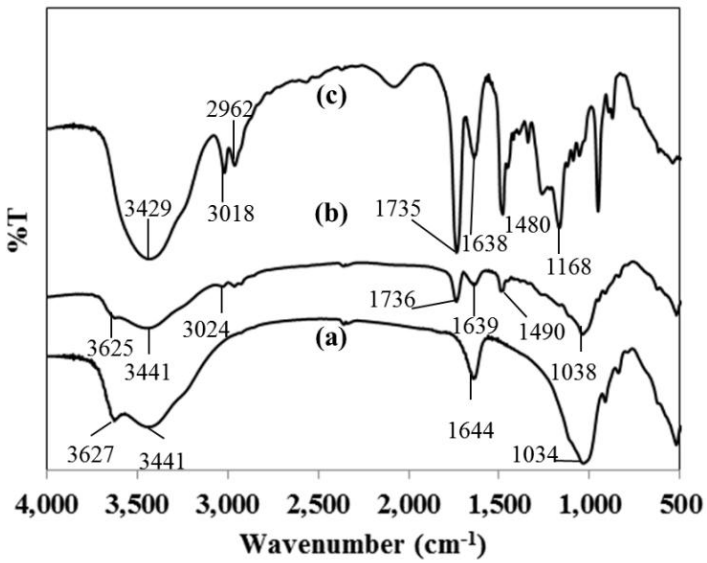

Figure 4.14 FTIR spectra of (a) Na-bentonite, (b) 7.5M1C0.5A30B and (c) pAETMA-Cl.

Table 4.3 FTIR spectral assignments of Na-bentonite, 7.5M1C0.5A30B and pAETMA-Cl

Band assignments	Na-bentonite (cm^{-1})	7.5M1C0.5A30B (cm^{-1})	pAETMA-Cl (cm^{-1})
ν(X – O – H), X = Al, Mg[a]	3627	3625	-
ν(H – O – H)[a]	3441	3441	3429
δ(H – O – H)[a]	1644	1639	1638
ν(Si – O)[a]	1034	1038	-
δ(Al – Al – OH)[a]	914	NA	-
δ(Al – Mg– OH)[a]	835	838	-
δ(Al – O – Si)[a]	521	517	-
δ(Si – O – Si)[a]	466	460	-
(– N – R_3)[b]	-	3441	3429
ν(CH_3) or ν(– CH_2 –)[b]		3024, 2961	3018, 2962
δ(– $N^+(CH_3)_3$[b]	-	1490	1480
δ(– CH_2 –)[b]	-	1490	1480
ν(C = O)[b]	-	1736	1735
(R – O – R)[b]	-	NA	1168

ν = stretching, δ = bending, [a]data from [36, 124, 125], [b]data from [71, 133-135], NA = not available

All XRD patterns of the nanocomposites (Figure 4.15) shows the shift of (001) peaks of bentonite to larger d-spacings as compared to the d-spacing of Na-bentonite. The intensities of (001) peaks of bentonite became very low and broadening suggesting the exfoliated nanocomposites were obtained.

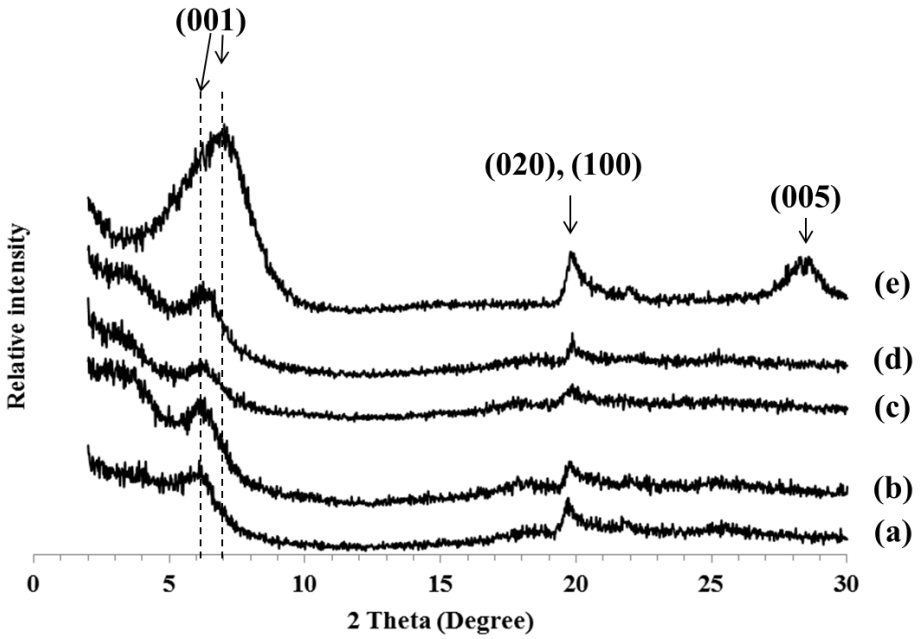

Figure 4.15 XRD patterns of pAETMACl/bentonite composites of (a) 7.5M1C0.5A30B, (b) 10M1C0.5A30B, (c) 12.5M1C0.5A30B, (d) 15M1C0.5A30B, and (e) Na-bentonite

The amount of polymer in nanocomposites was estimated using TGA. As shown in Figure 4.16, Na-bentonite possesses the two-stepped [124, 128, 129] weight loss upon increasing temperature, (i) the loss of adsorbed and intercalated water between 50 – 180 °C (9.9%) and (ii) the degradation of clay layered structure starting from 500 °C (5.3%). For the bulk pAETMA-Cl, the weight loss went through 3 steps [134, 135], (i) the loss of the adsorbed water up to 150 °C, (ii) the degradation of the pending groups on the polymer chain starts at 225 °C, and (iii) the decomposition of the main chains starts at 350 °C. The characteristic weight loss of the nanocomposites could be predicted as the combination of the individual components. At the temperature up to 150 °C, the amount of water in the nanocomposites was significantly lower than its individual components. This could be explained in similar way to section 4.1.1.1. that the pAETMA polycation was trapped inside bentonite galleries instead of the aquated Na^+ ions, resulting to less amount of intercalated water [130]. The characteristic loss of intercalated pAETMA appeared as that of the bulk pAETMA-Cl, except that the decomposition temperature

would not be the sharp cut due to the confined space between bentonite layers trapping the decomposition products. The calculation of polymer amount in the composites was based on that the weight loss in each temperature range is the combination of the weight loss due to water, polymer and bentonite. The weight loss of composites was derived into three steps. The temperature range from 50 °C to 200 °C was assigned as the loss of water. For the temperature range from 200 °C to 750 °C was assigned as the degradation of polymer. Finally, the temperature range from 500 °C to 850 °C was assigned as the degradation of bentonite. It can be seen the overlap of the weight loss due to polymer and bentonite, therefore, the amount of polymer and bentonite in composites were calculated in the same way as in the section 4.1.1.1.

The amounts of polymer in the composites were included in Figure 4.17. It can be seen that the amounts of polymer in the composites slightly increased with increasing AETMA-Cl monomer concentration.

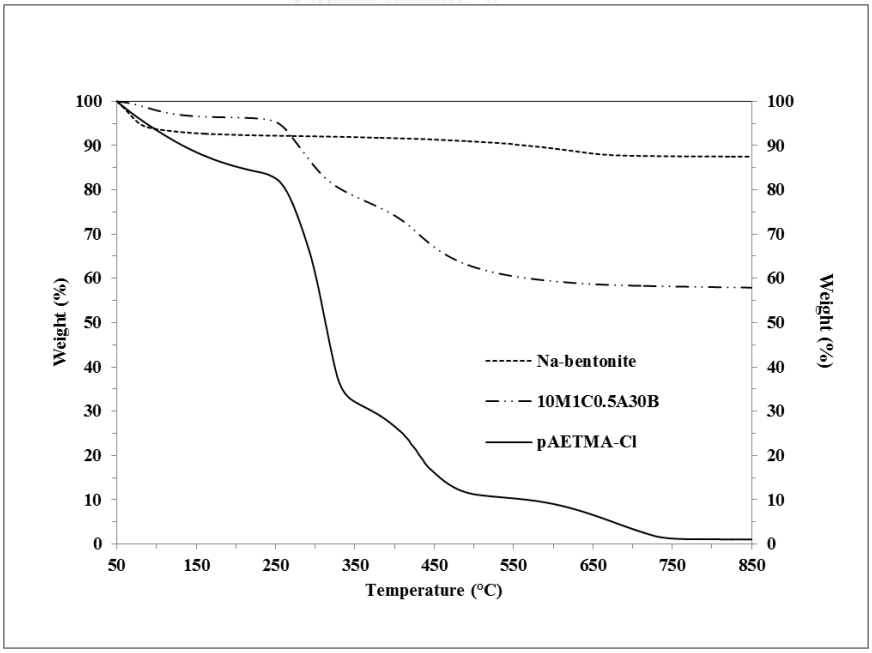

Figure 4.16 The TGA graphs of Na-bentonite (- - -), pAETMA-Cl (—), and pAETMACl/bentonite composites (– · · –).

All composites were used to remove As(V) from aqueous solution. The results were included in Figure 4.17. The As(V) adsorption amount increased with increasing AETMA-Cl monomer concentration. However, to compare the effect of AETMA-Cl monomer concentration, the calculated adsorption amounts per weight of polymer were calculated. The As(V) adsorption amount per weight of polymer reached the constant with the AETMA-Cl monomer concentration of 10 %w/v. Therefore, the composite prepared by using monomer concentration of 10 %w/v was selected for further.

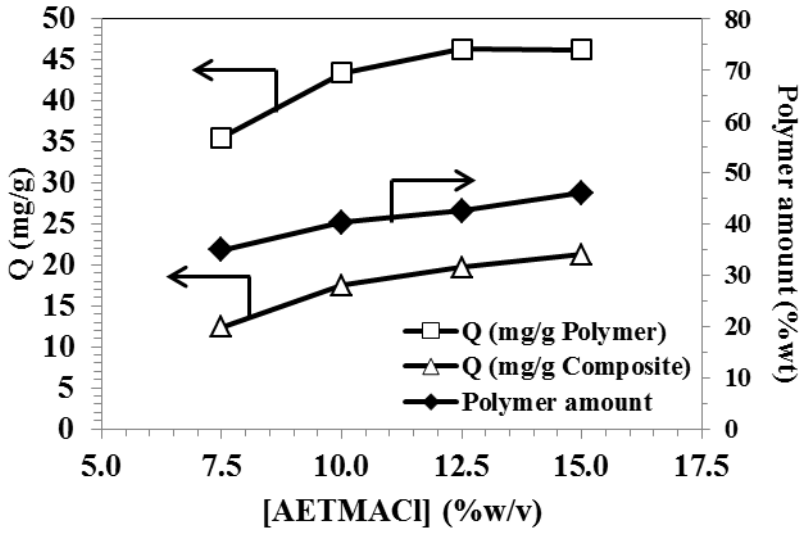

Figure 4.17 The As(V) adsorption and polymer amounts of pAETMA/bentonite composites with various monomer concentrations.

4.1.2.2 Effect of cross-linker concentration

The effect of MBA cross-linker concentration was studied by synthesizing the polymer with various molar ratio of MBA cross-linker over AETMA-Cl monomers (0-5 %mol) and combining it with Na-bentonite with the fixed weight ratio of 70:30. The AETMA-Cl monomer concentration was fixed at 10 %w/v. The molar ratio of TEMED and APS over the AETMA-Cl monomer was fixed at 1:100 and 0.5:100, respectively.

The polymer prepared by using MBA cross-linker higher than 3 %mole was in a solid phase; therefore, they could not mix well with Na-bentonite. All XRD patterns

of the nanocomposites (Figure 4.18) shows the shift of (001) peaks of bentonite to larger d-spacings as compared to the d-spacing of Na-bentonite. It can be noticed that the intensities of (001) peaks of bentonite were very low suggesting that the composites were the intercalated nanocomposites which nearly became exfoliated nanocomposites, excepted for 3 %mole.

.

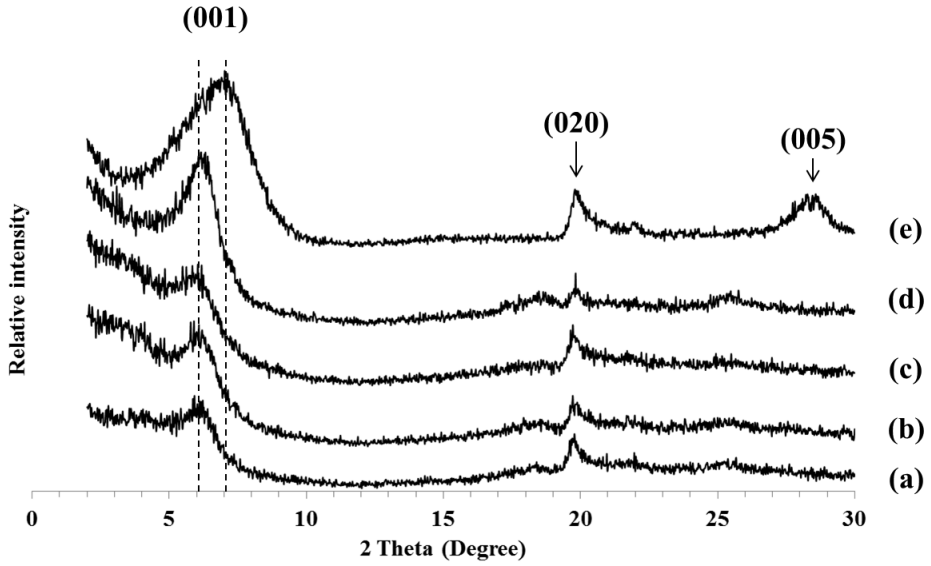

Figure 4.18 XRD patterns of pAETMA/bentonite composites of (a) 10M0C0.5A30B, (b) 10M1C0.5A30B, (c) 10M2C0.5A30B, (d) 10M3C0.5A30B, and (e) Na-bentonite

The As(V) adsorption of the composites (Figure 4.19) shows the slightly increase of the adsorption as the amount of cross-linker increased. However, the large error bar at high ration of cross-linker indicates the irreproducible results because of the uncontrollable synthesis.

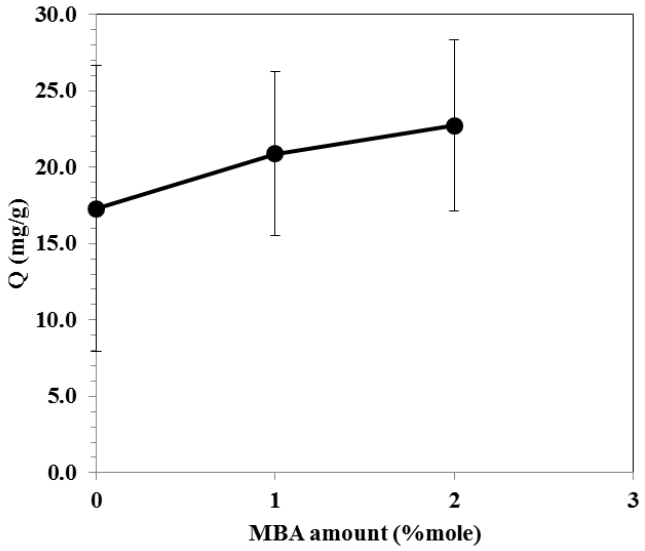

Figure 4.19 the As(V) adsorption of pAETMA/bentonite composites at various MBA concentrations.

4.1.2.3 Effect of Initiator concentration

The effect of APS initiator concentration was studied by synthesizing the polymer with various molar ratio of APS initiator concentration over AETMA-Cl monomer (0.5-5 %mole) and then combined it with Na-bentonite with the fixed weight ratio of 70:30. The AETMA-Cl monomer concentration was fixed at 10 %w/v. The molar ratio of TEMED and MBA cross-linker over the AETMA-Cl monomer were fixed at 1:100.

All XRD patterns of the nanocomposites (Figure 4.20) shows the shift of (001) peaks of bentonite to larger d-spacings as compared to the d-spacing of Na-bentonite. However, the (001) peak of bentonite from 0.5-2 % mole APS were broader than that from 3-5 %mole suggested that the composite from 0.5-2 % mole APS were the intercalated nanocomposites which nearly became exfoliated nanocomposites while the composite from 3-5 % mole APS were the pure phase of intercalated nanocomposites.

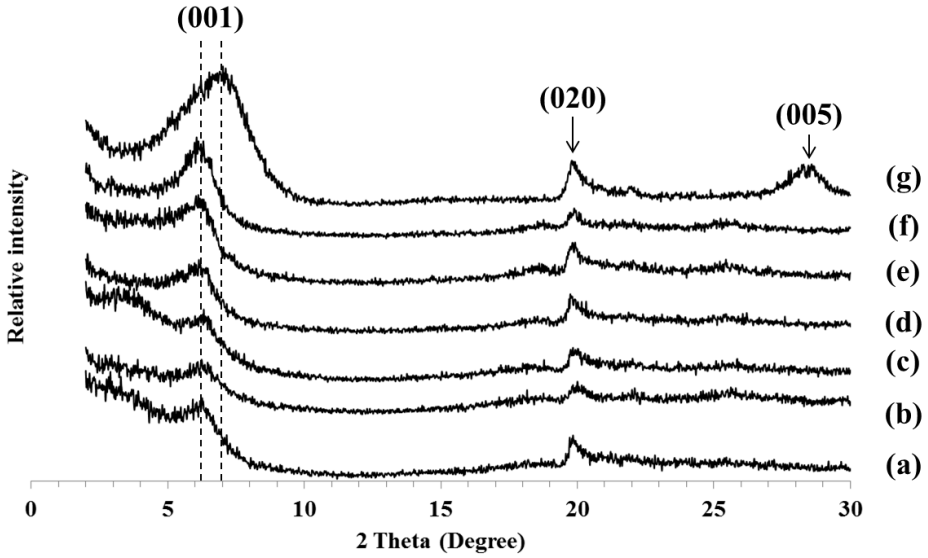

Figure 4.20 XRD patterns of pAETMA/bentonite composites of (a) 10M1C0.5A30B, (b) 10M1C1A30B, (c) 10M1C2A30B, (d) 10M1C3A30B, (e) 10M1C4A30B, (f) 10M1C5A30B, and (g) Na-bentonite.

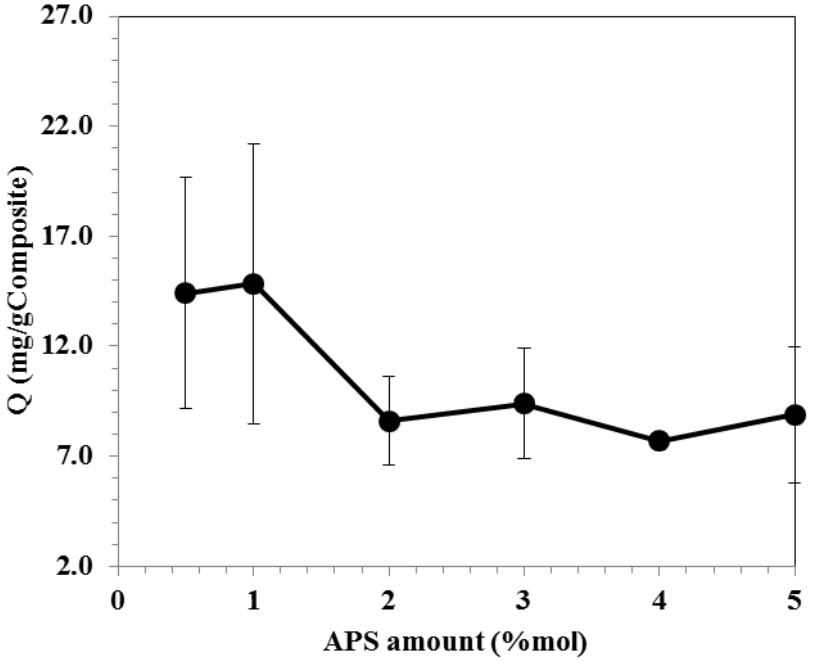

Figure 4.21 The As(V) adsorption of pAETMA/bentonite composites at various APS concentrations.

The samples prepared from 0.5 and 1 % mole of APS initiator exhibited higher As(V) adsorption amount than that from 2-5 % mole as shown in Figure 4.21. This might relate to the structure of nanocomposites. Therefore the used of 0.5 % mole APS initiator was selected for further studies.

4.1.2.4 Effect of Na-bentonite concentration

All XRD patterns of the nanocomposites (Figure 4.22) shows the shift of (001) peaks of bentonite to larger d-spacings as compared to the d-spacing of Na-bentonite. The d-spacing of nanocomposites were summarized in Figure 4.23. For the composites with Na-bentonite of 5 %wt, 10 %wt and 20 %wt, the d_{001} peak was hardly observed, suggested that these composites were exfoliated nanocomposites. This result is similar to the composite of pAPTMA-Cl and bentonite in section 4.1.1.4. For the composite with 30-70 %wt Na-bentonite, the (001) peak around 6 – 7 degree with a shoulder at lower 2 theta was observed, indicating the various degrees of clay expansion that could lead from intercalation to exfoliation.

The polymer amounts of composites (Figure 4.23) decreased with increasing the Na-bentonite concentration. This trend was similar to the trend of d-spacing of bentonite suggested that the expansion of d-spacing related to the amount of polymer in the composites. In other word, the expansion of d-spacing should be due to more polymercation inserted into the gallery of bentonite.

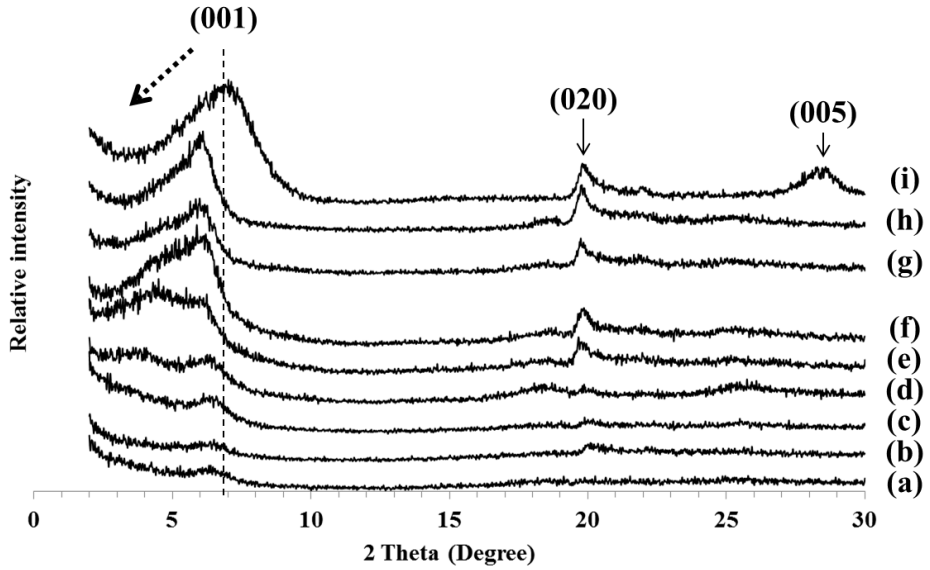

Figure 4.22 XRD patterns of pAETMA/bentonite composites of (a) 10M1C0.5A5B, (b) 10M1C0.5A10B, (c) 10M1C0.5A20B, (d) 10M1C0.5A30B, (e) 10M1C0.5A40B, (f) 10M1C0.5A50B, (g) 10M1C0.5A60B, (h) 10M1C0.5A70B, and (i) Na-bentonite.

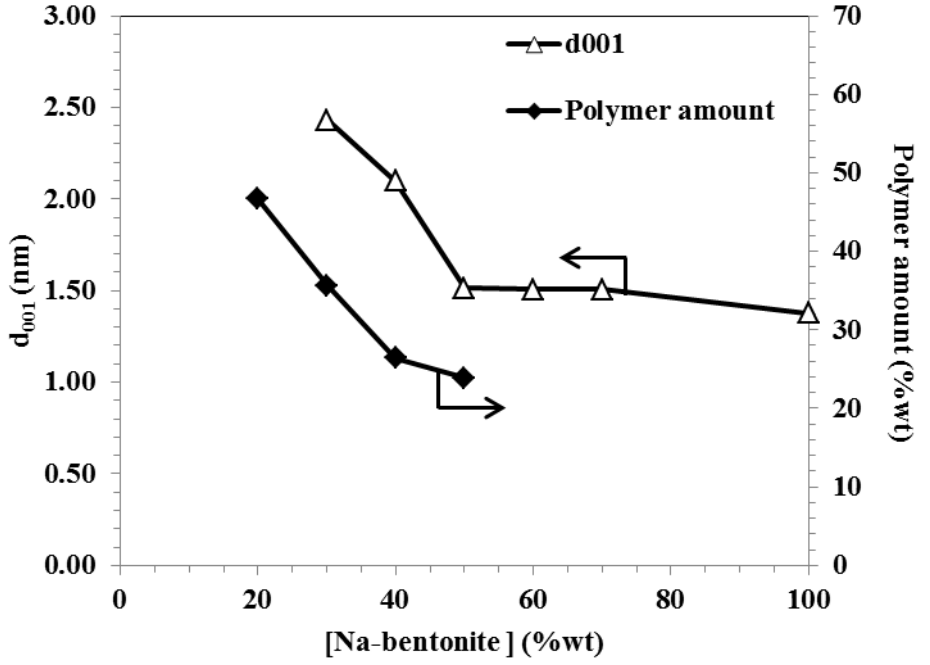

Figure 4.23 Polymer amount and d_{001} of pAETMA/bentonite composites at various Na-bentonite concentrations.

The As(V) adsorption amount of the composites decreased with increasing the Na-bentonite concentration (Figure 4. 24). Apparently it was due to the low adsorption capacity of bentonite. According to the basis that the bentonite acted as the supporter for the dispersion of pAETMA polycation and held the composites into a solid phase, therefore, the decreasing of adsorption amount upon the increasing of the Na-bentonite concentration resulted from the decreasing of the pAETMA polycation amount.

In order to compare the effect of Na-bentonite amount, the adsorption amounts per weight of polymer were calculated and shown in Figure 4. 24. The As(V) adsorption amount per weight of polymer reached the maximum value of 46.2 mg/g polymer with the Na-bentonite amount of 40 %wt. Comparing with 10M1C0.5A40B, 10M1C0.5A50B showed significant lower As(V) adsorption amounts per weight of polymer. This might be due to their smaller d-spacing leading to harder access of arsenate anions into the confine spaces of bentonite to bind with polymercation. For 10M1C0.5A20B and 10M1C0.5A30B, the As(V) adsorption amounts per weight of polymer were also lower than that of 10M1C0.5A40B. According to the XRD results, the composite with Na-bentonite of 20 %wt was an exfoliated nanocomposite and that of 30 %wt was in mixed-stage; therefore the water-soluble pAPTMA might leave the composite during the adsorption process due to the large expansion of bentonite layers. The loss of polymer resulted to low adsorption capacity of arsenate anions.

However, the calculated As(V) adsorption amounts per weight of polymer for the composites with Na-bentonite concertration of 20-50 %wt (36-46 mg/g polymer) are higher than that of bulk polymer (30 mg/g polymer).

Because the pAETMA/bentonite nanocomposite with Na-bentonite of 40 %wt showed the highest As(V) adsorption amount per weight of polymer, therefore it was selected for further study.

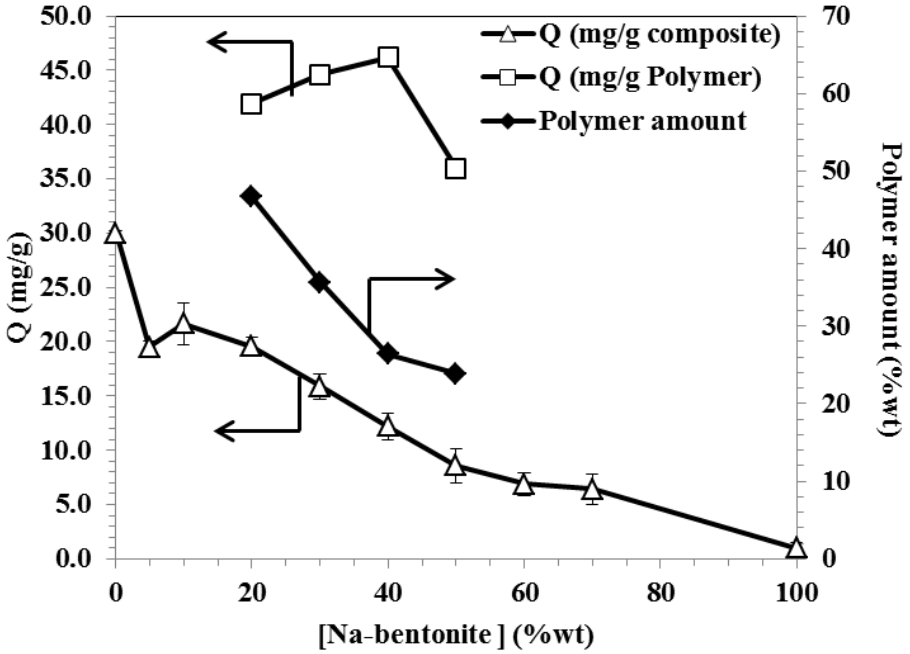

Figure 4. 24 The As(V) adsorption amount and d_{001} of pAETMA/bentonite composites at various Na-bentonite concentrations. (10 %w/v AETMA-Cl, 1 %mole MBA, 0.5 %mole APS)

According to all studied parameters, the optimum condition for the pAETMA/bentonite nanocomposite prepared via solution intercalation method is that:

APTMA-Cl monomer concentration = 10 % w/v,

MBA cross-linker concentration = 1 % mole (base on APTMA-Cl monomer),

APS initiator concentration = 0.5 % mole (base on APTMA-Cl monomer),

and Na-bentonite concentration = 40 % wt (base on APTMA-Cl monomer).

4.2 Synthesis of polymer/bentonite nanocomposites via *in-situ* intercalative polymerization method

The *in-situ* intercalative polymerization method was employed in order to compare with the previous synthesis technique. In this method, all precursors (APTMA-Cl monomer, MBA cross-linker, TEMED and Na-bentonite) were mixed and stirred overnight before adding APS initiator.

4.2.1 Poly(3-acrylamidopropyl)trimethylammonium chloride)

4.2.1.1 Effect of cross-linker concentration

The concentration of MBA cross-linker was varied from 0 % to 5 % mole while the weight ratio of Na-bentonite and APTMA-Cl monomer was fixed at 10:90, the molar ratio of TEMED and APS over the APTMA-Cl monomer was fixed at 1:100 and 0.5:100, respectively.

The FTIR spectra of Na-bentonite, the pAPTMA/bentonit composite (1C0.5A10B) and pAPTMA-Cl are shown in Figure 4.25. The characteristic peaks of Na-bentonite appear at 3627 cm^{-1} (X – OH, X = Al, Mg), 3441 cm^{-1}, 1644 cm^{-1} (H – O – H) and 1034 cm^{-1} ($Si(Al)O_4$) [36, 124, 125]. The FTIR spectrum of pAPTMA-Cl in Figure 4.25 (c) shows the characteristic peaks at 3449 cm^{-1} (H – O – H), 2944 cm^{-1} (C_{sp3} – H), 1649 cm^{-1} (C = O amide) and 1480 cm^{-1} (C – N amide) [126]. It can be seen that the FTIR spectrum of composite (1C0.5A10B) contains both the characteristic peaks of Na-bentonite and pAPTMA-Cl. The results suggested that the composite was composed of both bentonite and pAPTMA-Cl. The FTIR spectra of the other composites show the same result 1C0.5A10B. The characteristic absorption bands were summarized in Table 4.4. FTIR spectra of composites produced by this method were similar to those produced by the solution intercalation method.

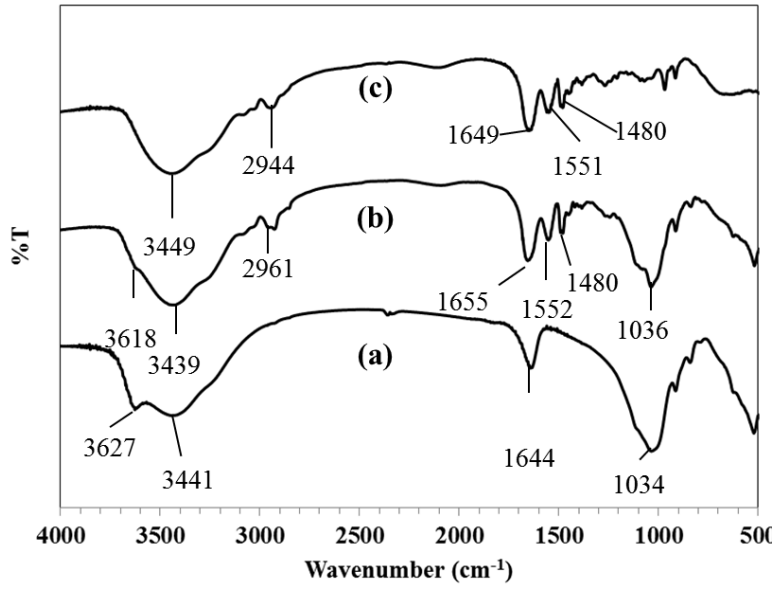

Figure 4.25 FTIR spectra of (a) Na-bentonite, (b) 1C0.5A10B and (c) pAPTMA-Cl.

Table 4.4 FTIR spectral assignments of Na-bentonite, 1C0.5A10B and pAPTMA-Cl

Band assignment	Na-bentonite (cm^{-1})	1C0.5A10B (cm^{-1})	pAPTMA-Cl (cm^{-1})
υ(X – O – H), X = Al, Mg[a]	3627	3618	-
υ(H – O – H)[a]	3441	3439	
δ(H – O – H)[a]	1644	1655	
υ(Si – O)[a]	1034	1036	-
δ(Al – Al – OH)[a]	914	914	-
δ(Al – Mg– OH)[a]	835	837	-
δ(Al – O – Si)[a]	521	518	-
δ(Si – O – Si)[a]	466	465	
υ(N – H) or υ(O – H)[b]		3439	3449
		3077	3077
υ(C – H)[b]	-	2961	2944
υ(C = O)[b]		1655	1649
δ(N – H)[b]	-	1552	1551
δ(N – H) of $RN^{+}(CH_3)_3$[b]	-	1480	1480
		1446	1443
υ(C – N)[b]		1244	1268

ν = stretching, δ = bending, [a]data from [36, 124, 125], [b]data from [70, 126, 127]

All XRD patterns of the nanocomposites (Figure 4.26) shows the shift of (001) peaks of bentonite to larger d-spacings (2.04 $\pm$ 0.03 nm) as compared to the d-spacing of Na-bentonite (1.46 nm), while the d-spacing of (020) peaks do not change. The (001) d-spacings of all samples were summarized in Figure 4.27.

Similar to the previous section (4.1.1.1), the expansion of d-spacing was due to the intercalation of polymer cations into the layers of bentonite. However, as the molar ratio of MBA cross-linker to APTMA-Cl monomer varied from 0 to 5, the (001) d-spacing of bentonite did not shift, but the relative intensity decreased with

increasing MBA cross-linker. According to the Debye-Scherrer equation, the peak width is inversely proportional to crystallinity, therefore, it suggest that increasing the MBA cross-linker amount decreased the crystallite size of the nanocomposite. The large amount of cross-linkers could lead to uncontrollable size and shape of polymer that prevent the stacking of bentonite layers.

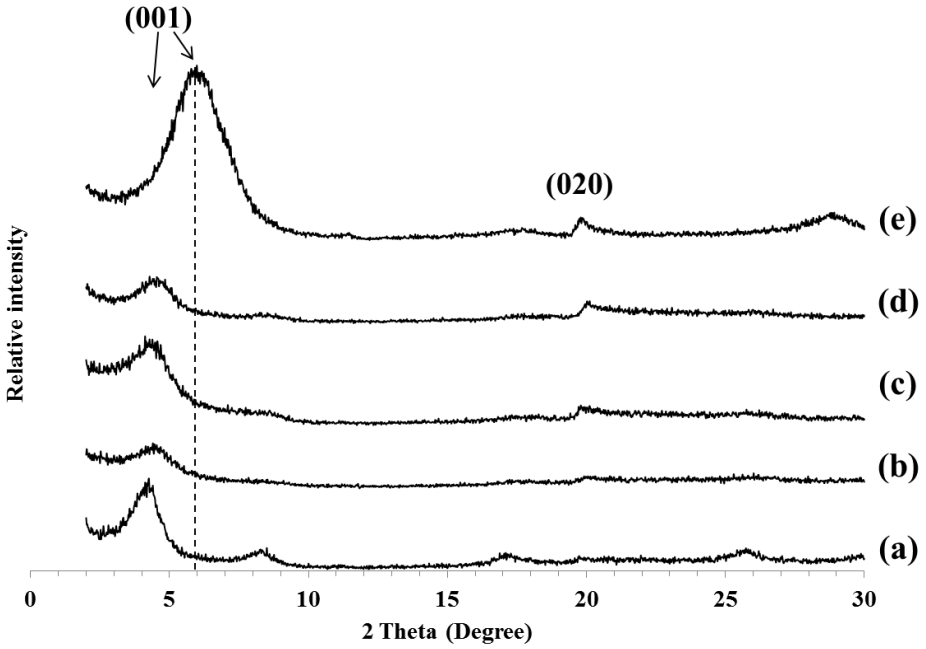

Figure 4.26 XRD patterns of pAPTMA/bentonite composites of (a) 0C0.5A10B, (b) 1C0.5A10B, (c) 3C0.5A10B, (d) 5C0.5A10B and (e) Na-bentonite.

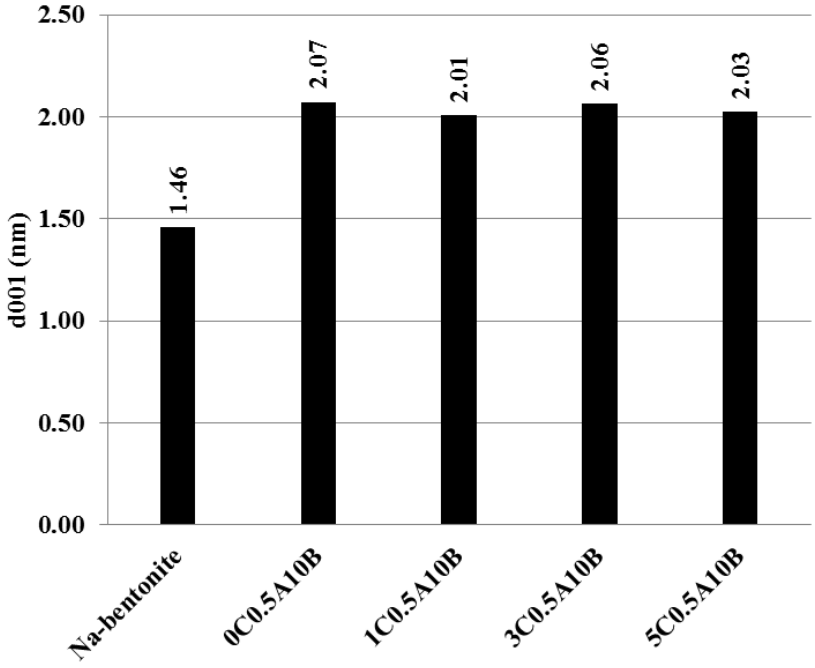

Figure 4.27 The d_{001} spacings of composites with varied MBA cross-linker concentrations.

The amount of polymer in nanocomposites was estimated using TGA. As shown in Figure 4.28, the characteristic weight loss of the nanocomposites could be predicted as the combination of the individual components. The characteristic loss of intercalated pAPTMA appeared as that of the bulk pAPTMA-Cl, except that the decomposition temperature would not be the sharp cut due to the confined space between bentonite layers trapping the decomposition products. The calculation of polymer amount in the composites was based on that the weight loss in each temperature range is the combination of the weight loss due to water, polymer and bentonite. Therefore weight loss of composites was divided into three steps and could be explained similar to section 4.1.1.1.

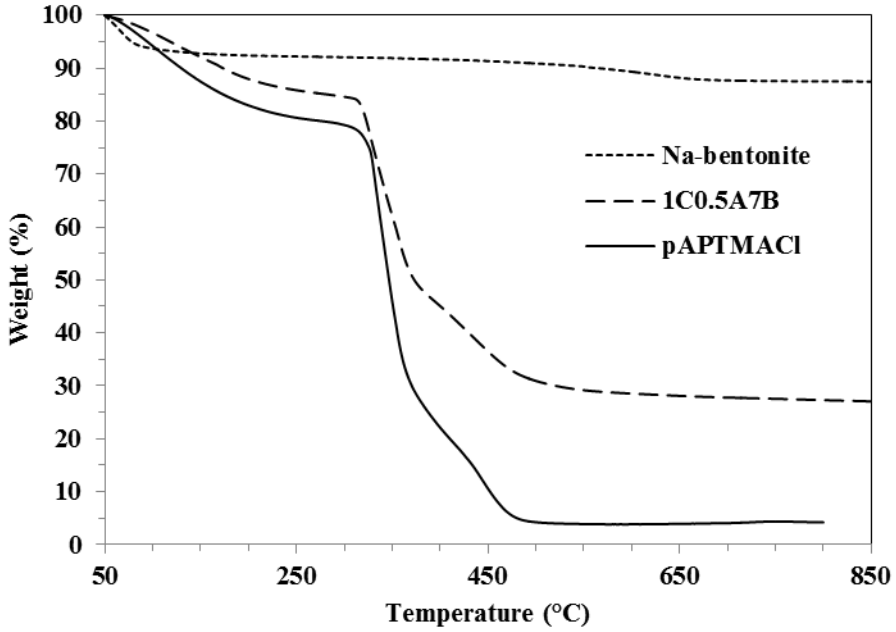

Figure 4.28 The TGA graphs of Na-bentonite (- - -), pAPTMA-Cl (—), and pAPTMACl/bentonite composites (– – –).

The As(V) adsorption of the composites (Figure 4.29) shows the dramatically increase of the adsorption as the amount of cross-linker increased and became constant when the MBA cross-linker concentration reached 3 % mole. This might be related to the crystallite size of composites which described in previous description. Therefore, the composite prepared by using MBA concentration of 3 % mole was selected for further study because it is the lowest concentration that reach to constant the As(V) adsorption amount.

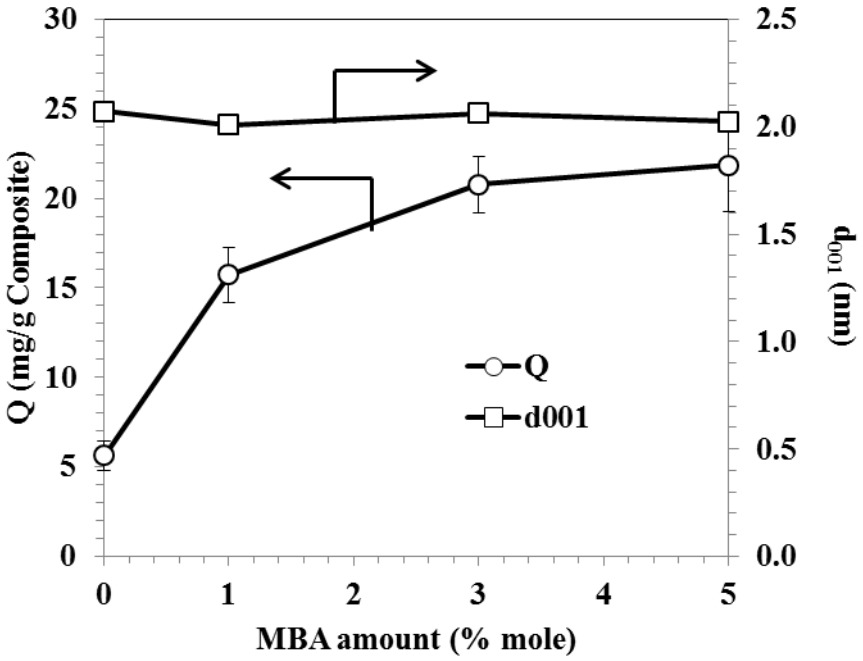

Figure 4.29 The d_{001} spacings and As(V) adsorption amounts with varied MBA concentrations.

4.2.1.2 Effect of Initiator concentration

The effect of APS initiator concentration was studied by varying the molar ratio of APS initiator concentration over APTMA-Cl monomer (0.5-5 %mole), while the weight ratio of Na-bentonite and APTMA-Cl monomer was fixed at 10:90, the molar ratio of TEMED and MBA over the APTMA-Cl monomer was fixed at 1:100 and 3:100, respectively.

The XRD patterns of the nanocomposites are shown in Figure 4.30. The shape of (001) peak of bentonite became broader as the APS initiator concentration increase.

The products can be classified into two groups. The first group from using the APS initiator concentration of 0.25-1 % mole shown the shift of (001) peaks of bentonite to larger d-spacings as compared to the d-spacing of Na-bentonite. It suggested the intercalated nanocomposite were obtained. In contrast, for the second group from using the APS initiator of 3 % mole and 5 % mole, the (001) peak of

bentonite disappear while the (020) peak still remained suggesting the exfoliated nanocomposite were obtained.

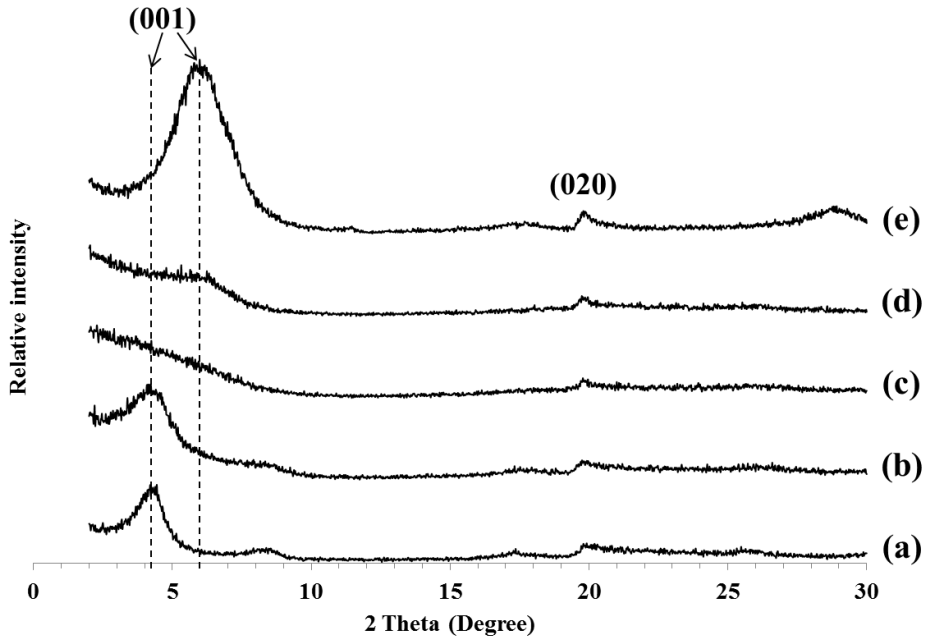

Figure 4.30 XRD patterns of pAPTMA/bentonite composites of (a) 3C0.25A10B, (b) 3C1A10B, (c) 3C3A10B, (d) 3C5A10B and (e) Na-bentonite.

The As(V) adsorption amount dramatically increase with increasing the APS initiator concentration from 0.25 % mole to 1 % mole. After that it slightly decreased upon the increasing of the initiator concentration as shown in Figure 4.31.

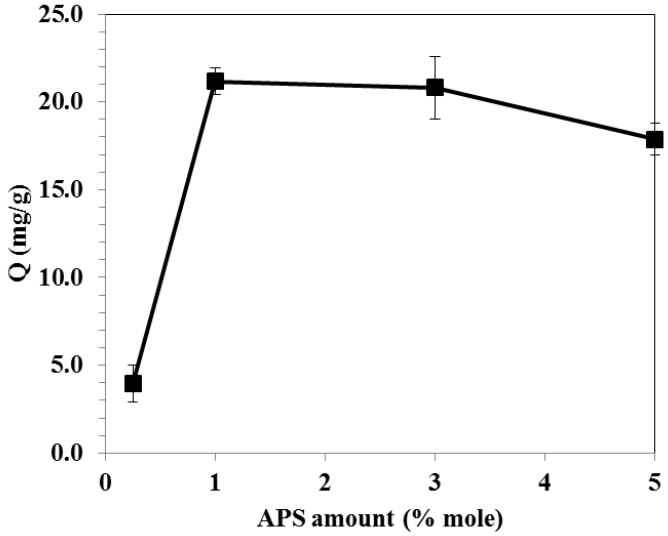

Figure 4.31 The As(V) adsorption amount of pAPTMA/bentonite composites at various APS concentrations.

4.2.1.3 Effect of Na-bentonite concentration

All XRD patterns of the nanocomposites (Figure 4.32) show the shift of (001) peaks of bentonite to larger d-spacings as compared to the d-spacing of Na-bentonite. The d-spacing of nanocomposites are summarized in Figure 4.33. For the composites with Na-bentonite concentration of 4-25 %wt, the d_{001} peak shifted to lower 2 theta values, suggested that the composites were intercalated nanocomposites. For the composites with 36-47 %wt Na-bentonite, two d_{001} peaks of bentonite were observed. The first peak at around 6 degree belonged to d_{001} peak of Na-bentonite. The second peak at around 4.2 degree could be referred to d_{001} peak of intercalated bentonite. For the composites with Na-bentonite concentration of 47 %wt, only one (001) peak at around 6 degree which belonged to d_{001} peak of Na-bentonite was observed. In conclusion, the amount of bentonite should not be higher than 25 %wt in order to obtain the pure phase of nanocomposites.

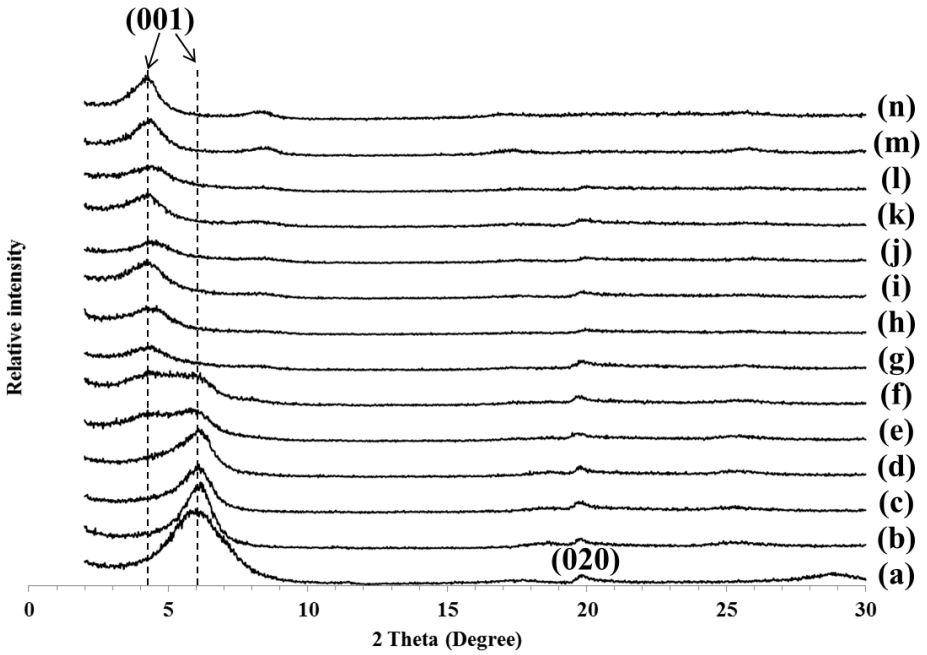

Figure 4.32 XRD patterns of pAPTMA/bentonite composites of (a) Na-bentonite (b) 1C0.5A76B, (c) 1C0.5A67B, (d) 1C0.5A57B, (e) 1C0.5A47B, (f) 1C0.5A36B, (g) 1C0.5A25B, (h) 11C0.5A22B, (i) 1C0.5A19B, (j) 1C0.5A16B, (k) 1C0.5A13B, (l) 1C0.5A10B, (m) 1C0.5A7B and (n) 1C0.5A4B.

The As(V) adsorption amount of the composites decreased with increasing Na-bentonite concentration (Figure 4.33). Apparently it was due to the low adsorption capacity of bentonite. According to the basis that the bentonite acted as the supporter for the dispersion of pAPTMA polycation and held the composites into a solid phase, therefore, the decreasing of adsorption amount upon the increasing of the Na-bentonite concentration resulted from the decreasing of the pAPTMA polycation amount

In order to compare the effect of Na-bentonite amount, the adsorption amounts per weight of polymer were calculated and shown in Figure 4.33. The As(V) adsorption amount per weight of polymer reached the maximum value of 14.6 mg/g Polymer with the Na-bentonite amount of 10 %wt. Comparing with the bulk polymer, all calculated As(V) adsorption amount per weight of polymer are very low. Therefore, the pAPTMA/bentonite composites prepared through *in situ* intercalative polymerization technique were not considered for further studied.

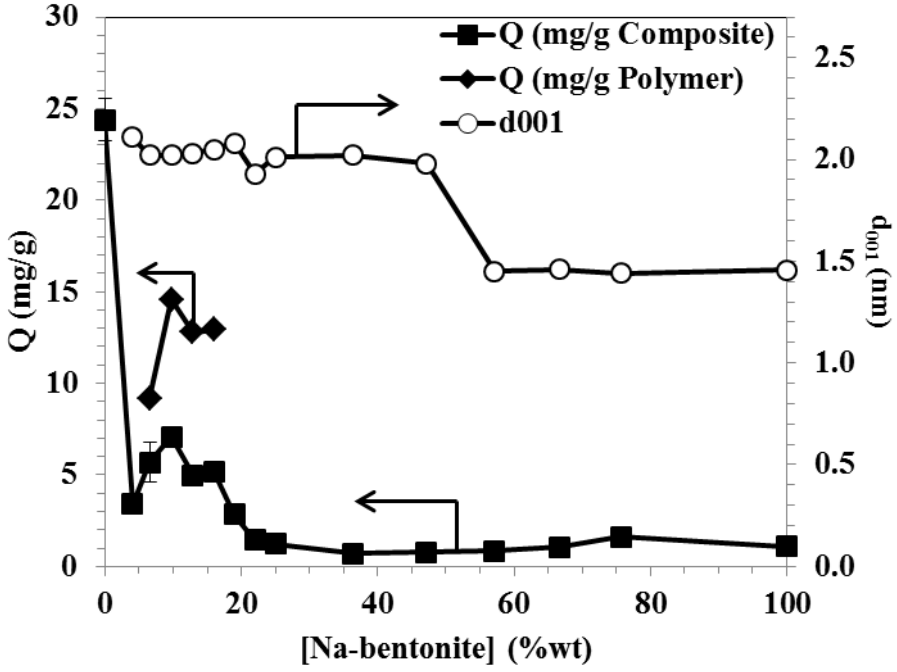

Figure 4.33 The As(V) adsorption amount and d001 of pAPTMACl/bentonite composites at various Na-bentonite concentration.

According to all studied parameters, the optimum condition for the pAPTMA/bentonite nanocomposite prepared through *in situ* intercalative polymerization method is that:
The weight ratio of Na-bentonite : APTMA-Cl monomer = 10:90,
MBA cross-linker concentration = 3 % mole (base on APTMA-Cl monomer),
APS initiator concentration = 3 % mole (base on APTMA-Cl monomer),
and Na-bentonite concentration = 10 % wt (base on APTMA-Cl monomer).

Comparing with solution intercalation method, the nanocomposites produced by *in-situ* intercalative polymerization method gave lower As(V) adsorption amount and the adsorption test of these nanocomposites might not be accurate and difficult to handle due to the hygroscopic nature of the polymer.

4.2.2 Poly([2-(acryloyloxy)ethyl]trimethylammonium chloride)

4.2.2.1 Effect of cross-linker concentration

This section used [2-(acryloyloxy)ethyl]trimethylammonium chloride (AETMA-Cl) as monomer. The concentration of MBA cross-linker was varied from 0-5 % mole while the weight ratio of Na-bentonite and AETMA-Cl monomer was fixed at 7.5:92.5, the molar ratio of TEMED and APS over the AETMA-Cl monomer was fixed at 1:100 and 0.5:100, respectively.

The FTIR spectra of Na-bentonite, pAETMA/bent composite (3C0.5A7.5B) and pAETMA-Cl are shown in Figure 4.34. The characteristic peaks of Na-bentonite appear at 3627 cm^{-1} (X – OH, X = Al, Mg), 3441 cm^{-1}, 1644 cm^{-1} (H – O – H) and 1034 cm^{-1} ($Si(Al)O_4$) [36, 124, 125]. The FTIR spectrum of pAETMA-Cl in Figure 4.34 (c) shows the characteristic peaks at 3429 cm^{-1} (– N – R_3), 1735 cm^{-1} (C = O) and 1168 cm^{-1} (R – O – R) [71]. The FTIR spectrum of composite (3C0.5A7.5B) contains both the characteristic peaks of Na-bentonite and pAETMA-Cl. The results suggested that the composite was composed of both bentonite and pAETMA-Cl. The FTIR spectra of the other composites show the same result with 3C0.5A7.5B. The characteristic absorption bands for all peaks were summarized in Table 4.5.

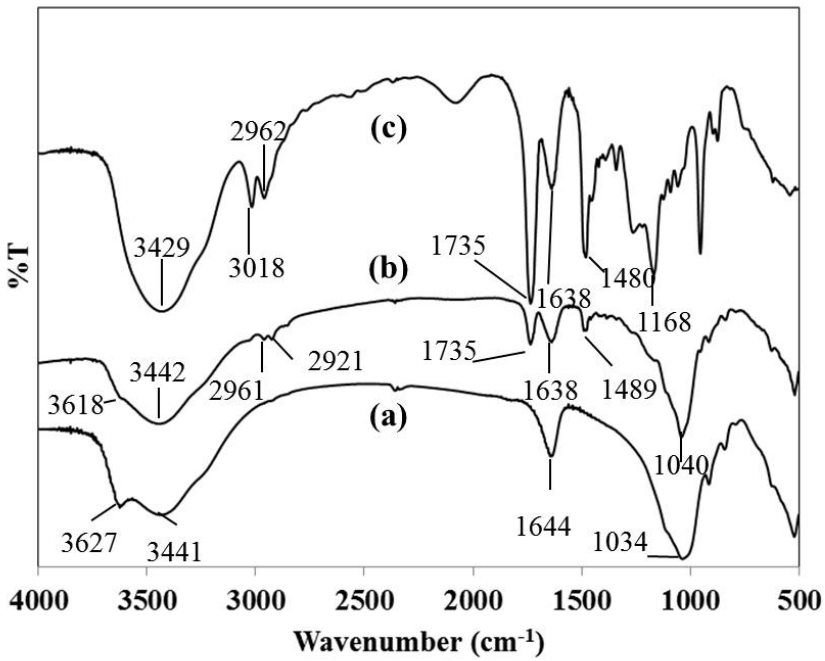

Figure 4.34 FTIR spectra of (a) Na-bentonite, (b) 3C0.5A7.5B and (c) pAETMA-Cl.

Table 4.5 FTIR spectral assignments of Na-bentonite, 3C0.5A7.5B and pAETMA-Cl

Band assignments	Na-bentonite (cm^{-1})	3C0.5A7.5B (cm^{-1})	pAETMA-Cl (cm^{-1})
ν(X – O – H), X = Al, Mg[a]	3627	3618	-
ν(H – O – H)[a]	3441	3442	3429
δ(H – O – H)[a]	1644	1638	1638
ν(Si – O)[a]	1034	1040	-
δ(Al – Al – OH)[a]	914	NA	-
δ(Al – Mg– OH)[a]	835	835	-
δ(Al – O – Si)[a]	521	519	-
δ(Si – O – Si)[a]	466	466	-
(– N – R_3)[b]	-	3418	3429
ν(CH_3) or ν(– CH_2 –)[b]		3030, 2961	3018, 2962
δ(– $N^+(CH_3)_3$[b]	-	1489	1480
δ(– CH_2 –)[b]	-	1489	1480
ν(C = O)[b]	-	1735	1735
(R – O – R)[b]	-	NA	1168

ν = stretching, δ = bending, [a]data from [36, 124, 125], [b]data from [71, 133-135], NA = not available

All XRD patterns of the nanocomposites (Figure 4.35) shows the shift of (001) peaks of bentonite to larger d-spacings (1.43 $\pm$ 0.01 nm) as compared to the d-spacing of Na-bentonite (1.38 nm) while the d-spacing of (020) peak do not change. It can be described in similar way to section 4.1.1.1. The results suggested that pAETMA found by FTIR could indeed intercalate into the layers of bentonite and expanded its d-spacing of bentonite. Therefore, it suggests that the obtained products are intercalated nanocomposites.

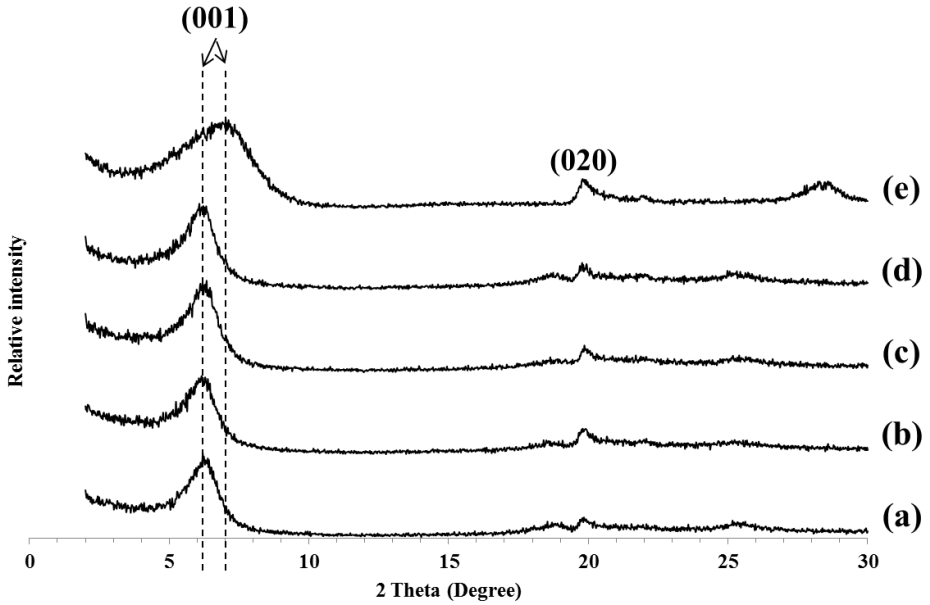

Figure 4.35 XRD patterns of pAETMA/bentonite composites of (a) 0C0.5A7.5B, (b) 1C0.5A7.5B, (c) 3C0.5A7.5B, (d) 5C0.5A7.5B and (e) Na-bentonite.

The amount of polymer in nanocomposites was estimated using TGA. As shown in Figure 4.36, the characteristic weight loss of the nanocomposites could be predicted as the combination of the individual components. The characteristic loss of intercalated pEPTMA appeared as that of the bulk pAETMA-Cl, except that the decomposition temperature would not be the sharp cut due to the confined space between bentonite layers trapping the decomposition products. The calculation of polymer amount in the composites was based on that the weight loss in each temperature range is the combination of the weight loss due to water, polymer and bentonite. Therefore weight loss of composites was divided into three steps and could be explained similar to section 4.1.2.1.

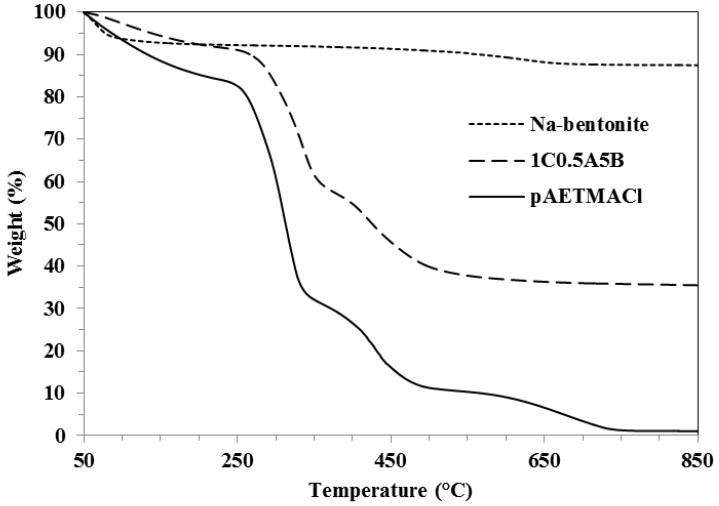

Figure 4.36 The TGA graphs of Na-bentonite (- - -), pAETMA-Cl (—), and pAETMA/bentonite composites (– – –).

The As(V) adsorption of the composites (Figure 4.37) shows the slightly increase of the adsorption as the amount of cross-linker increased. However, the large error bar at indicates the irreproducible results because of the uncontrollable synthesis.

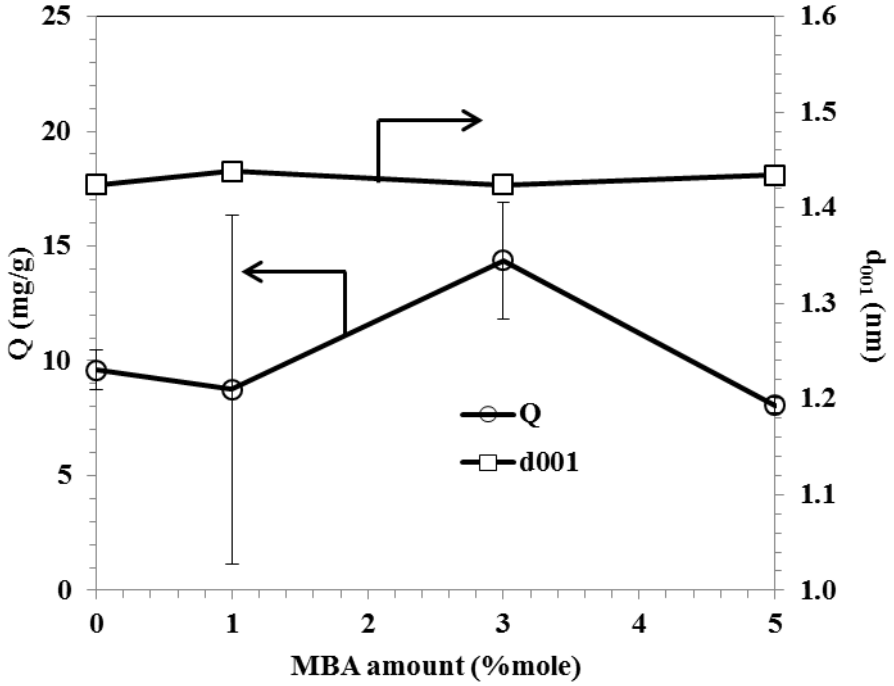

Figure 4.37 The d_{001} spacings and As(V) adsorption amounts with varied MBA concentrations.

4.2.2.2 Effect of Initiator concentration

The effect of APS initiator concentration was studied by varying the molar ratio of APS initiator concentration over AETMA-Cl monomer (0.5-5 %mole), while the weight ratio of Na-bentonite and AETMA-Cl monomer was fixed at 10:90, the molar ratio of TEMED and MBA over the AETMA-Cl monomer was fixed at 1:100 and 3:100, respectively.

All XRD patterns of the nanocomposites (Figure 4.38) shows the shift of (001) peaks of bentonite to larger d-spacings (1.43 $\pm$ 0.04 nm) as compared to the d-spacing of Na-bentonite (1.38 nm) while the (020) peak do not change. Therefore, it suggested that the obtained products were intercalated nanocomposites.

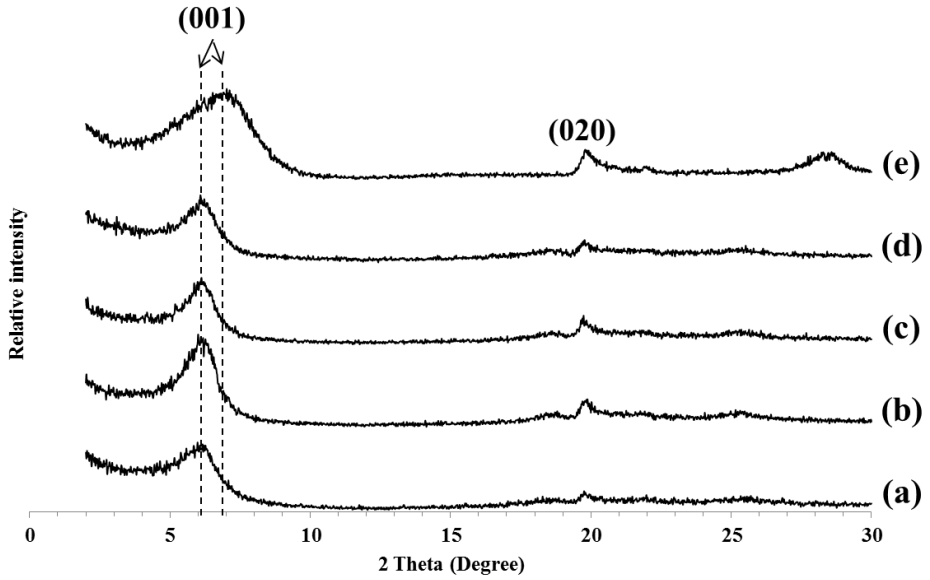

Figure 4.38 XRD patterns of pAETMACl/bentonite composites of (a) 3C0.5A7.5B, (b) 3C1A7.5B, (c) 3C3A7.5B, (d) 3C5A7.5B and (e) Na-bentonite

The As(V) adsorption decreased with increasing the APS concentration as shown in Figure 4.39. The maximum As(V) adsorption amount obtained from that using 0.5 % mole, therefore, the condition was selected for further studies.

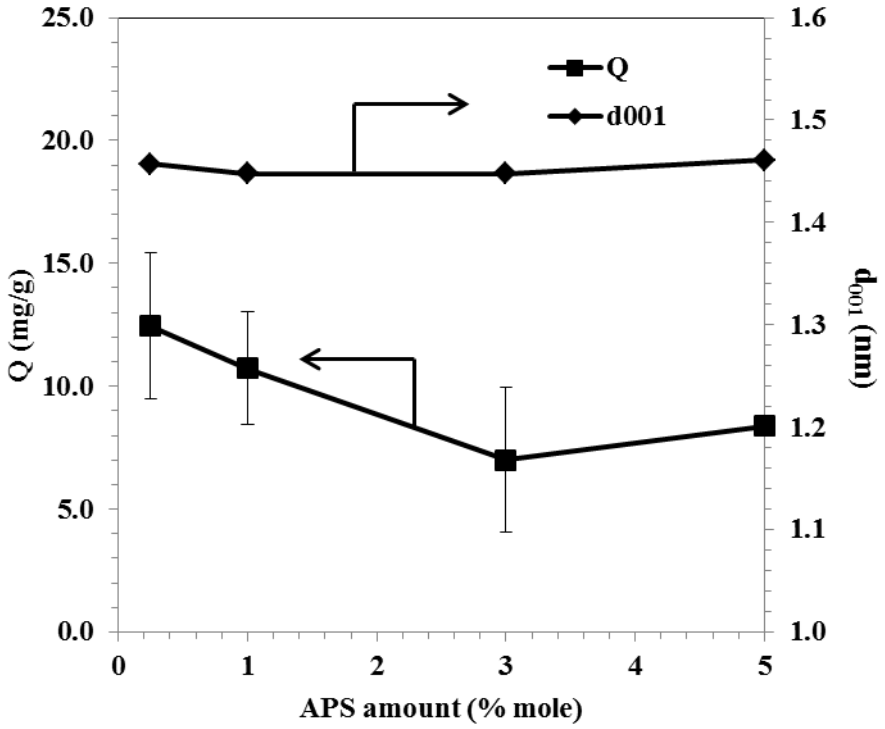

Figure 4.39 The As(V) adsorption amount of pAETMA/bentonite composites at various APS concentrations.

4.2.2.3 Effect of Na-bentonite concentration

All XRD patterns of the nanocomposites (Figure 4.40) shows the shift of (001) peaks of bentonite to larger d-spacings as compared to the d-spacing of Na-bentonite. The d-spacing of nanocomposites were summarized in Figure 4.41. For the composites with Na-bentonite concentration of 5 %wt, the d_{001} peak of bentonite disappeared suggested that the composites were exfoliated nanocomposites. For the composite with 7.5-25 %wt of Na-bentonite, the (001) peaks of bentonite shifted to larger d-spacings as compared to the d-spacing of Na-bentonite. Similar to the previous section (4.1.1.1), the expansion of d-spacing was due to the intercalation of polymer cations into the layers of bentonite. The results suggested that the product were intercalated nanocomposites.

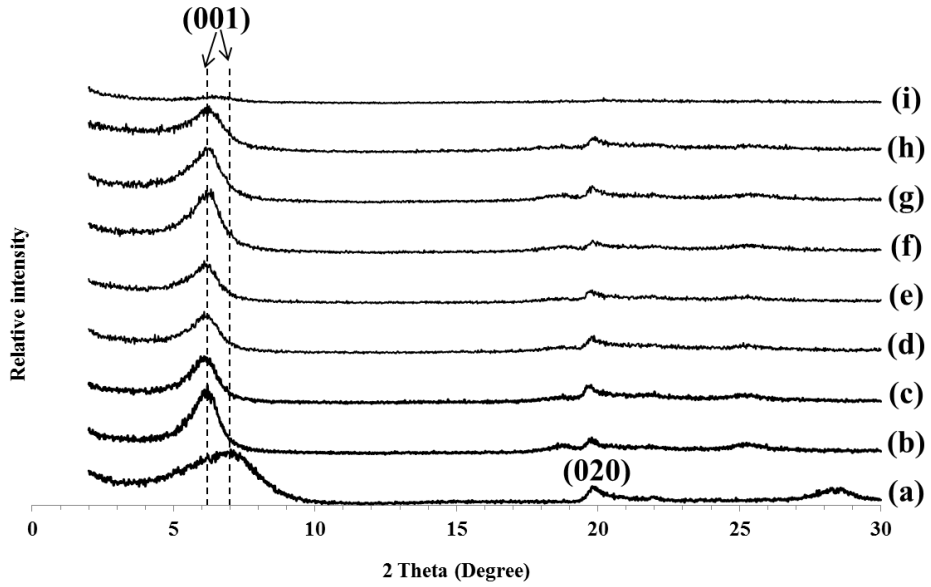

Figure 4.40 XRD patterns of pAPTMA/bentonite composites of (a) Na-bentonite (b) 1C0.5A22.5B, (c) 1C0.5A20B, (d) 1C0.5A17.5B, (e) 1C0.5A15B, (f) 1C0.5A12.5B, (g) 1C0.5A10B, (h) 11C0.5A7.5B and (i) 1C0.5A5B.

The As(V) adsorption amount of the composites decreased with increasing the Na-bentonite concentration (Figure 4.41). Apparently it was due to the low adsorption capacity of bentonite. According to the basis that the bentonite acted as the supporter for the dispersion of pAETMA polycation and held the composites into a solid phase, therefore, the decreasing of adsorption amount upon the increasing of the Na-bentonite concentration resulted from the decreasing of the pAETMA polycation amount.

In order to compare the effect of Na-bentonite amount, the adsorption amounts per weight of polymer were calculated and shown in Figure 4.41**.** The As(V) adsorption amount per weight of polymer reached the maximum value of 41.6 mg/g polymer with the Na-bentonite amount of 5 %wt. This value lower than that obtained from the solution intercalation method (46.2 mg/g polymer), therefore, the pAETMA/bentonite composites from this technique was not chosen for further studies.

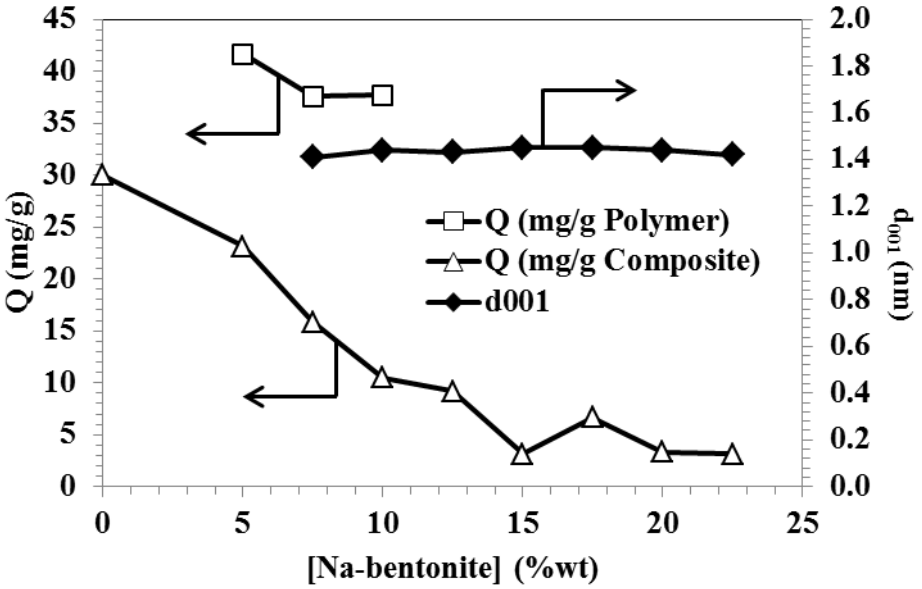

Figure 4.41 The As(V) adsorption amount and d_{001} of pAETMA/bentonite composites at various Na-bentonite concentrations.

According to all studied parameters, it can be concluded that the optimized condition for the pAETMA/bentonite nanocomposite prepared via *in situ* intercalative polymerization method is that preparing by using the weight ratio of Na-bentonite:AETMA-Cl monomer of 7.5:92.5, the MBA cross-linker of 3 % mole, and the APS initiator concentration of 0.5 % mole.

4.3 Comparison of the As(V) adsorption performance for the composite from different polymers and synthesis routes

The composites that showed the best performances from each synthesis method and each polymer are summarized in Table 4.6. Comparing between two methods, the composites prepared through the solution intercalation method provided higher the As(V) adsorption amount than the ones prepared from the *in situ* intercalative polymerization. Nanocomposites from both methods provided a similar

percent yield of polymers at lower Na-bentonite concentration. At high Na-bentonite concentration, the nanocomposites prepared by the solution intercalation method provided higher percent yield of polymers.

Comparing with bulk polymers, the nanocomposites, except APIS composites, possessed higher As(V) adsorption amount. The problem of handling of gel-like adsorbent in aqueous system in APIS discourages further investigation. Therefore, the composites produced by the solution intercalation method (named as APSI and AESI for pAPTMA/bentonite and pAPTMA/bentonite nanocomposites, respectively) were chosen for studied their As(V) adsorption behavior.

Table 4.6 Polymer/bentonite composites with the best performances from each methods.

Samples	Type of monomers	Methods	Abbreviation	Q		Polymer amount (%wt)
				mg/g Composite	mg/g Polymer	
15M1C2A30B	APTMA-Cl	**SI**	APSI	15.1	47.7	31.6
10M1C0.5A40B	AETMA-Cl	**SI**	AESI	12.2	46.2	26.4
1C0.5A10B	APTMA-Cl	**IS**	APIS	7.1	14.6*	48.7
1C0.5A5B	AETMA-Cl	**IS**	AEIS	23.1	41.6	55.5
pAPTMA-Cl	APTMA-Cl	-	-	-	24.4	100
pAPTMA-Cl	APTMA-Cl	-	-	-	33.2**	100
pAETMA-Cl	AETMA-Cl	-	-	-	30.0	100

SI= Solution intercalation, **IS** = *In situ* intercalative polymerization

*The gel-like products

**Calculated from ref. [49]

4.4 Optimization of As(V) adsorption parameters of polymer/bentonite nanocomposites

4.4.1 Effect of an adsorbent dose

The effect of 15M1C2A30B nanocomposite (APSI) and 10M1C0.5A40B nanocomposite (AESI) dosages on the As(V) removal was studied and shown in Figure 4.42. For both nanocomposites, the As(V) removal efficiency increased and the As(V) adsorption amount decreased with increasing the sorbent dosage. Starting from the dosages of 3 g/L, the removal efficiency slightly increased, but the adsorption amount got lower significantly. Therefore, the dosage of 3 g/L would be used for further studies.

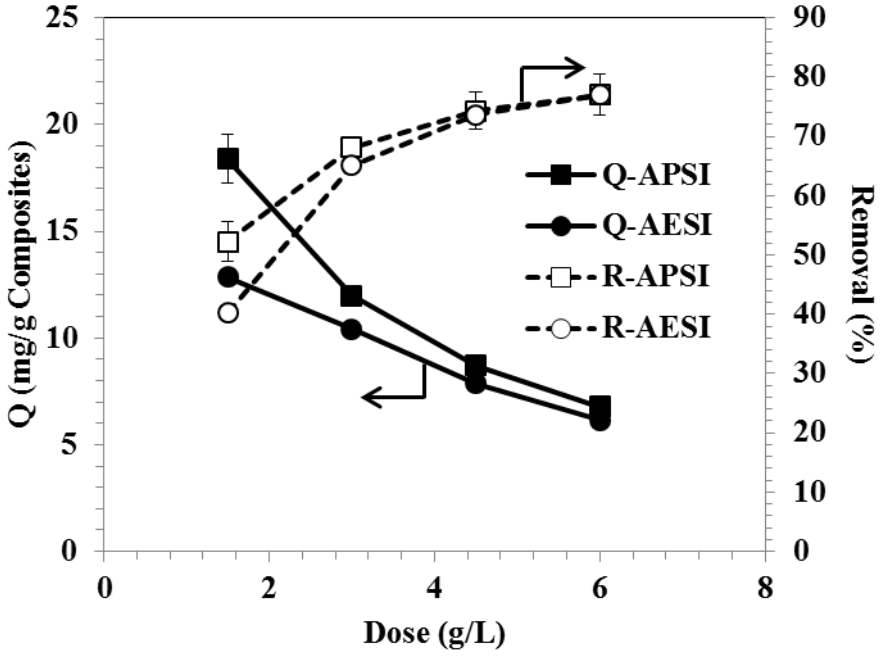

Figure 4.42 The As(V) removals from aqueous solution at various dosages using 15M1C2A30B (APSI) and 10M1C0.5A40B (AESI) nanocomposite. (C_0 = 50 mg/L, the contact time = 24 hour)

4.4.2 Effect of contact time

The effect of contact time on the As(V) adsorption amount using 15M1C2A30B nanocomposite (APSI) and 10M1C0.5A40B nanocomposite (AESI) are demonstrated in Figure 4.43. The adsorption occurred quickly and reached an equilibrium within 5 min for both nonocomposites. Compare to the As(V) adsorption result (360 min for bulk pAPTMA-Cl) of the bulk polymer from the previous report [49], these two nanocomposites showed faster treatment time (approximately 5 min). The reason was that, for the nanocomposites, As(V) adsorption onto polymer cations was facilitated by bentonite which acted as a supporter and dispersed the polymer cations.

The study of adsorption kinetics provides valuable insights into the mechanism of the reactions. There are three steps that normally control any adsorption process that could apply to this work: (i) the transportation of the solute from bulk solution to the film surrounding the adsorbent (Figure 4.44), (ii) from the transportation from an external surface to the an internal surface (the active site) (Figure 4.45), and (iii) the interaction between solute and an active site (in this case, chemisorption between the metal ions and cationic ends of polymer) (Figure 4.46). The slowest of these steps determines the overall rate of the adsorption process. Usually it is thought that the step (ii) leads to active surface and the step (iii) leads to intra-particle adsorption [118]. Several kinetic models have been used to explain the mechanism of the adsorption processes.

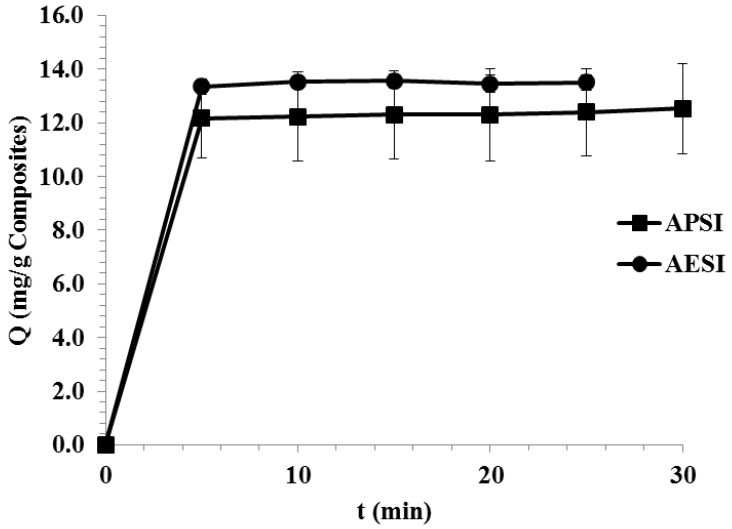

Figure 4.43 The effect of contact time on As(V) adsorption onto 15M1C2A30B composite(APSI) and 10M1C0.5A40B composite(AESI).

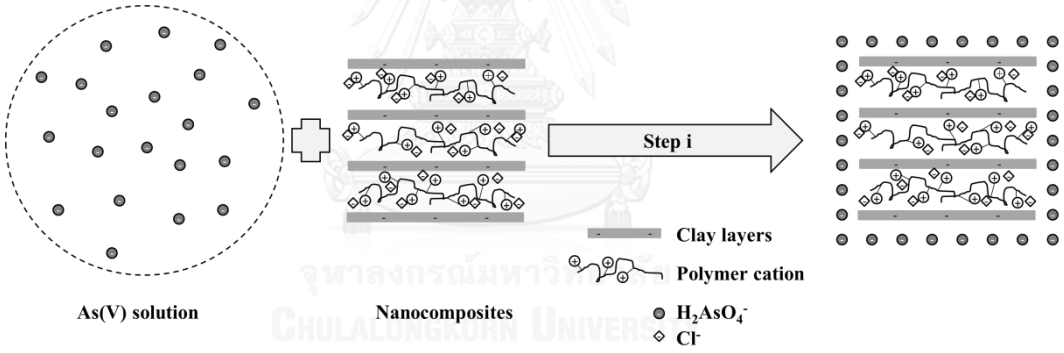

Figure 4.44 Schematic of the sorption mechanism step i, showing the transportation of the solute from bulk solution to the film surrounding the adsorbent.

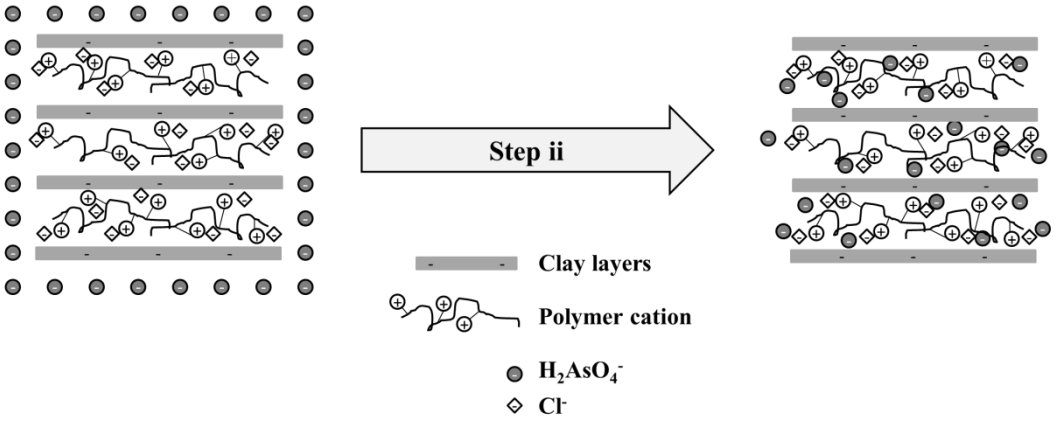

Figure 4.45 Schematic of the sorption mechanism step ii, showing the transportation of the solute from the film to the adsorbent surface.

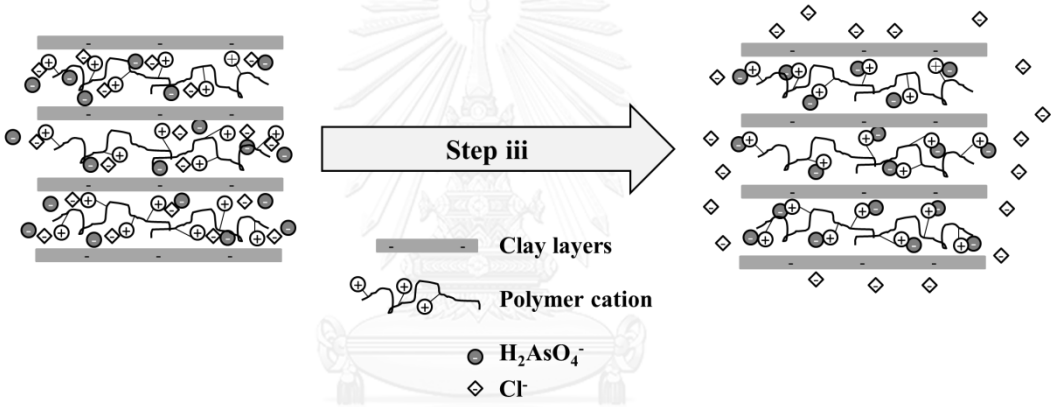

Figure 4.46 Schematic of the proposed sorption mechanism step iii, showing the As(V) adsorption onto the nanocomposites.

In this report, a simple pseudo-first and second-order kinetic models were employed. The linear plot between log (Q_e –Q_t) and t of the pseudo-first kinetic model was depicted in Figure 4.47 (a) and Figure 4.48 (a) for APSI and AESI, respectively. The values of Q_e and k_1 were calculated from the intercept and slope, respectively. While the linear plot between t/Q_t and t of the pseudo-second kinetic model was depicted in Figure 4.47 (b) and Figure 4.48 (b) for APSI and AESI, respectively. The values of Q_e and k_2 were calculated from the slope and intercept, respectively. The fitting parameters of kinetic studies for the As(V) adsorption on APSI and AESI by those two models were presented in Table 4.7. It can be seen that the correlation coefficients R^2 obtained from the pseudo second-order kinetic model

(0.9998 for APSI and 1.000 for AESI) were closer to 1.000 than those from the pseudo first-order kinetic model (0.9345 for APSI and 0.2048 for AESI), which suggested that the pseudo second-order kinetic model was suitable to describe the As(V) adsorption onto both 15M1C2A30B nanocomposite (APSI) and 10M1C0.5A40B nanocomposite (AESI). Additionally the calculated adsorption capacities (Q_e) from the pseudo second-order kinetic model for both nanocomposites were significantly close to the experimental values ($Q_{e,exp}$). Because the pseudo-second-order rate equation was based on the assumption that the rate-limiting step may be chemisorption [113, 117, 136]. Therefore, it was reasonable to assume that the rate-determining step in this work for this adsorption process might be chemisorption involving the anions exchange between arsenate anion in solution and chloride anion at polymer chain, corresponding with the step (iii) as described above.

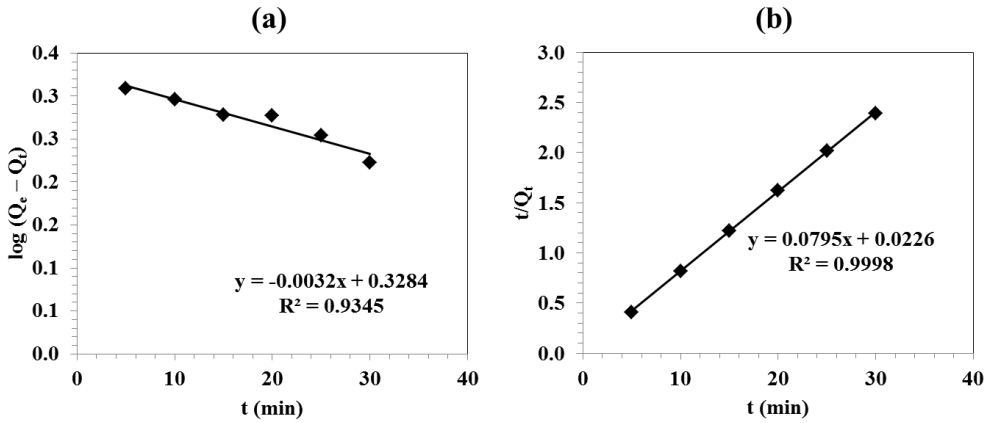

Figure 4.47 Linear plots of (a) pseudo-first-order kinetic model and (b) pseudo-second-order kinetic model of 15M1C2A30B nanocomposite (APSI).

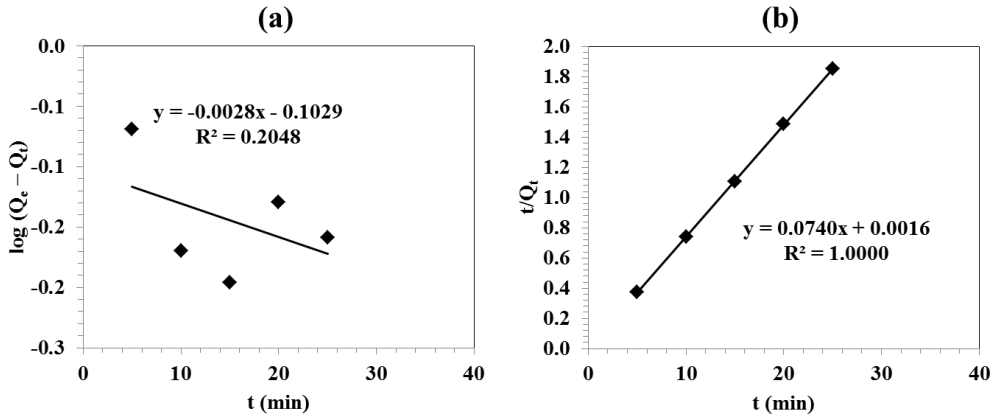

Figure 4.48 Linear plots of (a) pseudo-first-order kinetic model and (b) pseudo-second-order kinetic model of 10M1C0.5A40B nanocomposite (AESI).

Table 4.7 Adsorption kinetic parameters of As(V) adsorption onto 15M1C2A30B nanocomposites.

Materials	$Q_{e,exp}$ (mg/g)	Pseudo-first-order kinetic			Pseudo-second-order kinetic		
		k_1 (min^{-1})	Q_e (mg/g)	R^2	k_2 (g mg^{-1} in^{-1})	Q_e (mg/g)	R^2
APSI	12.5	0.00735	2.13	0.9345	0.280	12.6	0.9998
AESI	13.5	0.00638	0.79	0.2048	3.42	13.5	1.000

C_0 = 50 mg/L, m = 0.03g, V = 10 mL, shaking speed = 30 rpm

Based on the pseudo-second order kinetic model, the purposed mechanism for the APSI and AESI nanocomposites was described as chemical reaction below.

$$BP\text{-}Cl + H_2AsO_4^- \Longleftrightarrow BP(H_2AsO_4) + Cl^- \quad (4.\ 2)$$

where BP-Cl is polar site on the polymer ($RN(CH_3)_3^+Cl^-$) of the APSI and AESI nanocomposites.

Since the pseudo-second order kinetic model is suitable to describe, the rate law for above reaction can be express as:

$$d(BP - Cl)_t/dt = k[(BP - Cl)_0 - (BP - Cl)_t]^2 \quad (4.\ 3)$$

where $(BP - Cl)_t$ is the number of active sites occupied on the sorbent at time t, $(BP - Cl)_0$ is the number of equilibrium sites available on the sorbent.

If the number of active sites occupied on the sorbent is proportional to the sorption capacity, the kinetic rate law can be rewritten as:

$t/Q_t = (t/Q_e) + 1/(k_2 Q_e^2)$ (4. 4)

where Q_e and Q_t (mg/g) are the capacities at equilibrium and at time t, respectively, and k is the pseudo second-order kinetic rate constant.

4.4.3 Effect of initial pH of arsenate solution

The effect of the initial As(V) solution pH on the As(V) removal efficiency was shown in Figure 4.49. Both APSI and AESI nanocomposites show a similar trend that As(V) adsorption amount increased with increasing the solution pH and then reached to the maximum at pH 9. This results agree with that reported by Barakat and Sahiner [49] for APSI and that reported by Rivas et al. [137] for AESI. According to the Eh-pH diagram for arsenic in Figure 1.1, the species of As(V) are dependent on the solution pH. The pK_a of As(V) is written below [2].

$H_3AsO_4 \rightarrow H^+ + H_2AsO_4^-$ ($pKa_1 = 2.1$) (4. 5)

$H_2AsO_4^- \rightarrow H^+ + HAsO_4^{2-}$ ($pKa_2 = 6.7$) (4. 6)

$HAsO_4^{2-} \rightarrow H^+ + AsO_4^{3-}$ ($pKa_3 = 11.2$) (4. 7)

From the Eh-pH diagram in Figure 1.1 the species of As(V) at pH between 7 to 9 should be divalent arsenate anion, $HAsO_4^{2-}$. Dambies [77] reported that the resins having quaternary ammonium groups connected to polymer matrix had more affinity for divalent anions than monovalent anions. Hence the behaviors of the nanocomposites that showed high As(V) adsorption amounts over the solution pH range of 7 to 9 could be predicted because of AP and AE contained quaternary ammonium groups. However, the As(V) adsorption amount dramatically decreased when the pH of the solution got higher than 9. This was due to the higher competitive OH^- anion concentration at higher pH solution. The effect of pH as high as 11 was less in APSI as compared with that of AESI, It might be that the adsorption of As(V) by APSI was stabilized by the rearrangement of the amide group at side chain of polymer as shown in Figure 4.50.

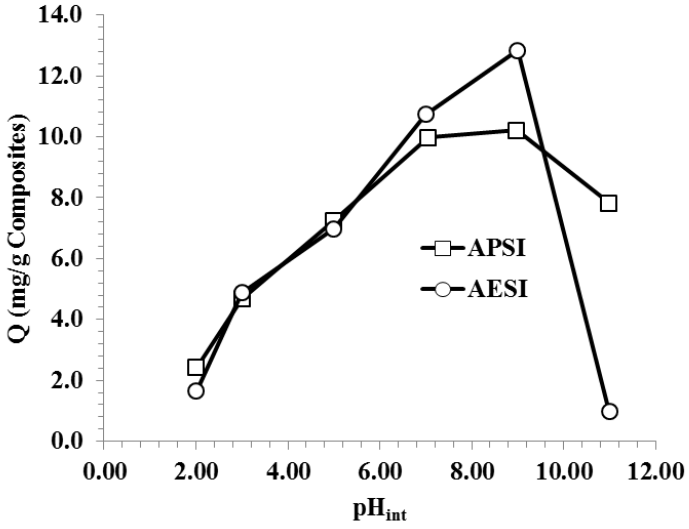

Figure 4.49 The adsorption of As(V) on nanocomposites in various pH. (C_0 = 50 mg/L, the contact time = 6 h)

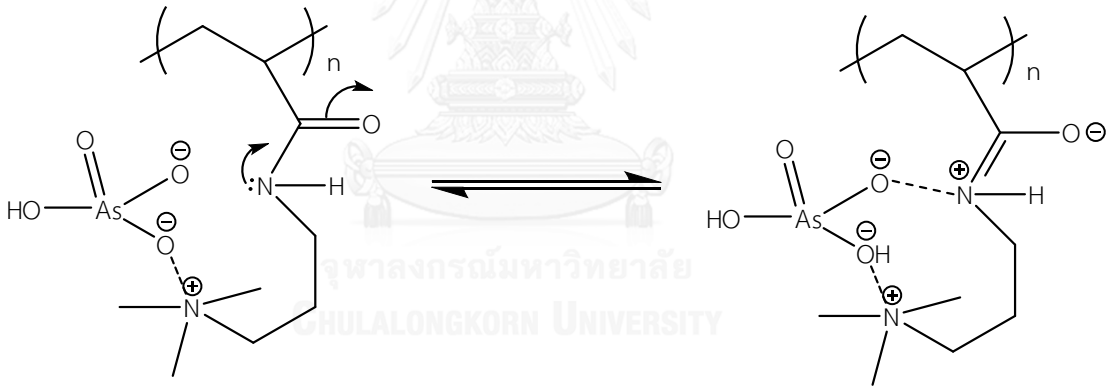

Figure 4.50 Schematic of the As(V) adsorption by APSI at pH =11.

4.4.4 Effect of initial concentration of arsenate

The equilibrium isotherms for the adsorption of As(V) onto APSI and AESI nanocomposite are presented in Figure 4.51. The As(V) adsorption amount increased with the increasing an equilibrium As(V) concentration. The steep slope at low C_{eq} and Q_e indicated that there were numerous readily adsorption sites at an initial stage. In order to obtain more information, the equilibrium adsorption data for AESI and APSI nanocomposites were fitted into the Langmuir and Freundlich isotherm models.

The Langmuir isotherm models describe a monolayer adsorption of sorbate onto the sorbent surface with homogeneous nature [114, 117]. The linear plots of Langmuir equation were depicted in Figure 4.52 (a) Figure 4.53 (a) for APSI and AESI, respectively. The Langmuir constant parameters were summarized in Table 4.8.

The assumption of Freundlich isotherm model is based on that the sorbate adsorbed onto the heterogeneous surface of sorbent [114, 115, 117]. The linear plots of Freundlich equation were depicted in Figure 4.52 (b) Figure 4.53 (b) and for APSI and AESI, respectively. The Langmuir constant parameters were summarized in Table 4.8.

For APSI nanocomposite, the Freundlich model has higher regression coefficient (R^2 = 0.9949) when compared to the Langmuir isotherm model (R^2 = 0.9778) suggesting an adsorption of As(V) on the heterogeneous surface of the APSI nanocomposites. In another word, there are more than one adsorption sites for As(V). First site is the positively charged (– NMe_3^+) of pAPTMA-Cl which could interact with the negatively charged As(V) species [70]. The second site is the amphoteric sites at the broken edges of bentonite layers which are mainly octahedral Al-OH and tetrahedral Si-OH groups [138-140]. These groups could be complexed with arsenic as shown below [138, 141, 142]:

$$–AlOH + H_2AsO_4^- \rightarrow –AlH_2AsO_4 + OH^- \quad (4.\ 8)$$

$$\text{or } 2(–AlOH) + HAsO_4^{2-} \rightarrow –Al_2HAsO_4 + 2OH^- \quad (4.\ 9)$$

The *n* value of 2.96 is larger than 1 suggests the favorable nature of adsorption [116, 119, 143]. It could be explained with the coulombic interaction of the positively charged (– NMe_3^+) with the negatively charged arsenate anion.

For the AESI nanocomposite, the experimental data fitted with both the Langmuir isotherm model (R^2 = 0.9880) and the Freundlich model (R^2 = 0.9797). Compared with the structure of pAPTMA-Cl, pAETMA-Cl contains the same positively charged (– NMe_3^+) active sites as shown in Figure 4.54. Therefore, the AESI nanocomposite is likely to possess similar active sites like the APSI nanocomposites; therefore, the Freundlich model is assumed here.

The *n* value of 4.21 is larger than 1 suggests the favorable nature of adsorption [116, 119, 143]. It could be explained with the coulombic interaction of the positively charged ($-NMe_3^+$) with the negatively charged arsenate anion.

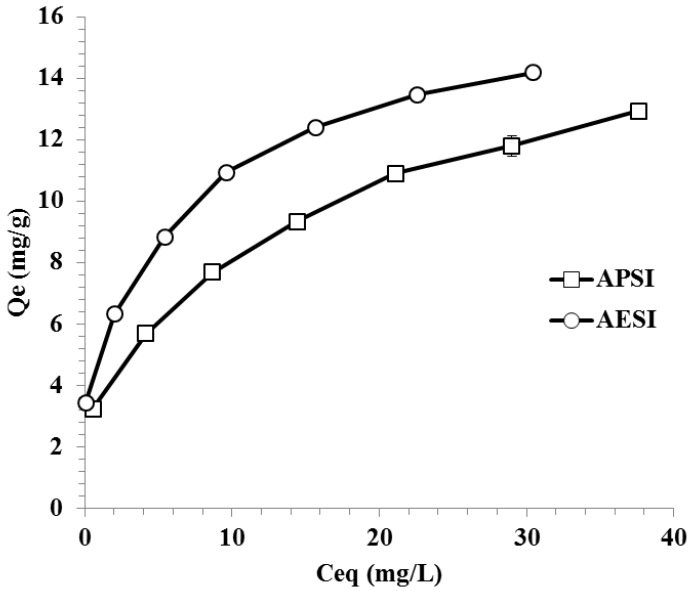

Figure 4.51 As(V) adsorption isotherm of APSI and AESI nanocomposites. (pH 9, the contact time = 6 hour)

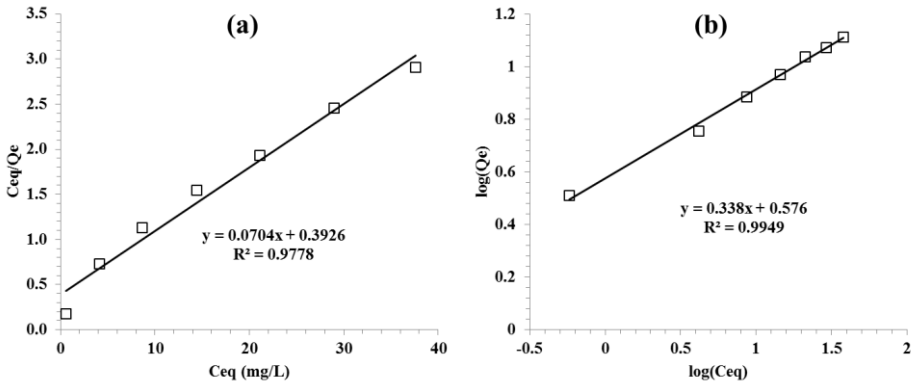

Figure 4.52 Langmuir isotherm plot (a) and Freundlich isotherm plot (b) of APSI nanocomposite.

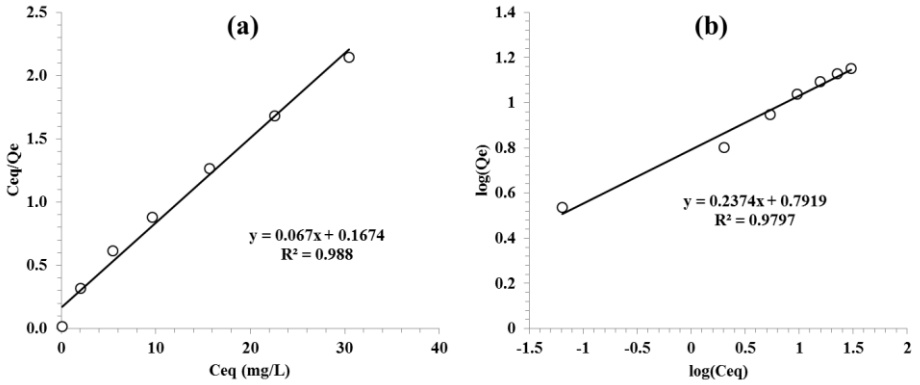

Figure 4.53 Langmuir isotherm plot (a) and Freundlich isotherm plot (b) of AESI nanocomposite.

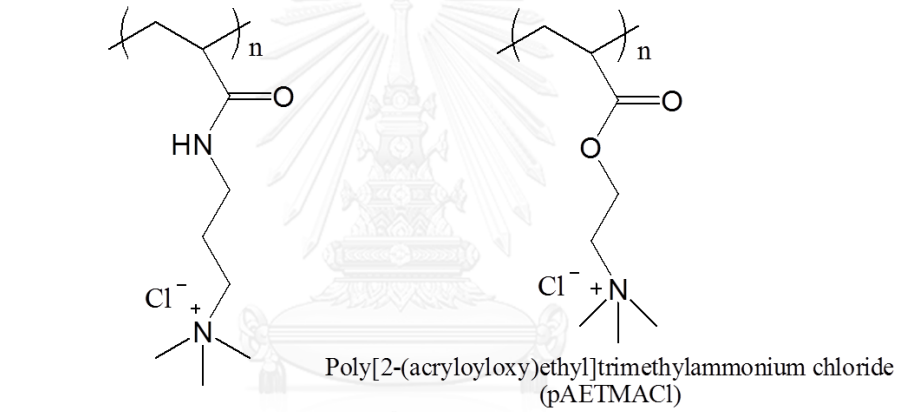

Figure 4.54 Schematic of the pAPTMA-Cl and pAETMA-Cl Structures.

Table 4.8 Isotherm parameters of As(V) adsorption onto the 15M1C2A30B nanocomposite(APSI) and 10M1C0.5A40B(AESI)

Materials	Langmuir isotherm model				Freundlich isotherm model		
	Q_m (mg/g)	K_L (L/mg)	R_L	R^2	K_F	n	R^2
APSI	14.2	0.18	0.07	0.978	3.77	2.96	0.995
AESI	14.9	0.40	0.03	0.988	6.19	4.21	0.980

m = 0.03 g, V = 10 mL, shaking speed = 30 rpm, time = 6 hour

4.4.5 Effect of interference anions

The adsorption of As(V) onto APSI and AESI nanocomposites was affected by the type and concentration of interference anions as shown in Figure 4.55 and Figure 4.56 for APSI and AESI, respectively. The order of the interfering effects was that $H_2PO_4^-$ ~ SO_4^{2-} > CO_3^{2-} > NO_3^- > Cl^- (at molar ratio lower than 10) and $H_2PO_4^-$ > SO_4^{2-} ~ CO_3^{2-} > NO_3^- > Cl^- (at molar ratio of 50) for both nanocomposites. The similarity resulted from having the quaternary ammonium as their active sites for As(V). It can be noticed that divalent anions could interfered the As(V) adsorption more than monovalent anions. In the case of $H_2PO_4^-$, at the solution pH of 9, the predominate species of phosphate became a divalent anion, HPO_4^{2-} [136].

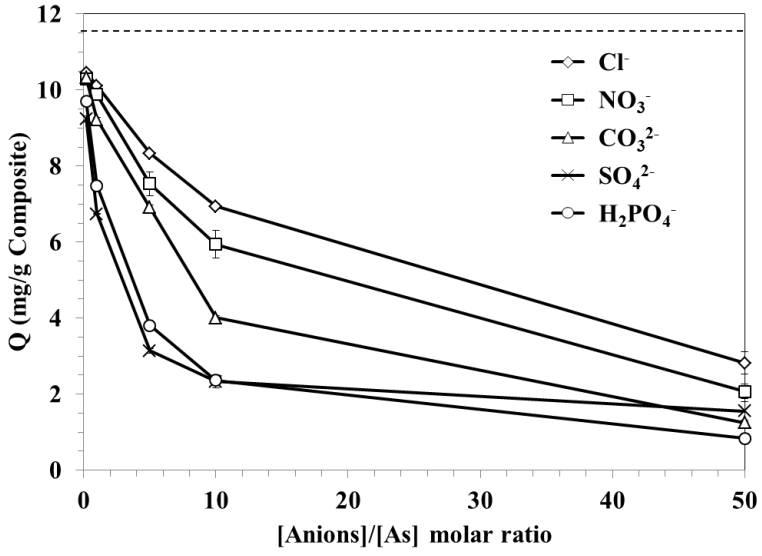

Figure 4.55 The As(V) adsorption on 15M1C2A30B composite (APSI) with difference competing anions. (C_0 = 50 mg/L, the contact time = 24 hour)

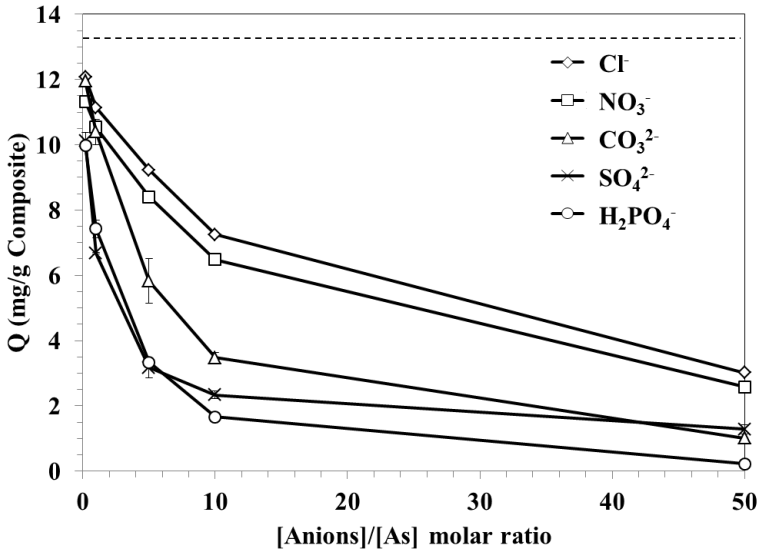

Figure 4.56 The As(V) adsorption on 10M1C0.5A40B composite (AESI) with difference competing anions. Dash line is the As(V) adsorption amount with no competing anion. (C_0 = 50 mg/L, the contact time = 24 hour)

4.6 Arsenic removals from real wastewater using polymer/bentonite nanocomposites

Two samples of wastewaters, TK80 and TK81, were obtained from the oil company in Thailand. The initial pH of TK80 and TK81 wastewaters are 7.68 and 2.66, respectively. Because the APSI and AESI nanocomposites performed well at pH of 9, therefore, the pH of TK80 and TK81 wastewaters were adjusted to 9 by adding 0.01, 0.1 and 1.0 M of NaOH and HNO_3. However, to comparison, the arsenic removals were conducted both in as received solution and in solution pH of 9. The precipitates occurred in both wastewaters during adjust the pH up to 9 and the arsenic concentrations decreased from 63.18 mg/L to 43.56 mg/L (31.1%) for TK80 and 82.4 mg/L to 49.35 mg/L (40.1%) for TK81. It might be that arsenic was adsorbed by other metal oxide that precipitated at high hydroxide level. Figure 4.57 shows the arsenic adsorption using APSI and AESI nanocomposites. Arsenic removal efficiency increased with increasing the sorbents dose for both TK80 and TK81 wastewaters. However, the values are very low due to interference anions in the wastewaters.

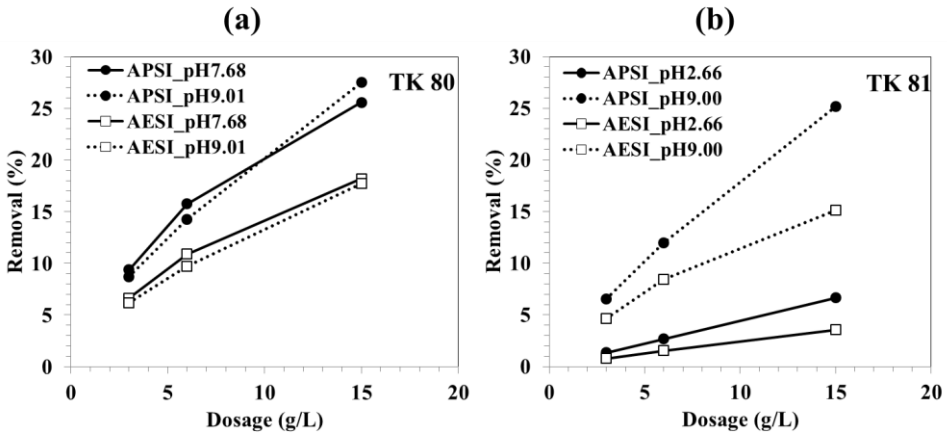

Figure 4.57 Arsenic removal from wastewater samples (a) TK80 and (b) TK81 using polymer/bentonite nanocomposites.

4.7 Synthesis and characterization of magnetic layered double hydroxide composite via coprecipitation method

In this part, another type of clay minerals, called as “anionic clay” or “layered double hydroxides (LDHs)”, was used as an adsorbent for arsenate or As(V) in which incorporated with magnetic particles to facilitate its separation from solution using an external magnetic field. The synthesis and characterization of the materials and their composite as well as its adsorption ability towards As(V) were studied.

4.7.1 Synthesis of Fe_3O_4

The XRD pattern of Fe_3O_4, shown in Figure 4.58 (a), was identified as that of the magnetite phase (PDF 88-0315). The diffraction peaks appearing at 30.32°, 35.58°, 43.28°, 53.66°, 57.22° and 63.02°, corresponded to d_{220}, d_{311}, d_{400}, d_{422}, d_{511} and d_{440}, respectively. In the synthesis of the magnetic/LDH composite, the calcination step was needed; therefore, the change of Fe_3O_4 phase upon the temperature was studied. The synthesized Fe_3O_4 was calcined at 450°C for 5h. After calcination, Fe_3O_4 transformed to the hematite phase (PDF 33-0664) (α-Fe_2O_3), as shown in Figure 4.58 (b). As a consequence of this phase change, the magnetic behavior of iron oxide phase vanished. The transformation of Fe_3O_4 to the hematite phase was also reported by Pati et al. [81]. This phase change occurred because

Fe_3O_4 contacted directly to oxygen in air at high temperature and formed the oxygen-rich product of α-Fe_2O_3. Moreover, the crystallinity of the calcined product was higher than that of Fe_3O_4, indicating the aggregation and crystal growth of iron oxides which was unpreferable for the use as an adsorbent. In this work, the magnetite particles would be covered thoroughly by LDH platelets in order to maintain the magnetic property and prevented the aggregation of iron oxide phase.

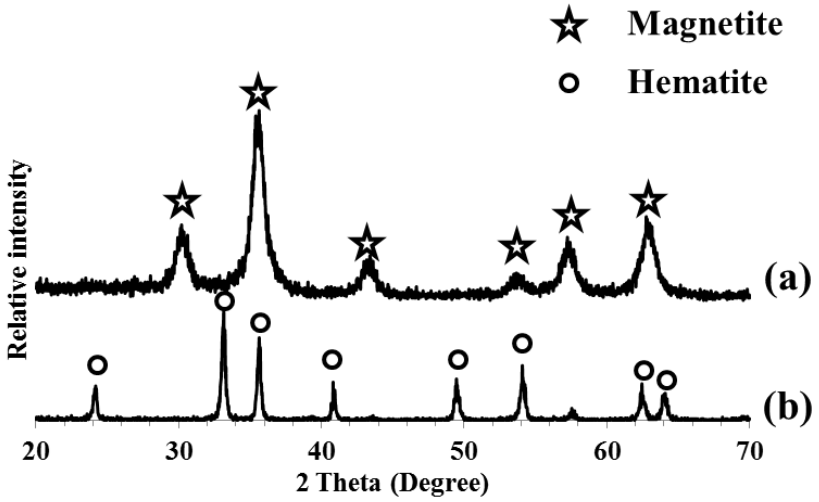

Figure 4.58 XRD patterns of (a) Fe_3O_4 and (b) cal-Fe_3O_4

4.7.2 Synthesis of $[Mg_{0.66}Fe_{0.33-x}Zr_x(OH)_2](CO_3)\delta$ (x = 0 – 0.33)

Figure 4.59 shows the XRD pattern of the as-synthesized Mg-Fe-Zr LDHs. All XRD patterns are identified as LDHs structure. This result similars to that reported by Chitrakar et al. [75], except for x = 0.33. The diffraction peaks at 2θ of 10.98°, 22.09°, 33.80°, 38.06° and 59.04° were identified as d_{003}, d_{006}, d_{009}/d_{012}, d_{015} and d_{110}, respectively [21, 42, 75, 144]. It can be noticed that the (001) peaks shows a little bit shift to lower 2θ value with increasing Zr amount. The shift of (110) peak suggests that the octahedral unit cell of LDHs which is the building block of Brucite-like sheet is expanded. The reason behind the shift is that the Fe^{3+} ion (ionic radius of 64.5 pm) located inside the octahedral unite cell is partially substituted by a larger Zr^{4+} ion (ionic radius of 72 pm) that lead to the increasing in *a* parameter upon the increasing

in Zr content (Figure 4.60 and Figure 4.61). Moreover, the peaks involve *l* parameter (d_{003} and d_{006}) shows a dramatically shift with increasing Zr amounts. The (00*l*) peaks are related to the basal spacing of LDHs. The shift of (00*l*) peaks in Figure 4.60 and Figure 4.61 suggests that the interlayer of LDHs is expanded. The reason behind the shift could be that increasing the Zr^{4+} content results to the higher positive charge of the brucite-like sheet and larger numbers of intercalated anions. For x = 0.33, the phase is no longer LDHs structure.

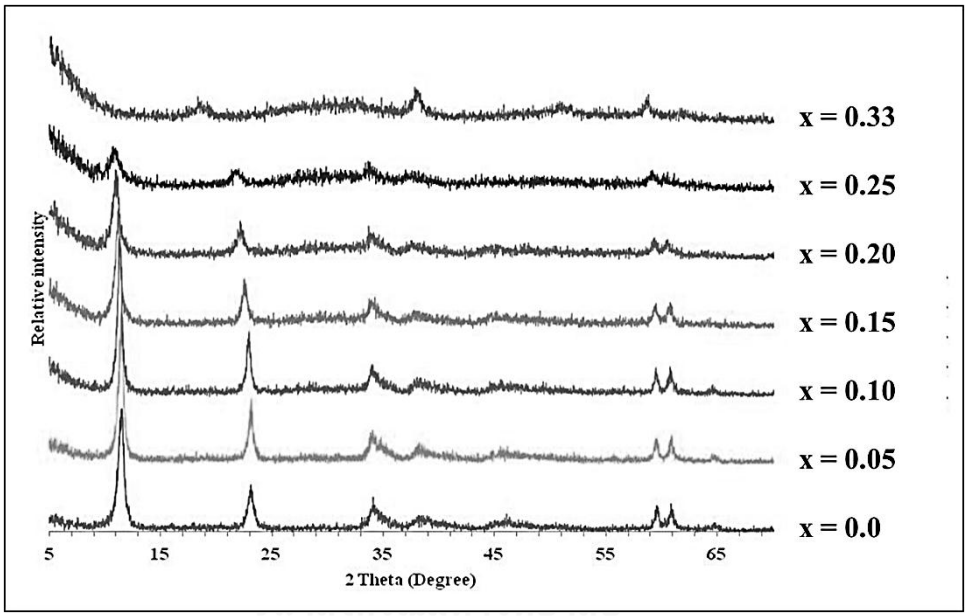

Figure 4.59 XRD patterns of $[Mg_{0.66}Fe_{0.33-x}Zr_x(OH)_2](CO_3)\delta$ (x = 0 – 0.33)

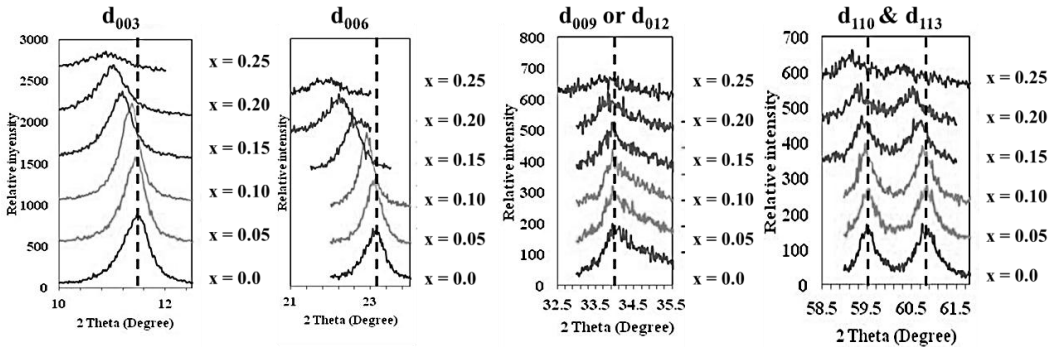

Figure 4.60 XRD patterns at various region of $[Mg_{0.66}Fe_{0.33-x}Zr_x(OH)_2](CO_3)\delta$ (x = 0 – 0.33)

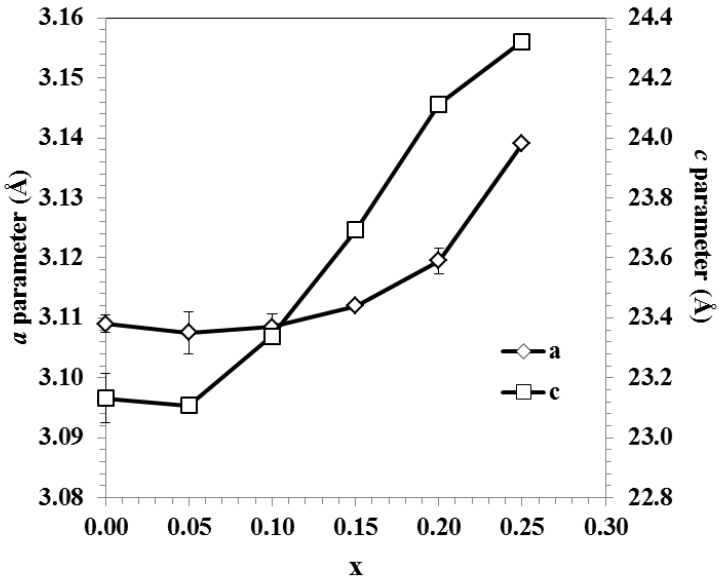

Figure 4.61 The unit cell parameters of $[Mg_{0.66}Fe_{0.33-x}Zr_x(OH)_2](CO_3)_{\delta}$ (x = 0 – 0.33)

The As(V) adsorption amounts increased upon increasing the Zr content as shown in Figure 4.62. Increasing Zr content in the Mg-Fe-Zr LDHs resulted in increasing the net positive charge of brucite-like sheet because the lower charge of Fe^{3+} ion is partially substituted by the higher charge of Zr^{4+} ion. Mg-Fe-Zr LDHs with x = 0.25 provided the highest As(V) adsorption amount with still retained the LDHs structure, therefore it was chosen for further study.

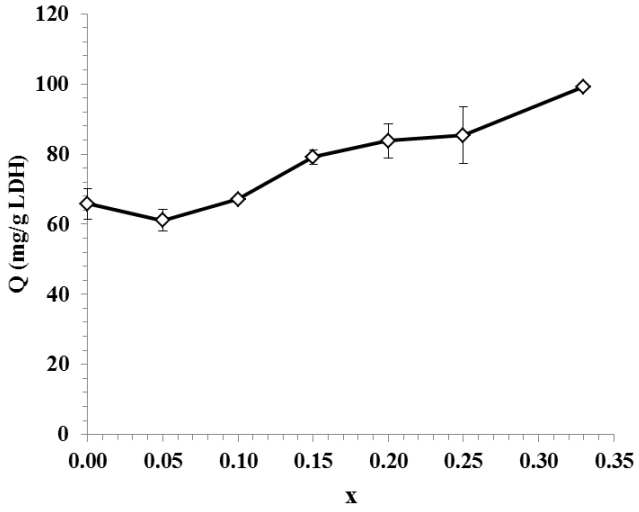

Figure 4.62 The As(V) adsorption amounts of $[Mg_{0.66}Fe_{0.33-x}Zr_x(OH)_2](CO_3)_{\delta}$ (x = 0 – 0.33). (C_0 = 150 ppm, pH = 6, shaking time = 18 h at 30 rpm)

4.7.3 Synthesis of Fe_3O_4/Mg-Fe-Zr LDH composite

The XRD pattern of the as-synthesized m-LDH composite is shown in Figure 4.63 (d). The pattern is comprised of two sets of characteristic reflection planes from the LDH (Figure 4.63 (c)) and Fe_3O_4 (Figure 4.63 (a)), with the typical peaks of the LDH at d_{003}, d_{006}, d_{009} and d_{110} and the five highest peaks of Fe_3O_4 at d_{220}, d_{311}, d_{400}, d_{511} and d_{440} being recognized. After calcination, the LDH transformed to mixed-metal oxide particles [42], as shown in Figure 4.63 (e), and it will be called as calcined LDH. For m-LDH, after calcination, the XRD pattern in Figure 4.63 (f) shows that m-LDH composite was comprised of two phases, Fe_3O_4 and the calcined LDH. Despite the fact that the bare Fe_3O_4 was transformed to α-Fe_2O_3 and lost its magnetic behavior after calcination, the Fe_3O_4 phase of the magnetic composite retained its structure after calcination. This result indirectly suggested that the Fe_3O_4 particles were well covered by the LDH platelets, therefore, the oxidation of Fe_3O_4 at the calcination temperature was prohibited. This was confirmed by both the TEM and SEM-EDX results. TEM analysis shows that the Fe_3O_4 particles were well dispersed and covered by the LDH (Figure 4.64) and mixed-metal oxide (Figure 4.65) in m-LDH and cm-LDH, respectively. In Figure 4.66, the SEM-EDX analysis of the cm-LDH composite shows the spread of the Mg, Fe and Zr elements over all particles. In particular, the strong signals of Mg and Zr over Fe indicate that the preformed Fe_3O_4 particles were covered by the LDH during the process of LDH precipitation.

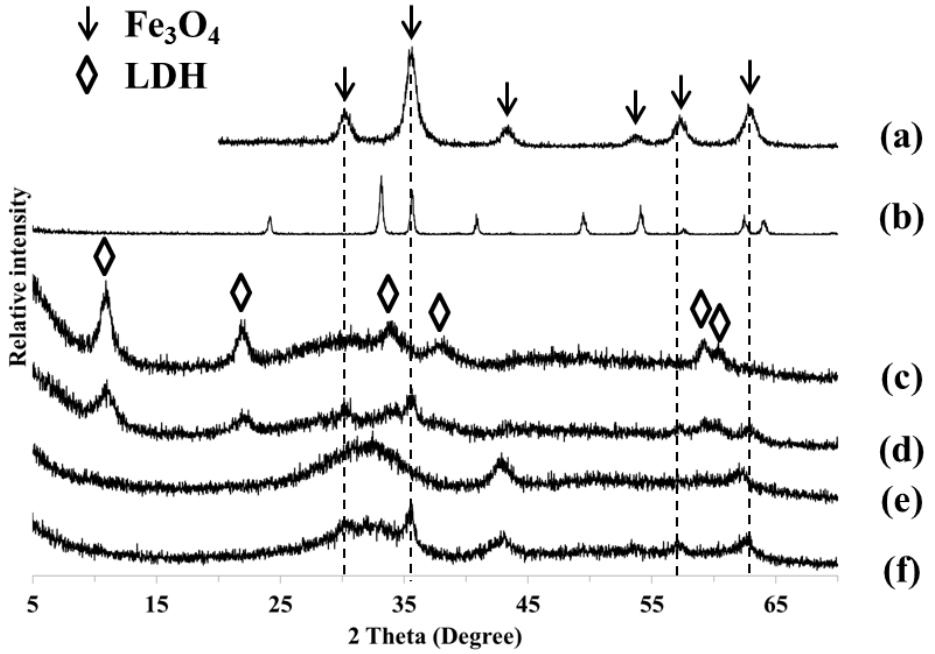

Figure 4.63 XRD patterns of (a) Fe_3O_4, (b) calcined Fe_3O_4, (c) LDH, (d) as-synthesized m-LDH composite, (e) c-LDH and (f) cm-LDH.

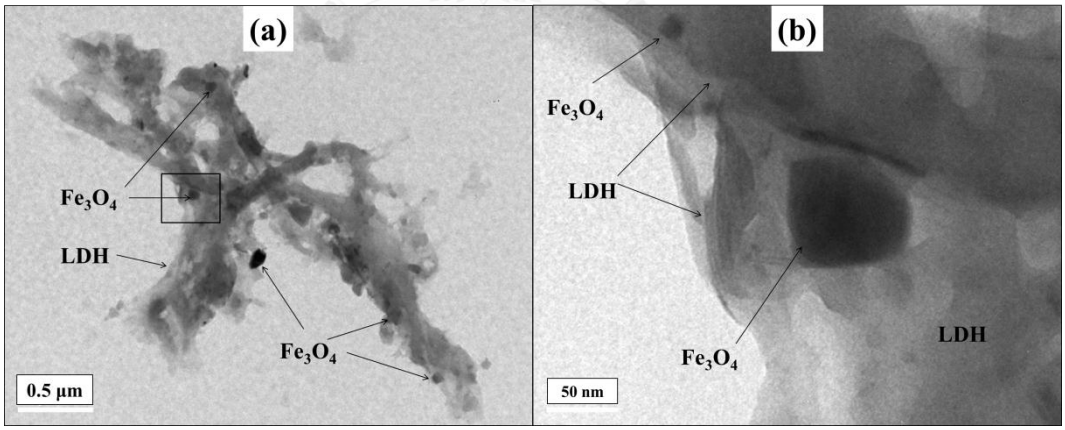

Figure 4.64 TEM images of m-LDH (a) with scale bar of 0.5 μm and (b) the enlarge of the square box in (a).

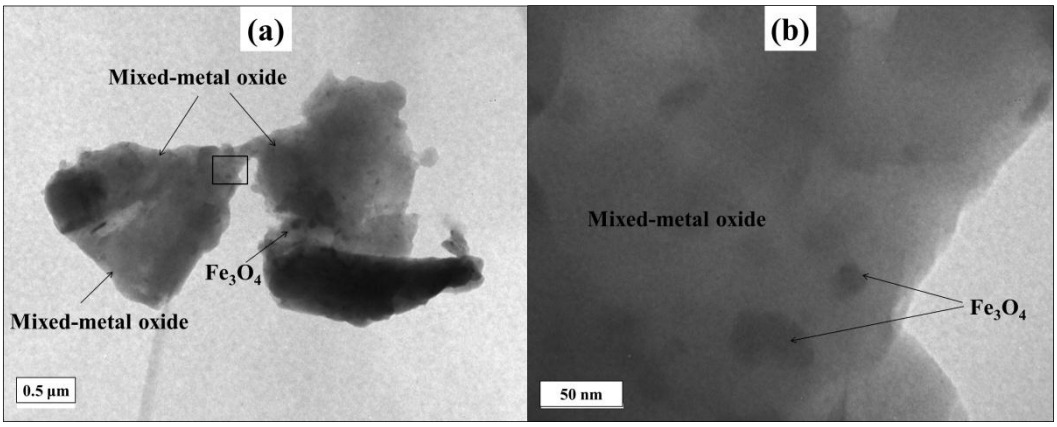

Figure 4.65 TEM images of cm-LDH: (a) with scale bar of 0.5 μm and (b) the enlarge of the square area in (a).

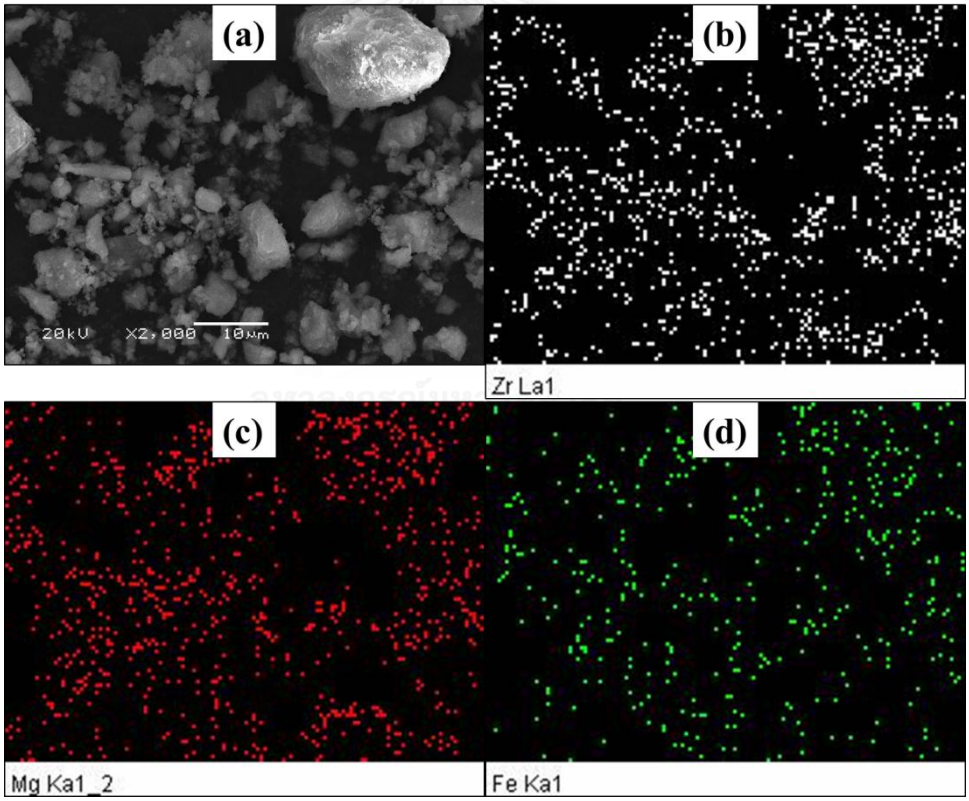

Figure 4.66 SEM-EDX of cm-LDH showing (a) particles, and the distributions of (b) Zr atoms, (c) Mg atoms and (d) Fe atoms.

Figure 4.67 shows the magnetic hysteresis loops of Fe_3O_4 and cm-LDH. The lower saturated magnetization parameter (Ms) of cm-LDH (3.6 emu/g), compared with that of Fe_3O_4 (142.7 emu/g), was due to the nonmagnetic LDH coated around Fe_3O_4, which interrupted the magnetic induction among magnetic domains under the external field. A similar phenomenon for Fe_3O_4 was previously reported [19, 122, 145, 146] as shown in Table 4.9.

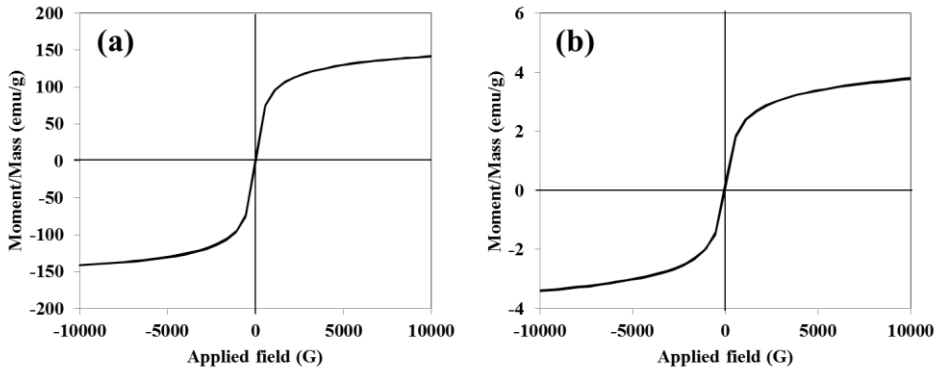

Figure 4.67 Magnetization hysteresis curves of (a) Fe_3O_4 and (b) cm-LDH.

Table 4.9 The saturated magnetization of various magnetic composites

Samples	Saturated magnetization (emu/g)	References
Fe_3O_4	69.86	[122]
Fe_3O_4/SiO_2	13.611	[122]
Fe_3O_4/SiO_2/OA	9.918	[122]
Magnetic SEP	31.82	[145]
ATP/ Fe_3O_4	13.23	[146]
MMIPs	5.67	[146]
MNIPs	5.12	[146]
Nano magnetite (NM)	63	[19]
Fe-hydrotalcite-NM	6	[19]
Fe_3O_4	142.7	This study
cm-LDH	3.6	This study

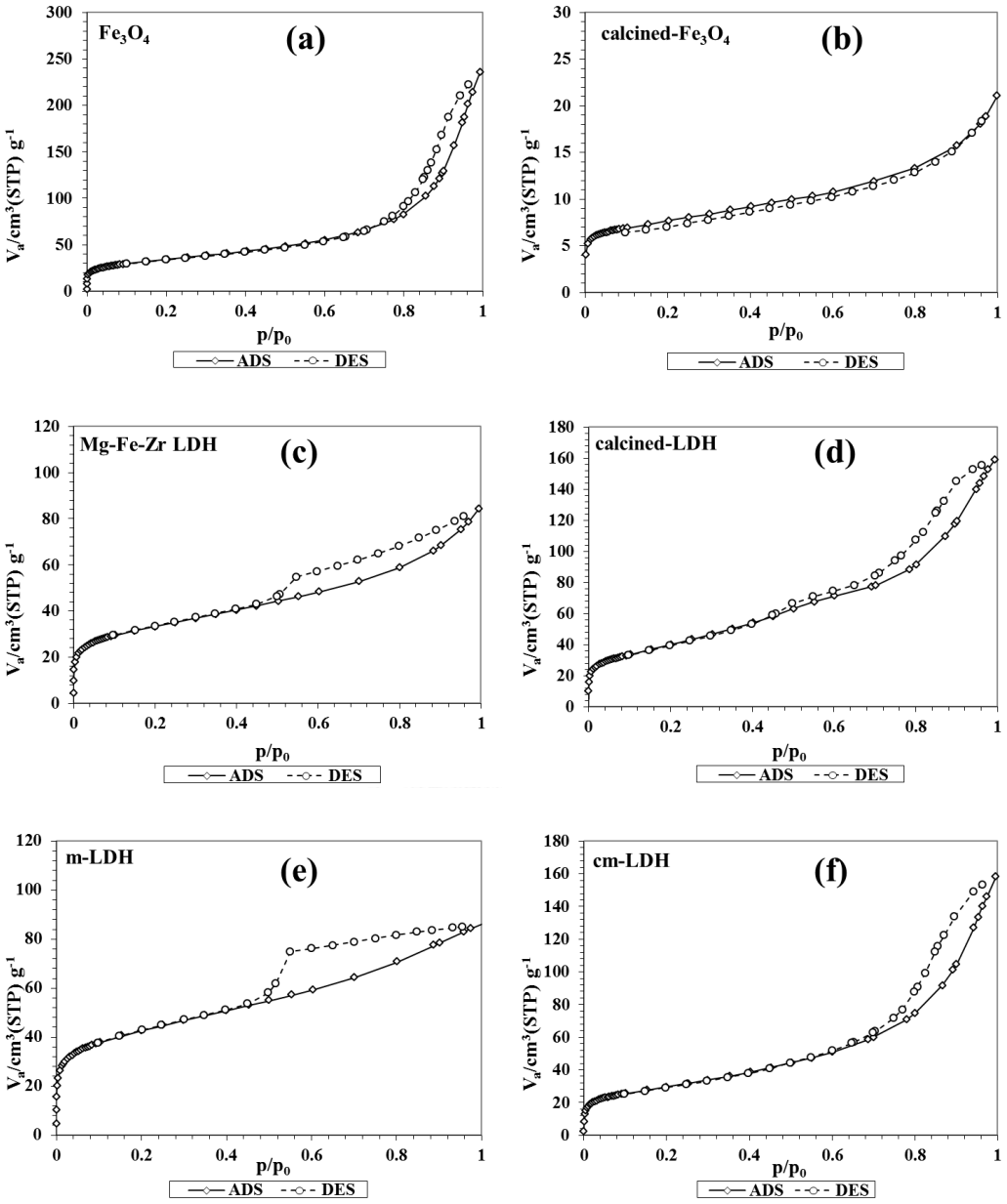

Figure 4.68 Nitrogen adsorption/desorption isotherms of (a) Fe_3O_4, (b) calcined Fe_3O_4, (c) Mg-Fe-Zr LDH, (d) calcined Mg-Fe-Zr LDH (c-LDH), (e) as-synthesized m-LDH composite, and (f) cm-LDH.

The nitrogen adsorption-desorption isotherms shown in Figure 4.68 and the surface area results summarized in Table 4.10 reveal the effects of the calcination process. The isotherm of bare Fe_3O_4, synthesized by rapid precipitation, exhibited a

small hysteresis loop with a high surface area. After calcination, Fe_3O_4 nanoparticles became α-Fe_2O_3 aggregates, in which their isotherm follows type I adsorption characteristics. The LDH and as-synthesized m-LDH composite possessed type IV adsorption isotherms due to the lamellar morphology of the LDH. After calcination, the LDH phase was converted to fine particles of mixed-metal oxides, resulting in a surface area increase [42] and the micro-mesoporous character being maintained.

4.8 Optimization of As(V) adsorption parameters of magnetic/LDH composite

Along with the As(V) adsorption test of cm-LDH, the adsorption of bare Fe_3O_4 and the LDH and their calcined counterparts were also investigated for comparison. The adsorption condition of pH 3 for three days was set to ensure that the dominant species of As(V) was in the anionic form without competing hydroxide ions, because $H_2AsO_4^-$ is the predominant species at pH 3-6 [147, 148]. The LDH possesses an anionic-exchange ability due to its cationic framework, therefore, the acidic region reduces the amount of competing hydroxide anions. The adsorption of As(V) on all adsorbents is presented in Table 4.10. The c-LDH and cm-LDH possess higher adsorption amounts than their non-calcined counterparts due to the increase of surface area after calcination. These results agree with previous reports that the calcination process of LDHs causes increases in surface area and porosity and a decrease in the amount of counter anions between the interlayers of the calcined-LDHs [42, 149, 150]. In the case of iron oxides, their surface area decreased dramatically after calcination due to the phase transformation and particle aggregation, resulting in lower adsorption capacity. The cm-LDH showed lower adsorption than c-LDH, because the composite contained the Fe_3O_4 phase.

In order to address the role of each component, the calculated adsorption amounts were estimated from the sum of the adsorption amount of each component. The amount of each component was estimated from the stoichiometric ratio of the starting materials. The as-synthesized m-LDH composite is comprised of 92% LDH and 8% Fe_3O_4, by weight, whereas cm-LDH is comprised of 87% c-LDH and 13% Fe_3O_4, by weight. Their calculated adsorption amounts are 88 and 182 mg As/g, respectively. Compared to the calculated adsorption amount of cm-LDH (182 mg

As/g), the experimental adsorption amount (188.2±3.1 mg As/g) shows a slightly higher value that could be due to the reduced crystallinity of the LDH phase, resulting from the presence of Fe_3O_4 particles. Moreover, the as-synthesized m-LDH composite and cm-LDH could be separated from the adsorption batch using an external magnetic field (Figure 4.69). As cm-LDH has a high adsorption amount and can be conveniently separated from the solution, its adsorption nature was further investigated.

Table 4.10 Surface area and As(V) adsorption amounts of the LDH, Fe_3O_4 and composites

Adsorbents	BET area (m^2/g)	Q (mg/g)	C_0 (mg/L)	pH	Time (h)	Ref.
Fe_3O_4	115.4±8.7	40.1±1.1	200	3	72	T
Fe_3O_4	40	8.8	1-7	6	24	[79]
Fe_3O_4	39.3	12.7*	0.5-150	6	336	[80]
Calcined Fe_3O_4	29.8±2.8	4.5±2.6	200	3	72	T
Mg-Fe-Zr-LDH	114.9±4.0	103.9±5.9	200	3	72	T
Mg-Fe-LDH	273	194*	4.5-1,199	6	24	[151]
c-LDH	144.0±1.2	203.3±6.6	200	3	72	T
m-LDH	99.3±0.7	102.2±7.8	200	3	72	T
Magnetic Mg-Al-LDH	-	24.09	75	4	24	[82]
cm-LDH	114.2±2.3	188.2±3.1	200	3	72	T

C_0 = 200 mg/L, m = 0.01g, V = 10 mL, shaking speed = 30 rpm and time = 3 days.

Dosage = 1 g/L or 5 g/L for Ref. [82, 151]

*Calculated from published data

T = this study

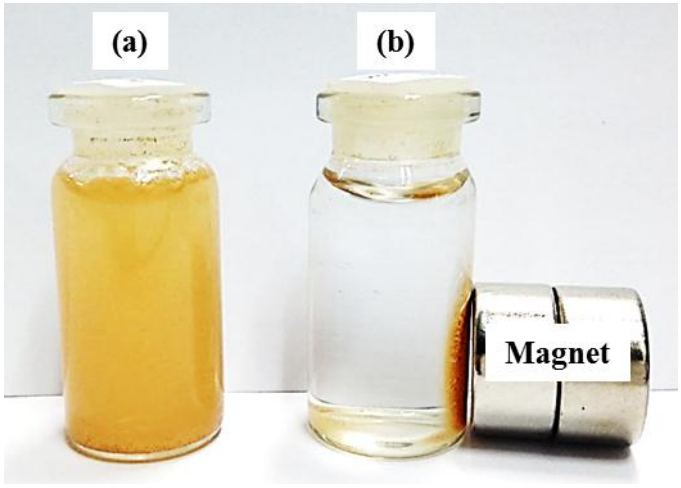

Figure 4.69 Demonstration of the magnetic separation of cm-LDH in aqueous As(V) solution (a) without and (b) with an external magnetic field

4.8.1 Effect of initial pH of arsenate solution

The effect of initial solution pH on the adsorption of As(V) was examined at different initial pH values, ranging from 2 to 11. The equilibrium pH value of each initial pH is plotted in Figure 4.70, showing the buffering ability of the composite at a pH around 10. The buffer nature results from the consumption of proton from aqueous solution in order to reconstruct the layer structure of the LDH from its calcined phase [150].

The adsorption of As(V) at different initial pH values is plotted Figure 4.70. The highest As(V) adsorption amount appeared at the initial solution of pH 3. Below pH 3, the adsorption amount dramatically decreased due to two reasons. First, the predominant species of As(V) is a neutral species and therefore the attraction force between cationic charge on the LDH layer and anionic charge of As(V) disappear resulting in lower sorption amount. Second, the partial dissolution of the mixed-metal oxide phase of calcined composites at pH values below 3. Above pH 3, the adsorption capacity decreased with increasing pH, which was due to two reasons, the difficulty in reconstructing the layered structure at high pH values [150] and the competitive adsorption of hydroxide ions on the adsorbent [42, 150]. This assumption is clearly observed in Figure 4.71 which shows the adsorption amount as a function of the difference between an equilibrium pH and an initial pH during the

buffer zone. The As(V) adsorption amount increases as the proton consumption increases.

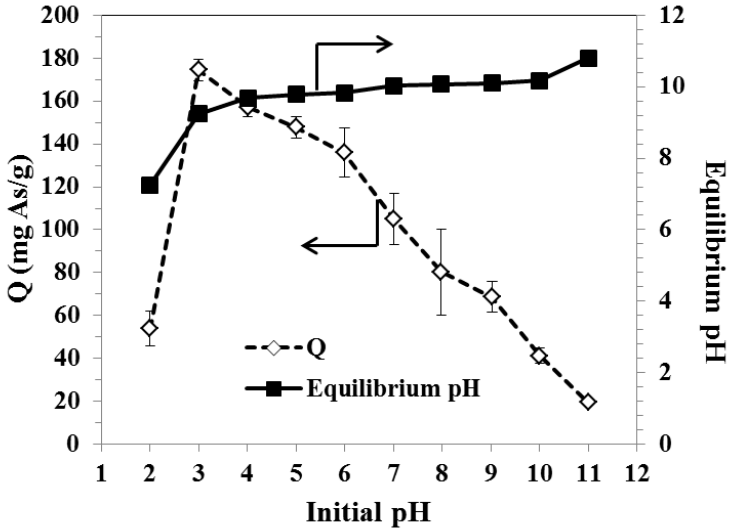

Figure 4.70 The pH buffer capacities of cm-LDH and the adsorption of As(V) on cm-LDH in various pH solutions. (C_0 = 200 mg/L, the contact time = 3 days)

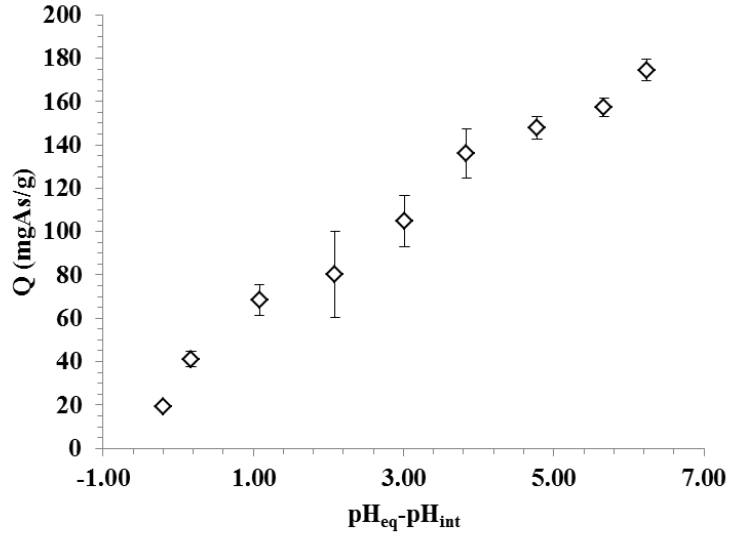

Figure 4.71 The adsorption of As(V) onto cm-LDH as a function of (pH_{eq} – pH_{int}). (C_0 = 200 mg/L, contact time = 3 days)

4.8.2 Effect of contact time

The effect of contact time on As(V) adsorption onto cm-LDH is shown in Figure 4.72. The kinetics could be separated into two steps, the first one reached equilibrium at 8 h and the second one started at 15 h. Because of the clear separation between the two steps, they could be modeled separately. The pseudo first-order kinetic and pseudo second-order kinetic models were used to identify the adsorption kinetics. As shown in Table 4.11, Figure 4.73 and Figure 4.74, the experimental data were fitted with the pseudo-second-order model (R^2 = 0.999 and 0.996), rather than with the pseudo-first-order model (R^2 = 0.647 and 0.901). The result agree with previous report that studied the adsorption of As(III) by Mg-Fe-Cl LDH [21]. It has been reported that the sorption mechanism of calcined-LDHs involves the rehydration of mixed-metal oxides and concurrent intercalation of As(V) and hydroxide ions into the interlayers to reconstruct the LDH within the first hour [42, 149]. Similarly in this work, cm-LDH could adsorb As(V) quickly in the beginning and reach equilibrium within 8 h, as shown in Figure 4.72 (a). The second process was observed starting from 15 to 120 h (Figure 4.72 b). This long-period process suggests that the mechanism could involve anion-exchange between arsenate ions in aqueous solution and hydroxide ions trapped in the LDH galleries. The XRD patterns of cm-LDH before and after the adsorption test were shown in Figure 4.75. The reappearance of the LDH peaks in the composite after adsorption is the result of the reconstruction of LDH phase in aqueous solution which proved a topotactic exchange mechanism [152]. A simple schematic presentation of the two-stepped mechanism is illustrated in Figure 4.76.

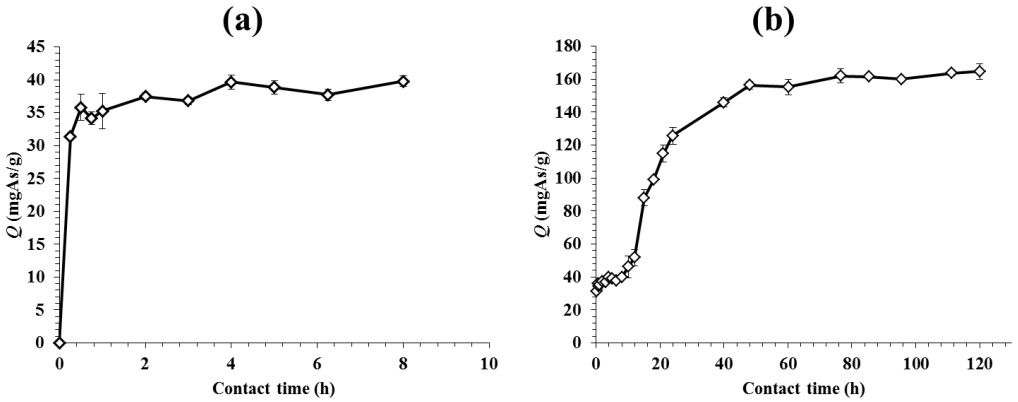

Figure 4.72 The effect of contact time on As(V) adsorption onto cm-LDH, (a) up to 8 h and (b) up to 120 h.

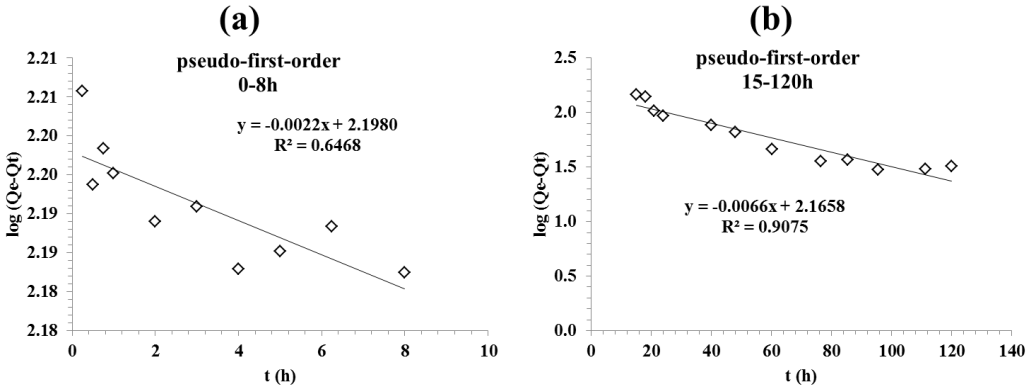

Figure 4.73 Linear plots of pseudo-first-order kinetic model of cm-LDH composite, (a) up to 8 h and (b) up to 120 h.

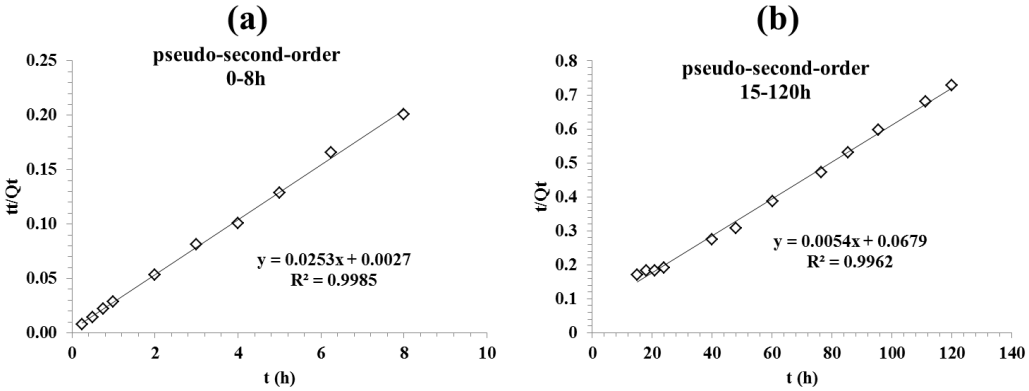

Figure 4.74 Linear plots of pseudo-second-order kinetic model of cm-LDH composite, (a) up to 8 h and (b) up to 120 h.

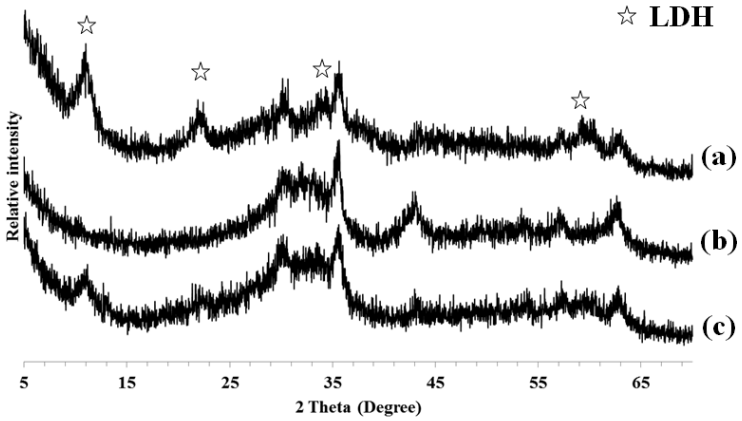

Figure 4.75 XRD patterns of the (a) as-synthesized m-LDH composite, (b) cm-LDH and (c) cm-LDH after As(V) adsorption

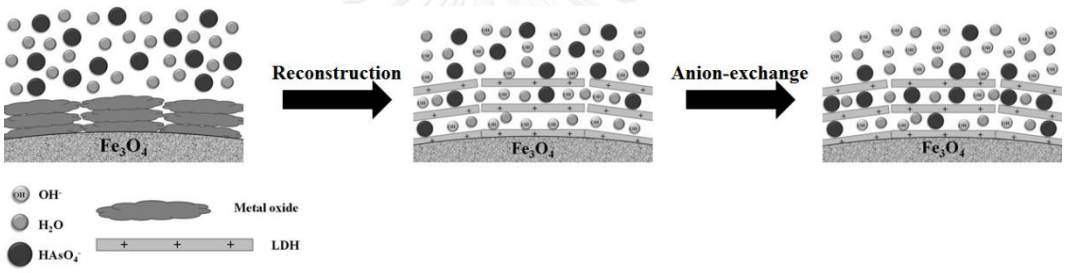

Figure 4.76 Schematic mechanism of As(V) adsorption by cm-LDH

Table 4.11 Adsorption kinetic parameters of As(V) adsorption onto the cm-LDH composite

	Times	Pseudo-first-order			Pseudo-second-order		
		k_1 (min^{-1})	$Q_{e,}$ (mg/g)	R^2	k_2 (gmg^{-1} in^{-1})	Q_e (mg/g)	R^2
cm-LDH	0-8 h	0.00506	158	0.647	0.236	39.6	0.999
	15-120 h	0.01524	146	0.908	0.000436	184	0.996

C_0 = 200 mg/L, m = 0.01g, V = 10 mL, shaking speed = 30 rpm

4.8.3 Effect of Initial concentration of arsenate

Figure 4.77 shows the adsorption isotherm of As(V) on cm-LDH. It can be seen that the As(V) adsorption amount increased with the increase of an equilibrium As(V) concentration. The steep slope at low C_{eq} and Q_e indicates that there were numerous readily adsorption sites at an initial stage. Langmuir and Freundlich models were employed to fit the experimental data (Figure 4.78 and Figure 4.79). The Langmuir and Freundlich constant parameters were summarized Table 4.12. The results show that the Langmuir model (R^2 = 0.991) is more suitable than the Freundlich model (R^2 = 0.742). The observed maximum As(V) adsorption capacity (192 mg/g) is closed to the adsorption amount from experiment (188 mg/g). This result indicated that the monolayer adsorption occurred at the anionic sites in the LDH galleries, confirming the mechanism in Figure 4.76. Moreover, the maximum adsorption capacities calculated from Langmuir equation (192 mg/g) and the equilibrium adsorption capacities calculated from the pseudo second order model (184 mg/g) show that the calculated values are reasonable.

The calculated R_L values were in the range 0.0022 to 0.0198 with a decreased R_L at high As(V) concentrations. The result suggested that the adsorption of As(V) onto cm-LDH composite was favorable adsorption process *[114, 115]*.

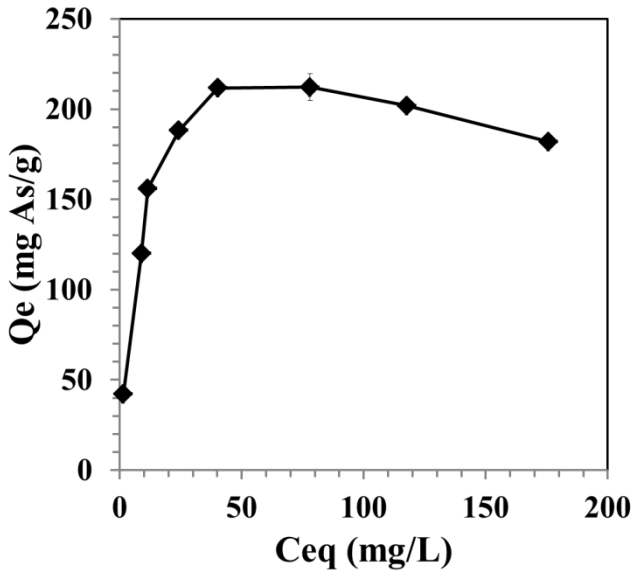

Figure 4.77 As(V) adsorption isotherm of cm-LDH.

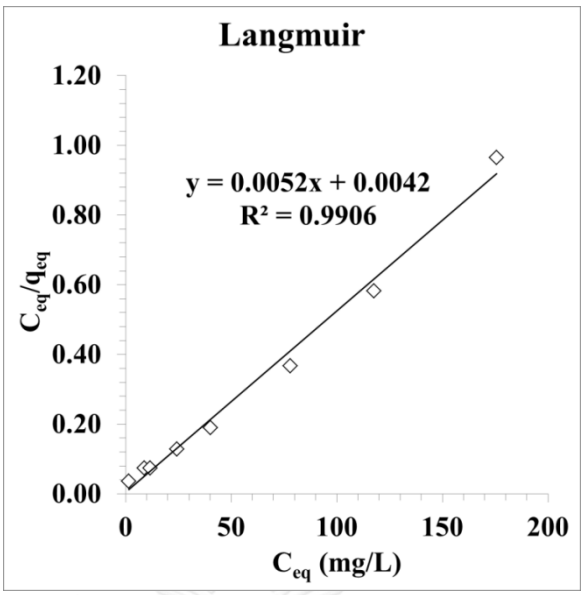

Figure 4.78 Langmuir isotherm plot of cm-LDH.

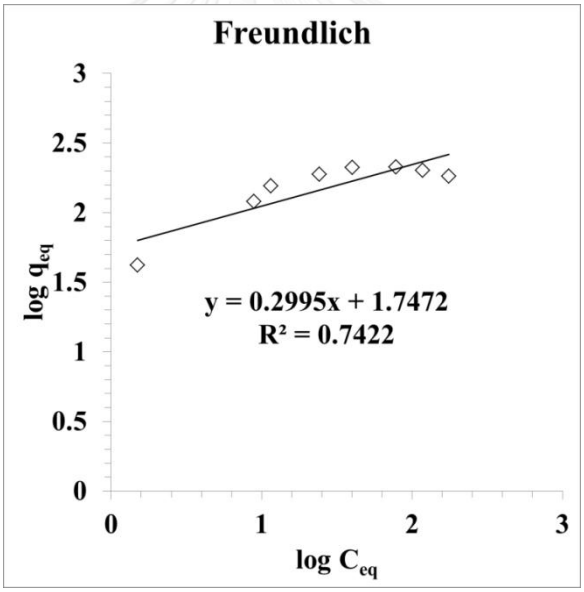

Figure 4.79 Freundlich isotherm plot of cm-LDH.

Table 4.12 Isotherm parameters of As(V) adsorption onto the cm-LDH composite

Material	Langmuir isotherm model				Freundlich isotherm model		
	Q_m(mg/g)	K_L (L/mg)	R_L	R^2	K_F	n	R^2
cm-LDH	192	1.24	0.0058	0.991	55.9	3.34	0.742

m = 0.01 g, V = 10 mL, shaking speed = 30 rpm, time = 3 days

4.9 As removals from real wastewater using magnetic/LDH composite

Two samples of wastewaters were obtained from the oil company in Thailand, TK80 and TK81. The initial As concentration of TK80 and TK81 were 82.1 mg/L and 78.4 mg/L, respectively. Figure 4.80 shows the As removal using cm-LDH. At low sorbent dosage (1 g/L) the As removal were 59.2% (TK80) and 40.8% (TK81). Increasing the sorbent dosage resulted to the increase in As removal. The removal reached 99.3% for both TK80 and TK81 using the sorbent dosage of 10 g/L, as the remaining of As in TK80 and TK81 were 0.57 mg/L and 0.58 mg/L, respectively. Compared to the removal of the synthetic As(V) solution, the much lower values of TK80 and TK81 could cause by competitive anion species in TK80 and TK81. As proposed mechanism in Figure 4.76, the electrostatic interaction of anions and cationic layer charge is predominant in the adsorption process, the effect of competitive anions would be severed.

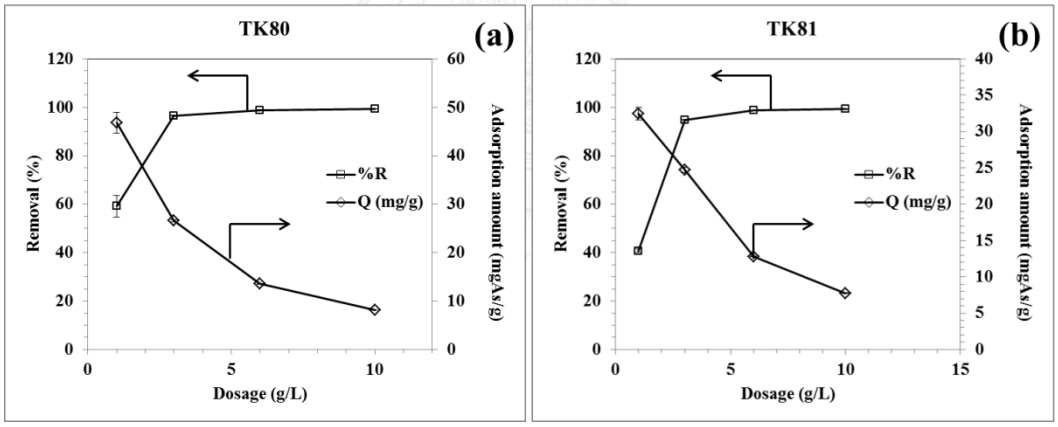

Figure 4.80 As removal from wastewater samples TK80 (a) and TK81 (b) from the oil company in Thailand.

CHAPTER 5
CONCLUSION

5.1 Synthesis of polymer/bentonite nanocomposites via solution intercalation method

Both pAPTMA/bentonite and pAETMA/bentonite nanocomposites were successful synthesized via solution intercalation method with pAPTMA or pAETMA intercalated in between the interlayers of bentonite.

5.1.1 Poly(3-acrylamidopropyl)trimethylammonium chloride)

For pAPTMA/bentonite nanocomposites, the monomer concentration did not affect the polymer amount and d-spacing. However, decreasing monomer concentration decreased the As(V) adsorption amount due to the dissolution of polymer with low M_n.

The increasing in MBA cross-linker amount did not affect the d-spacing of bentonite but decreased the crystallite size and slightly increased As(V) adsorption. The APS initiator concentration affected both d-spacing of bentonite and As(V) adsorption as it controlled the size of intercalated polymer. The higher APS concentration yielded the smaller d-spacing of nanocomposite. The suitable APS concentration was 2 % mole as provided highest the As(V) adsorption amount.

Changing in Na-bentonite concentration affected the structure of composites; the exfoliated nanocomposites were obtained using 5-20 %wt bentonite, and the intercalated nanocomposites were obtained using 30 - 40 %wt. The highest As(V) adsorption amount of 47.7 mg/g polymer was obtained from the 15M1C2A30B nanocomposite.

5.1.2 Poly([2-(acryloyloxy)ethyl]trimethylammonium chloride)

For pAETMA/bentonite nanocomposites, the increasing in monomer concentration resulted to slightly increased the polymer amount in the composite and the As(V) adsorption amount. The increasing in MBA amount result to slightly

increased As(V) adsorption. Whereas the increasing in APS concentration result to decreased the As(V) adsorption. The suitable APS concentration was 0.5 % mole as it is the lowest concentration that provided highest the As(V) adsorption amount. Changing in Na-bentonite concentration affected the structure of composites; the exfoliated nanocomposites were obtained using 5-20 %wt bentonite, and the intercalated nanocomposites were obtained using 30-50 %wt. The highest As(V) adsorption amount of 46.2 mg/g polymer was obtained from the 10M1C0.5A40B nanocomposite.

5.2 Synthesis of polymer/bentonite nanocomposites via *in-situ* intercalative polymerization method

Both pAPTMA/bentonite and pAETMA/bentonite nanocomposites were successful synthesized via *in-situ* intercalative polymerization method with pAPTMA or pAETMA intercalated in between the interlayers of bentonite.

5.2.1 Poly(3-acrylamidopropyl)trimethylammonium chloride)

The increasing in MBA amount did not affect the d-spacing of bentonite, however it lead to decreased the crystallite size and increased As(V) adsorption. The APS concentration affected the As(V) adsorption amount as it controlled the size of intercalated polymer. The APS concentration also affected the structure of composites; the intercalated nanocomposites were obtained using 0.5-1 %mole, and the exfoliated nanocomposites were obtained using 3-5 %mole. The suitable APS concentration was 1 % mole as provide highest the As(V) adsorption amount. Changing in Na-bentonite concentration affected the structure of composites, only the pure phase of intercalated nanocomposite was obtained at lower than 25 %wt bentonite. The highest As(V) adsorption amount of 14.6 mg/g polymer was obtained from the 1C0.5A10B nanocomposite.

5.2.2 Poly([2-(acryloyloxy)ethyl]trimethylammonium chloride)

The increasing in MBA amount did not affect the d-spacing of bentonite but seemingly lead to increase in the As(V) adsorption. The increasing in APS amount also did not affect the d-spacing of bentonite but decreased As(V) adsorption. The suitable APS concentration was 0.25 % mole as provided highest the As(V) adsorption amount. Changing in Na-bentonite concentration affected the structure of composites; the exfoliated nanocomposite was obtained using 5%wt bentonite, and the exfoliated nanocomposites were obtained using 7.5-22.5 %wt. The highest As(V) adsorption amount of 41.6 mg/g polymer was obtained from the 1C0.5A10B nanocomposite.

5.3 Comparison of the As(V) adsorption performance for the composite from different polymers and synthesis routes

Solution intercalation method gave the nanocomposites with higher As(V) adsorption amounts per weight of polymer than those produced by *in-situ* intercalative polymerization method. For the adsorption studies, the pseudo-second-order kinetic model was suitable to described the As(V) adsorption of both pAPTMA/bentonite and pAETMA/bentonite nanocomposites. The rate determining step chemisorption involves the anions exchange between arsenate anion in solution and chloride anion at polymer chain. The suitable pH for the As(V) adsorption was 9 for both nanocomposites.

The As(V) adsorption of both pAETMA/bentonite and pAPTMA/bentonite nanocomposites fitted with the Freundlich isotherm model suggesting the As(V) adsorption on heterogeneous surface of nanocomposites. Both nanocomposites possessed two active sites of positively charged $-N[CH_3]_3^+$ of polymercations and the hydroxyl groups (Al-OH and Si-OH) at the broken edges of bentonite layers.

The As(V) adsorption of both pAPTMA/bentonite and pAETMA/bentonite nanocomposites were affected by interference anions and the order of the affecting was: $H_2PO_4^-$ ~ SO_4^{2-} > CO_3^{2-} > NO_3^- > Cl^- (at molar ratio lower than 10) and $H_2PO_4^-$ > SO_4^{2-} ~ CO_3^{2-} > NO_3^- > Cl^- (at molar ratio of 50) for both nanocomposites.

Arsenic removal efficiency increased with increasing the sorbents dose for both TK80 and TK81 wastewaters. However, the values are very low due to interference anions in the wastewaters.

5.4 Synthesis of magnetic layered double hydroxide composite

The Fe_3O_4 was successful synthesized by coprecipitate method. The $[Mg_{0.66}Fe_{0.33-x}Zr_x(OH)_2](CO_3)\delta$ (x = 0 – 0.33) had the LDH structure, excepted for x = 0.33. The unit cell parameters and the As(V) adsorption amounts increased with increasing Zr contents. The Mg-Fe-Zr LDHs with x = 0.25 provided the highest As(V) adsorption amount.

The Fe_3O_4/Mg-Fe-Zr LDH composite was successful synthesized by coprecipitation of layered double hydroxide (LDH) precursors in the presence of Fe_3O_4 particles. The Fe_3O_4 particles were covered thoroughly by LDH platelets. The composite still remained magnetic behavior although calcined it up to 450 ^{o}C for 5h. The presence of LDH in the composite decreased the saturated magnetization of Fe_3O_4, but resulted to a high surface area of the composite.

5.5 The As(V) adsorption of Fe_3O_4/Mg-Fe-Zr LDH composite

The suitable pH for the As(V) adsorption of the composite was pH 3. The As(V) adsorption capacity of the composite (188 mg/g) is slightly lower than that of the calcined-LDH (203 mg/g), due to the low adsorption capacity of the core Fe_3O_4 (40.1 mg/g). The adsorption kinetics of the composite suggests a two-stepped adsorption mechanism. The initial adsorption occurred on the outer surface of the composite during the structural reconstruction process of LDH phase. After 24 h, the further adsorption resulted from the ion-exchange between the interlayers of reconstructed LDH. The adsorption isotherm is well fitted to the Langmuir model, describing the monolayer adsorption behavior within the interlayers of LDH. The removal reached 99.3% for both TK80 and TK81 using the sorbent dosage of 10 g/L, as the remaining of As in TK80 and TK81 were 0.57 mg/L and 0.58 mg/L, respectively.

5.6 Suggestions

5.6.1 The polymer/bentonite nanocomposites should be further tested in the basic wastewaters, because it performed better at high pH up to 9

5.6.2 The magnetic LDH composite should be further tested in the acid wastewaters, because it performed better at very low pH down to 3.

5.6.3 The adsorption of other anionic pollutant (for example, Cr(VI), HPO_4^{2-} and anionic dyes) onto the polrmer/bentonite nanocomposites and magnetic LDH were suggested for further studies. Because these composites provided the positively charge active sites for adsorbed anions.

REFERENCES

[1] Choong, T.S.Y., Chuah, T.G., Robiah, Y., Gregory Koay, F.L., and Azni, I. Arsenic toxicity, health hazards and removal techniques from water: an overview. Desalination 217(1–3) (2007): 139-166.

[2] Mohan, D. and Pittman Jr, C.U. Arsenic removal from water/wastewater using adsorbents—a critical review. Journal of Hazardous Materials 142(1–2) (2007): 1-53.

[3] Mandal, B.K. and Suzuki, K.T. Arsenic round the world: a review. Talanta 58(1) (2002): 201-235.

[4] Wang, S. and Mulligan, C.N. Occurrence of arsenic contamination in Canada: sources, behavior and distribution. Science of The Total Environment 366(2–3) (2006): 701-721.

[5] Chakrabortty, S., Sen, M., and Pal, P. Arsenic removal from contaminated groundwater by membrane-integrated hybrid plant: optimization and control using Visual Basic platform. Environmental Science and Pollution Research 21(5) (2014): 3840-3857.

[6] Chang, F.-f., Liu, W.-j., and Wang, X.-m. Comparison of polyamide nanofiltration and low-pressure reverse osmosis membranes on As(III) rejection under various operational conditions. Desalination 334(1) (2014): 10-16.

[7] He, J., Matsuura, T., and Chen, J.P. A novel Zr-based nanoparticle-embedded PSF blend hollow fiber membrane for treatment of arsenate contaminated water: Material development, adsorption and filtration studies, and characterization. Journal of Membrane Science 452 (2014): 433-445.

[8] Urbano, B.F., Rivas, B.L., Martinez, F., and Alexandratos, S.D. Equilibrium and kinetic study of arsenic sorption by water-insoluble nanocomposite resin of poly[N-(4-vinylbenzyl)-N-methyl-d-glucamine]-montmorillonite. Chemical Engineering Journal 193–194 (2012): 21-30.

[9] Dominguez-Ramos, A., et al. Arsenic removal from natural waters by adsorption or ion exchange: an environmental sustainability assessment. Industrial & Engineering Chemistry Research 53(49) (2014): 18920-18927.

[10] Mertens, J., et al. Adsorption of arsenic on polyaluminum granulate. Environmental Science & Technology 46(13) (2012): 7310-7317.

[11] Guo, Q. and Tian, J. Removal of fluoride and arsenate from aqueous solution by hydrocalumite via precipitation and anion exchange. Chemical Engineering Journal 231 (2013): 121-131.

[12] Haraguchi, D., Tokoro, C., Oda, Y., and Owada, S. Sorption mechanisms of arsenate in aqueous solution during coprecipitation with aluminum hydroxide. Journal of Chemical Engineering of Japan 46(2) (2013): 173-180.

[13] Sun, Y., Zhou, G., Xiong, X., Guan, X., Li, L., and Bao, H. Enhanced arsenite removal from water by $Ti(SO_4)_2$ coagulation. Water Research 47(13) (2013): 4340-8.

[14] Francisca, F.M. and Carro Perez, M.E. Arsenic removal by coagulation-flocculation processes. Revista Internacional De Contaminacion Ambiental 30(2) (2014): 177-190.

[15] Unuabonah, E.I. and Taubert, A. Clay–polymer nanocomposites (CPNs): Adsorbents of the future for water treatment. Applied Clay Science 99 (2014): 83-92.

[16] Chetia, M., et al. Arsenic removal from water using calcined Mg–Al layered double hydroxide. Clean Technologies and Environmental Policy 14(1) (2012): 21-27.

[17] Gupta, A., Yunus, M., and Sankararamakrishnan, N. Zerovalent iron encapsulated chitosan nanospheres – a novel adsorbent for the removal of total inorganic Arsenic from aqueous systems. Chemosphere 86(2) (2012): 150-155.

[18] Tiwari, D. and Lee, S.M. Novel hybrid materials in the remediation of ground waters contaminated with As(III) and As(V). Chemical Engineering Journal 204–206 (2012): 23-31.

[19] Türk, T., Alp, İ., and Deveci, H. Adsorption of As(V) from water using Mg–Fe-based hydrotalcite (FeHT). Journal of Hazardous Materials 171(1–3) (2009): 665-670.

[20] Jain, C.K. and Singh, R.D. Technological options for the removal of arsenic with special reference to South East Asia. Journal of Environmental Management 107 (2012): 1-18.

[21] Jiang, J.Q., Ashekuzzaman, S.M., Hargreaves, J.S.J., McFarlane, A.R., Badruzzaman, A.B.M., and Tarek, M.H. Removal of Arsenic (III) from groundwater applying a reusable Mg-Fe-Cl layered double hydroxide. Journal of Chemical Technology and Biotechnology 90(6) (2015): 1160-1166.

[22] Vunain, E., Mishra, A.K., and Krause, R.W. Fabrication, characterization and application of polymer nanocomposites for arsenic(III) removal from water. Journal of Inorganic and Organometallic Polymers and Materials 23(2) (2013): 293-305.

[23] Wang, J., Xu, W., Chen, L., Huang, X., and Liu, J. Preparation and evaluation of magnetic nanoparticles impregnated chitosan beads for arsenic removal from water. Chemical Engineering Journal 251 (2014): 25-34.

[24] Wang, Y., Morin, G., Ona-Nguema, G., and Brown, G.E. Arsenic(III) and arsenic(V) speciation during transformation of lepidocrocite to magnetite. Environmental Science & Technology 48(24) (2014): 14282-14290.

[25] Burton, E.D., et al. Sorption of arsenic(V) and arsenic(III) to schwertmannite. Environmental Science & Technology 43(24) (2009): 9202-9207.

[26] Pehlivan, E., Tran, T.H., Ouédraogo, W.K.I., Schmidt, C., Zachmann, D., and Bahadir, M. Removal of As(V) from aqueous solutions by iron coated rice husk. Fuel Processing Technology 106 (2013): 511-517.

[27] Olad, A. Polymer/Clay Nanocomposites. in *Advances in Diverse Industrial Applications of Nanocomposites*, Reddy, B., Editor. 2011, InTech.

[28] Gacitua, W., Ballerini, A., and Zhang, J. Polymer nanocomposites: synthetic and natural fillers a review. Maderas. Ciencia y tecnología 7 (2005): 159-178.

[29] Mittal, V. Polymer Layered Silicate Nanocomposites: a review. Materials 2(3) (2009): 992.

[30] Ajayan, P.M. Bulk Metal and ceramics nanocomposites. in Nanocomposite Science and Technology, pp. 1-75: Wiley-VCH Verlag GmbH & Co. KGaA, 2004.

[31] Theng, B.K.G. Chapter 7 - Polymer–Clay Nanocomposites. in Theng, B.K.G. (ed.) Developments in Clay Science, pp. 201-241: Elsevier, 2012.

[32] Camargo, P.H.C., Satyanarayana, K.G., and Wypych, F. Nanocomposites: synthesis, structure, properties and new application opportunities. Materials Research 12 (2009): 1-39.

[33] Kurecic, M. and Smole, M.S. Polymer nanocomposite hydrogels for water purification. in *Nanocomposites - New Trends and Developments*, Ebrahimi, F., Editor. 2012, InTech. 161-185.

[34] Alexandre, M. and Dubois, P. Polymer-layered silicate nanocomposites: preparation, properties and uses of a new class of materials. Materials Science and Engineering: R: Reports 28(1–2) (2000): 1-63.

[35] Wang, B., Yin, Y., Liu, C., Yu, S., and Chen, K. Synthesis and characterization of clay/polyaniline nanofiber hybrids. Journal of Applied Polymer Science 128(2) (2013): 1304-1312.

[36] Hayati-Ashtiani, M. Characterization of nano-porous bentonite (montmorillonite) particles using FTIR and BET-BJH analyses. Particle & Particle Systems Characterization 28(3-4) (2011): 71-76.

[37] Lee, S.M. and Tiwari, D. Organo and inorgano-organo-modified clays in the remediation of aqueous solutions: an overview. Applied Clay Science 59–60 (2012): 84-102.

[38] Sinha Ray, S. and Okamoto, M. Polymer/layered silicate nanocomposites: a review from preparation to processing. Progress in Polymer Science 28(11) (2003): 1539-1641.

[39] Brigatti, M.F., Galán, E., and Theng, B.K.G. Chapter 2 - Structure and Mineralogy of Clay Minerals. in Faïza, B. and Gerhard, L. (eds.), Developments in Clay Science, pp. 21-81: Elsevier, 2013.

[40] Schmidt, C.U. and Lagaly, G. Surface modification of bentonites; I, Betaine montmorillonites and their rheological and colloidal properties. Clay Minerals 34(3) (1999): 447-458.

[41] Lee, J. and Shackelford, C. Impact of Bentonite Quality on Hydraulic Conductivity of Geosynthetic Clay Liners. Journal of Geotechnical and Geoenvironmental Engineering 131(1) (2005): 64-77.

[42] Goh, K.-H., Lim, T.-T., and Dong, Z. Application of layered double hydroxides for removal of oxyanions: a review. Water Research 42(6–7) (2008): 1343-1368.

[43] Forano, C., Hibino, T., Leroux, F., and Taviot-Guého, C. Chapter 13.1 Layered double hydroxides. in Faïza Bergaya, B.K.G.T. and Gerhard, L. (eds.), Developments in clay science, pp. 1021-1095: Elsevier, 2006.

[44] Bish, D.L. Anion exchange in takovite: applications to other hydroxide minerals. Bulletin de minéralogie 103 (1980): 170-175.

[45] Cavani, F., Trifirò, F., and Vaccari, A. Hydrotalcite-type anionic clays: preparation, properties and applications. Catalysis Today 11(2) (1991): 173-301.

[46] Reichle, W.T. Synthesis of anionic clay minerals (mixed metal hydroxides, hydrotalcite). Solid State Ionics 22(1) (1986): 135-141.

[47] Rivas, B., Pereira, E., Paredes, J., and Sánchez, J. Removal of arsenate from ionic mixture by anion exchanger water-soluble polymers combined with ultrafiltration membranes. Polymer Bulletin 69(9) (2012): 1007-1022.

[48] Zeng, X. and Ruckenstein, E. Cross-linked macroporous chitosan anion-exchange membranes for protein separations. Journal of Membrane Science 148(2) (1998): 195-205.

[49] Barakat, M.A. and Sahiner, N. Cationic hydrogels for toxic arsenate removal from aqueous environment. Journal of Environmental Management 88(4) (2008): 955-961.

[50] Hammud, H., Abbas, I., and Al-khalili, D. Kinetics and thermodynamics of chromate and phosphate uptake by polypyrrole: batch and column studies. Journal of Inclusion Phenomena and Macrocyclic Chemistry 82(3-4) (2015): 395-405.

[51] Kusku, O., Rivas, B.L., Urbano, B.F., Arda, M., Kabay, N., and Bryjak, M. A comparative study of removal of Cr(VI) by ion exchange resins bearing

quaternary ammonium groups. Journal of Chemical Technology & Biotechnology 89(6) (2014): 851-857.

[52] Thakare, S.R., Pal, M.R., and Jadhao, S.Z. Simple synthesis of highly selective and fast Hg(II) removal polymer from aqueous solution. Designed Monomers and Polymers 18(7) (2015): 650-660.

[53] Kaşgöz, H., Durmuş, A., and Kaşgöz, A. Enhanced swelling and adsorption properties of AAm-AMPSNa/clay hydrogel nanocomposites for heavy metal ion removal. Polymers for Advanced Technologies 19(3) (2008): 213-220.

[54] Kaplan, M. and Kasgoz, H. Hydrogel nanocomposite sorbents for removal of basic dyes. Polymer Bulletin 67(7) (2011): 1153-1168.

[55] Urbano, B. and Rivas, B. Poly(sodium 4-styrene sulfonate) and poly(2-acrylamidoglycolic acid) nanocomposite hydrogels: montmorillonite effect on water absorption, thermal, and rheological properties. Polymer Bulletin 67(9) (2011): 1823-1836.

[56] Güçlü, G., Al, E., Emik, S., İyim, T., Özgümüş, S., and Özyürek, M. Removal of Cu^{2+} and Pb^{2+} ions from aqueous solutions by starch-graft-acrylic acid/montmorillonite superabsorbent nanocomposite hydrogels. Polymer Bulletin 65(4) (2010): 333-346.

[57] Irani, M., Ismail, H., and Ahmad, Z. Preparation and properties of linear low-density polyethylene-g-poly (acrylic acid)/organo-montmorillonite superabsorbent hydrogel composites. Polymer Testing 32(3) (2013): 502-512.

[58] Starodoubtsev, S.G., Churochkina, N.A., and Khokhlov, A.R. Hydrogel composites of neutral and slightly charged poly(acrylamide) gels with incorporated bentonite. interaction with salt and ionic surfactants. Langmuir 16(4) (2000): 1529-1534.

[59] Zadaka, D., Nir, S., Radian, A., and Mishael, Y.G. Atrazine removal from water by polycation–clay composites: effect of dissolved organic matter and comparison to activated carbon. Water Research 43(3) (2009): 677-683.

[60] Anirudhan, T.S. and Suchithra, P.S. Adsorption characteristics of humic acid-immobilized amine modified polyacrylamide/bentonite composite for cationic

dyesin aqueous solutions. Journal of Environmental Sciences 21(7) (2009): 884-891.

[61] Ganigar, R., Rytwo, G., Gonen, Y., Radian, A., and Mishael, Y.G. Polymer–clay nanocomposites for the removal of trichlorophenol and trinitrophenol from water. Applied Clay Science 49(3) (2010): 311-316.

[62] Futalan, C.M., Kan, C.-C., Dalida, M.L., Hsien, K.-J., Pascua, C., and Wan, M.-W. Comparative and competitive adsorption of copper, lead, and nickel using chitosan immobilized on bentonite. Carbohydrate Polymers 83(2) (2011): 528-536.

[63] Bulut, Y., Akcay, G., Elma, D., and Serhatli, I.E. Synthesis of clay-based superabsorbent composite and its sorption capability. Journal of Hazardous Materials 171(1-3) (2009): 717-23.

[64] Mansri, A., Benabadji, K.I., Desbrières, J., and François, J. Chromium removal using modified poly(4-vinylpyridinium) bentonite salts. Desalination 245(1–3) (2009): 95-107.

[65] Natkaǹski, P., Kuśtrowski, P., Białas, A., Piwowarska, Z., and Michalik, M. Thermal stability of montmorillonite polyacrylamide and polyacrylate nanocomposites and adsorption of Fe(III) ions. Applied Clay Science 75–76 (2013): 153-157.

[66] Lvov, Y., Ariga, K., Ichinose, I., and Kunitake, T. Formation of ultrathin multilayer and hydrated gel from montmorillonite and linear polycations. Langmuir 12(12) (1996): 3038-3044.

[67] Li, Z., Beachner, R., McManama, Z., and Hanlie, H. Sorption of arsenic by surfactant-modified zeolite and kaolinite. Microporous and Mesoporous Materials 105(3) (2007): 291-297.

[68] Li, Q., Yue, Q., Su, Y., and Gao, B. Equilibrium and a two-stage batch adsorber design for reactive or disperse dye removal to minimize adsorbent amount. Bioresource Technology 102(9) (2011): 5290-5296.

[69] Constantin, M., Asmarandei, I., Harabagiu, V., Ghimici, L., Ascenzi, P., and Fundueanu, G. Removal of anionic dyes from aqueous solutions by an ion-

exchanger based on pullulan microspheres. Carbohydrate Polymers 91(1) (2013): 74-84.

[70] Patel, Y.N. and Patel, M.P. Adsorption of azo dyes from water by new poly (3-acrylamidopropyl)-trimethylammonium chloride-co-N,N-dimethylacrylamide superabsorbent hydrogel—Equilibrium and kinetic studies. Journal of Environmental Chemical Engineering 1(4) (2013): 1368-1374.

[71] Morales, D.V., Rivas, B.L., and Escalona, N. Poly([(2-methacryloyloxy)ethyl]trimethylammonium chloride): synthesis, characterization, and removal properties of As(V). Polymer Bulletin 73(3) (2016): 875-890.

[72] Chen, L., et al. Application of metal oxide heterostructures in arsenic removal from contaminated water. Journal of Nanomaterials 2014 (2014): 10.

[73] Seko, N., Basuki, F., Tamada, M., and Yoshii, F. Rapid removal of arsenic(V) by zirconium(IV) loaded phosphoric chelate adsorbent synthesized by radiation induced graft polymerization. Reactive and Functional Polymers 59(3) (2004): 235-241.

[74] Zhu, X. and Jyo, A. Removal of arsenic(V) by zirconium(IV)-loaded phosphoric acid chelating resin. Separation Science and Technology 36(14) (2001): 3175-3189.

[75] Chitrakar, R., et al. Uptake properties of phosphate on a novel Zr–modified MgFe–LDH(CO_3). Journal of Colloid and Interface Science 349(1) (2010): 314-320.

[76] Mandel, K., Drenkova-Tuhtan, A., Hutter, F., Gellermann, C., Steinmetz, H., and Sextl, G. Layered double hydroxide ion exchangers on superparamagnetic microparticles for recovery of phosphate from waste water. Journal of Materials Chemistry A 1(5) (2013): 1840-1848.

[77] Dambies, L. Existing and prospective sorption technologies for the removal of arsenic in water. Separation Science and Technology 39(3) (2005): 603-627.

[78] Liu, C.-H., et al. Mechanism of arsenic adsorption on magnetite nanoparticles from water: thermodynamic and spectroscopic studies. Environmental Science & Technology 49(13) (2015): 7726-7734.

[79] Song, K., Kim, W., Suh, C.-Y., Shin, D., Ko, K.-S., and Ha, K. Magnetic iron oxide nanoparticles prepared by electrical wire explosion for arsenic removal. Powder Technology 246 (2013): 572-574.

[80] Salazar-Camacho, C., Villalobos, M., Rivas-Sánchez, M.d.l.L., Arenas-Alatorre, J., Alcaraz-Cienfuegos, J., and Gutiérrez-Ruiz, M.E. Characterization and surface reactivity of natural and synthetic magnetites. Chemical Geology 347 (2013): 233-245.

[81] Pati, S.S., Gopinath, S., Panneerselvam, G., Antony, M.P., and Philip, J. High temperature phase transformation studies in magnetite nanoparticles doped with Co^{2+} ion. Journal of Applied Physics 112(5) (2012): 054320.

[82] Toledo, T.V., Bellato, C.R., Rosário, R.H.d., and Marques Neto, J.d.O. Adsorção de arsênio(V) pelo compósito magnético hidrotalcita: óxido de ferro. Química Nova 34 (2011): 561-567.

[83] Zhang, H., Huang, F., Liu, D.-L., and Shi, P. Highly efficient removal of Cr(VI) from wastewater via adsorption with novel magnetic Fe_3O_4@C@MgAl-layered double-hydroxide. Chinese Chemical Letters 26(9) (2015): 1137-1143.

[84] Guggenheim, S. and Martin, R.T. Definition of clay and clay mineral: joint report of the AIPEA nomenclature and CMS nomenclature committees. Clays and Clay Minerals 43(2) (1995): 255-256.

[85] Bergaya, F. and Lagaly, G. Chapter 1 General introduction: clays, clay minerals, and clay science. in Faïza Bergaya, B.K.G.T. and Gerhard, L. (eds.), Developments in clay science, pp. 1-18: Elsevier, 2006.

[86] Brigatti, M.F., Galan, E., and Theng, B.K.G. Chapter 2 Structures and mineralogy of clay minerals. in Faïza Bergaya, B.K.G.T. and Gerhard, L. (eds.), Developments in clay science, pp. 19-86: Elsevier, 2006.

[87] Goldman, L.J., Greenfield, L.l., Damle, A.S., Kingsbury, G.L., Northeim, C.M., and Truesdale, R.S. Clay liners for waste management facilities [Online]. Available from: http://www.groundwaterresearch.com.au/reference_files/clay_liners/clay_liners [july 20, 2016]

[88] [Online]. Available from: http://keizee.home.xs4all.nl/osmosis/osmosis/osmosis/osmosis21_files/synthesis%20of%20clays.jpg [June 8, 2016]

[89] Evans, D.G. and Slade, R.C.T. Structural aspects of layered double hydroxides. in Duan, X. and Evans, D.G. (eds.), Layered double hydroxides, pp. 1-87. Berlin, Heidelberg: Springer Berlin Heidelberg, 2006.

[90] Brucite [Online]. Available from: http://www.wikiwand.com/fr/Brucite [June 9, 2016]

[91] Benício, L.P.F., et al. Layered double hydroxides: nanomaterials for applications in agriculture. Revista Brasileira de Ciência do Solo 39 (2015): 1-13.

[92] Mills, S.J., Christy, A.G., Génin, J.-M.R., Kameda, T., and Colombo, F. Nomenclature of the hydrotalcite supergroup: natural layered double hydroxides. Mineralogical Magazine 76(5) (2012): 1289-1336.

[93] Velu, S., Sabde, D.P., Shah, N., and Sivasanker, S. New hydrotalcite-like anionic clays containing Zr^{4+} in the layers: synthesis and physicochemical properties. Chemistry of Materials 10(11) (1998): 3451-3458.

[94] Velu, S., Suzuki, K., Kapoor, M.P., Tomura, S., Ohashi, F., and Osaki, T. Effect of Sn incorporation on the thermal transformation and reducibility of M(II)Al-layered double hydroxides [M(II) = Ni or Co]. Chemistry of Materials 12(3) (2000): 719-730.

[95] Velu, S., Suzuki, K., Okazaki, M., Osaki, T., Tomura, S., and Ohashi, F. Synthesis of new Sn-incorporated layered double hydroxides and their thermal evolution to mixed oxides. Chemistry of Materials 11(8) (1999): 2163-2172.

[96] Tichit, D., Das, N., Coq, B., and Durand, R. Preparation of Zr-containing layered double hydroxides and characterization of the acido-basic properties of their mixed oxides. Chemistry of Materials 14(4) (2002): 1530-1538.

[97] He, J., Wei, M., Li, B., Kang, Y., Evans, D.G., and Duan, X. Preparation of layered double hydroxides. in Duan, X. and Evans, D.G. (eds.), Layered double hydroxides, pp. 89-119. Berlin, Heidelberg: Springer Berlin Heidelberg, 2006.

[98] Callister, W.D. Materials science and engineering: an introduction, 7th Edition Wiley Plus Set. John Wiley & Sons, Limited, 2007.

[99] Pinnavaia, T.J., Lan, T., Wang, Z., Shi, H., and Kaviratna, P.D. Clay-reinforced epoxy nanocomposites: synthesis, properties, and mechanism of formation. in Nanotechnology, pp. 250-261: American Chemical Society, 1996.

[100] Pavlidou, S. and Papaspyrides, C.D. A review on polymer–layered silicate nanocomposites. Progress in Polymer Science 33(12) (2008): 1119-1198.

[101] Chen, B., et al. A critical appraisal of polymer-clay nanocomposites. Chem Soc Rev 37(3) (2008): 568-94.

[102] Stout, G.H. and Jensen, L.H. X-ray structure determination: a practical guide. Macmillan, 1968.

[103] Bragg, W.H. and Bragg, W.L. The reflection of X-rays by crystals. Proceedings of the Royal Society of London A: Mathematical, Physical and Engineering Sciences 88(605) (1913): 428-438.

[104] Sing, K.S.W., et al. Reporting physisorption data for gas/solid systems. IUPAC Commission on Colloid and Surface Chemistry including Catalysis. Pure and Applied Chemistry 57(4) (1985): 603-619.

[105] Kaneko, K. Determination of pore size and pore size distribution: 1. Adsorbents and catalysts. Journal of Membrane Science 96(1–2) (1994): 59-89.

[106] Balbuena, P.B. and Gubbins, K.E. Classification of adsorption behavior: simple fluids in pores of slit-shaped geometry. Fluid Phase Equilibria 76 (1992): 21-35.

[107] Adsorption Isotherm [Online]. Available from: http://www.microtrac-bel.com/en/tech/bel/seminar02.html [June 9,2016]

[108] Brunauer, S., Emmett, P.H., and Teller, E. Adsorption of gases in multimolecular layers. Journal of the American Chemical Society 60(2) (1938): 309-319.

[109] Rouquerol, J., et al. Recommendations for the characterization of porous solids. IUPAC Commission on colloid and surface chemistry. Pure and Applied Chemistry 66(8) (1994): 1739-1758.

[110] Yuh-Shan, H. Citation review of Lagergren kinetic rate equation on adsorption reactions. Scientometrics 59(1) (2004): 171-177.

[111] Agarwal, A.K., Kadu, M.S., Pandhurnekar, C.P., and Muthreja, I.L. Kinetics study on the adsorption of Ni^{2+} ions onto fly ash. Journal of Chemical Technology and Metallurgy 50(5) (2015): 601-605.

[112] Azizian, S. Kinetic models of sorption: a theoretical analysis. Journal of Colloid and Interface Science 276(1) (2004): 47-52.

[113] Ho, Y.S. and McKay, G. Pseudo-second order model for sorption processes. Process Biochemistry 34(5) (1999): 451-465.

[114] Afroze, S., Sen, T.K., Ang, M., and Nishioka, H. Adsorption of methylene blue dye from aqueous solution by novel biomass Eucalyptus sheathiana bark: equilibrium, kinetics, thermodynamics and mechanism. Desalination and Water Treatment 57(13) (2016): 5858-5878.

[115] Baskaralingam, P., Pulikesi, M., Elango, D., Ramamurthi, V., and Sivanesan, S. Adsorption of acid dye onto organobentonite. Journal of Hazardous Materials 128(2–3) (2006): 138-144.

[116] Malik, P.K. Dye removal from wastewater using activated carbon developed from sawdust: adsorption equilibrium and kinetics. Journal of Hazardous Materials 113(1–3) (2004): 81-88.

[117] Cirik, Y., Molu Bekci, Z., Buyukates, Y., Ak, İ., and Merdivan, M. Heavy metals uptake from aqueous solutions using marine algae (Colpomenia sinuosa): kinetics and isotherms. Chemistry and Ecology 28(5) (2012): 469-480.

[118] Sharma, A. and Bhattacharyya, K.G. Adsorption of chromium (VI) on Azadirachta Indica (Neem) leaf powder. Adsorption 10(4) (2005): 327-338.

[119] Demiral, H., Demiral, İ., Tümsek, F., and Karabacakoğlu, B. Adsorption of chromium(VI) from aqueous solution by activated carbon derived from olive bagasse and applicability of different adsorption models. Chemical Engineering Journal 144(2) (2008): 188-196.

[120] Bergaya, F. and Vayer, M. CEC of clays: measurement by adsorption of a copper ethylenediamine complex. Applied Clay Science 12(3) (1997): 275-280.

[121] Lee, J.-M. and Shackelford, C.D. Impact of bentonite quality on hydraulic conductivity of geosynthetic clay liners. Journal of Geotechnical and Geoenvironmental Engineering 131(1) (2005): 64-77.

[122] Hong, R.-Y., et al. Preparation and characterization of silica-coated Fe_3O_4 nanoparticles used as precursor of ferrofluids. Applied Surface Science 255(6) (2009): 3485-3492.

[123] Grover, K., Komarneni, S., and Katsuki, H. Synthetic hydrotalcite-type and hydrocalumite-type layered double hydroxides for arsenate uptake. Applied Clay Science 48(4) (2010): 631-637.

[124] Alabarse, F.G., Conceição, R.V., Balzaretti, N.M., Schenato, F., and Xavier, A.M. In-situ FTIR analyses of bentonite under high-pressure. Applied Clay Science 51(1–2) (2011): 202-208.

[125] Bishop, J.L. and Murad, E. Characterization of minerals and biogeochemical markers on Mars: a Raman and IR spectroscopic study of montmorillonite. Journal of Raman Spectroscopy 35(6) (2004): 480-486.

[126] Rivas, B.L., Canessa, G.S., and Martínez, E. Poly[3-(methacryloylamino)propyl]trimethylammonium chloride hydrogel. synthesis and water-absorption capacity. Boletín de la Sociedad Chilena de Química 45 (2000): 283-288.

[127] Sahiner, N., Demirci, S., Sahiner, M., Yilmaz, S., and Al-Lohedan, H. The use of superporous p(3-acrylamidopropyl)trimethyl ammonium chloride cryogels for removal of toxic arsenate anions. Journal of Environmental Management 152 (2015): 66-74.

[128] Celis, R., Trigo, C., Facenda, G., Hermosin Mdel, C., and Cornejo, J. Selective modification of clay minerals for the adsorption of herbicides widely used in olive groves. Journal of Agricultural and Food Chemistry 55(16) (2007): 6650-8.

[129] Xi, Y., Ding, Z., He, H., and Frost, R.L. Structure of organoclays—an X-ray diffraction and thermogravimetric analysis study. Journal of Colloid and Interface Science 277(1) (2004): 116-120.

[130] Souza, C.E.C. and Nascimento, R.S.V. Adsorption behavior of cationic polymers on bentonite. Journal of Thermal Analysis and Calorimetry 94(2) (2008): 579-583.

[131] Song, K. and Sandí, G. Characterization of montmorillonite surfaces after modification by organosilane. Clays and Clay Minerals 49(2) (2001): 119-125.

[132] Odian, G. Radical Chain Polymerization. in Principles of Polymerization, pp. 198-349: John Wiley & Sons, Inc., 2004.

[133] Sun, G., Zhang, M., He, J., and Ni, P. Synthesis of amphiphilic cationic copolymers poly[2-(methacryloyloxy)ethyl trimethylammonium chloride-co-stearyl methacrylate] and their self-assembly behavior in water and water-ethanol mixtures. Journal of Polymer Science Part A: Polymer Chemistry 47(18) (2009): 4670-4684.

[134] Supeno, Daik, R., and El-Sheikh, S.M. Cationic quaternization of cellulose with methacryloyloxy ethyl trimethyl ammonium chloride via ATRP method. AIP Conference Proceedings 1614(1) (2014): 178-185.

[135] Torres, C.C., Urbano, B.F., Campos, C.H., Rivas, B.L., and Reyes, P. Composite hydrogel based on surface modified mesoporous silica and poly[(2-acryloyloxy)ethyl trimethylammonium chloride]. Materials Chemistry and Physics 152 (2015): 69-76.

[136] Deng, H. and Yu, X. Adsorption of fluoride, arsenate and phosphate in aqueous solution by cerium impregnated fibrous protein. Chemical Engineering Journal 184 (2012): 205-212.

[137] Rivas, B.L., del Carmen Aguirre, M., and Pereira, E. Cationic water-soluble polymers with the ability to remove arsenate through an ultrafiltration technique. Journal of Applied Polymer Science 106(1) (2007): 89-94.

[138] Mohapatra, D., Mishra, D., Chaudhury, G.R., and Das, R.P. Arsenic(V) adsorption mechanism using kaolinite, montmorillonite and illite from aqueous medium. J Environ Sci Health A Tox Hazard Subst Environ Eng 42(4) (2007): 463-9.

[139] Baik, M.H. and Lee, S.Y. Colloidal stability of bentonite clay considering surface charge properties as a function of pH and ionic strength. Journal of Industrial and Engineering Chemistry 16(5) (2010): 837-841.

[140] Tombácz, E. and Szekeres, M. Colloidal behavior of aqueous montmorillonite suspensions: the specific role of pH in the presence of indifferent electrolytes. Applied Clay Science 27(1–2) (2004): 75-94.

[141] Thanhmingliana, Tiwari, D., and Lee, S.-M. Hybrid materials in the remediation of arsenic contaminated waters: a physico-chemical study. Desalination and Water Treatment 57(5) (2016): 1995-2005.

[142] Haraguchi, D., Tokoro, C., Oda, Y., and Owada, S. Sorption mechanisms of arsenate in aqueous solution during coprecipitation with aluminum hydroxide. Journal of Chemical Engineering of Japan 46(2) (2013): 173-180.

[143] Daneshvar, N., Salari, D., and Aber, S. Chromium adsorption and Cr(VI) reduction to trivalent chromium in aqueous solutions by soya cake. Journal of Hazardous Materials 94(1) (2002): 49-61.

[144] Wang, S.-L., Liu, C.H., Wang, M.K., Chuang, Y.H., and Chiang, P.N. Arsenate adsorption by Mg/Al–NO_3 layered double hydroxides with varying the Mg/Al ratio. Applied Clay Science 43(1) (2009): 79-85.

[145] Liu, H., Chen, W., Liu, C., Liu, Y., and Dong, C. Magnetic mesoporous clay adsorbent: Preparation, characterization and adsorption capacity for atrazine. Microporous and Mesoporous Materials 194 (2014): 72-78.

[146] Pan, J., et al. Magnetic molecularly imprinted polymers based on attapulgite/Fe_3O_4 particles for the selective recognition of 2,4-dichlorophenol. Chemical Engineering Journal 174(1) (2011): 68-75.

[147] Smedley, P.L. and Kinniburgh, D.G. A review of the source, behaviour and distribution of arsenic in natural waters. Applied Geochemistry 17(5) (2002): 517-568.

[148] Vaclavikova, M., Gallios, G., Hredzak, S., and Jakabsky, S. Removal of arsenic from water streams: an overview of available techniques. Clean Technologies and Environmental Policy 10(1) (2008): 89-95.

[149] Yang, L., Shahrivari, Z., Liu, P.K.T., Sahimi, M., and Tsotsis, T.T. Removal of trace levels of arsenic and selenium from aqueous solutions by calcined and uncalcined layered double hydroxides (LDH). Industrial & Engineering Chemistry Research 44(17) (2005): 6804-6815.

[150] You, Y.W., Zhao, H.T., and Vance, G.F. Removal of arsenite from aqueous solutions by anionic clays. Environmental Technology 22(12) (2001): 1447-57.

[151] Caporale, A.G., Pigna, M., Dynes, J.J., Cozzolino, V., Zhu, J., and Violante, A. Effect of inorganic and organic ligands on the sorption/desorption of arsenate on/from Al–Mg and Fe–Mg layered double hydroxides. Journal of Hazardous Materials 198 (2011): 291-298.

[152] Guo, Y., Zhu, Z., Qiu, Y., and Zhao, J. Adsorption of arsenate on Cu/Mg/Fe/La layered double hydroxide from aqueous solutions. Journal of Hazardous Materials 239–240 (2012): 279-288.

APPENDIX

VITA

Mister Soontorn Suvokhiaw was born on September 22, 1985 in Roi-Et, Thailand. He received Bachelor's Degree of Science in Chemistry from Khon Kaen University in 2008 and Master's Degree of Science in Chemistry from Chulalongkorn University in 2011. Since then he attended the Doctoral Degree Department of Chemistry at Faculty of Science, Chulalongkorn University.

His present address is 57 Naloeng, Selaphum, Roi-Et, 45120. Thailand. Tel 092-2729430, E-mail: s_suntornsc@hotmail.com.